FERMILAB-TM-2242

MARS Simulations of the NuMI Primary Beamline

Sergei Striganov

11 May 2004

Contents

1 Introduction **3**

2 MARS model setup **4**

3 Calculation Procedure **6**

4 Model Results **9**

4.1 Effects of Beam Phase Space 9
4.2 Beam Loss vs. Magnet Current Variations 14
4.3 Star Density vs. Beam Loss Models 18
4.4 Multi-wire Beam Loss 26
4.5 Beam Loss Correlations 34

A MARS Model Elements **37**

B Star Density Distributions **48**

C Star Density and Beam Loss Monitors **89**

Chapter 1

Introduction

MARS is a Monte Carlo code for simulation of three-dimensional hadronic and electromagnetic cascades, muon and low-energy neutron transport in shielding and in accelerator and detector components in the energy range from a fraction of an eV up to 100 TeV. This report uses MARS to both transport the 120 GeV primary proton beam from the NuMI extraction Lambertsons through the NuMI Pre-target Hall and calculate the radiological effect of beam losses at various locations and for a variety of conditions. These results are used to:

- anticipate where beam losses will be significant
- determine the level of activation of components
- calculate ground water activation and confirm adequacy of shielding

The results are presented in tables and figures along with drawings of the magnets as they were modeled in MARS. Details of the model elements are found in Appendix A. Further details of beam loss case studies are included in Appendix B.

Chapter 2

MARS model setup

The MARS NuMI beam line model includes the three NuMI Lambertson magnets, one MI lattice quadrupole, four 3Q60 and seventeen 3Q120 quadrupoles, one CMG-1 (”C”-magnet), six EPB, ten B2 bend magnets, two trim dipoles and ten horizontal and nine vertical correctors. A schematic of the major NuMI beamline elements is shown in Figure 2.1. Transverse and longitudinal cross sections of magnets are shown in Appendix A.

Longitudinal cross sections of NuMI tunnel are shown in the Appendix A. Note that the tunnel shape changes many times. Transverse cross sections of tunnel at different places are also presented in Appendix A.

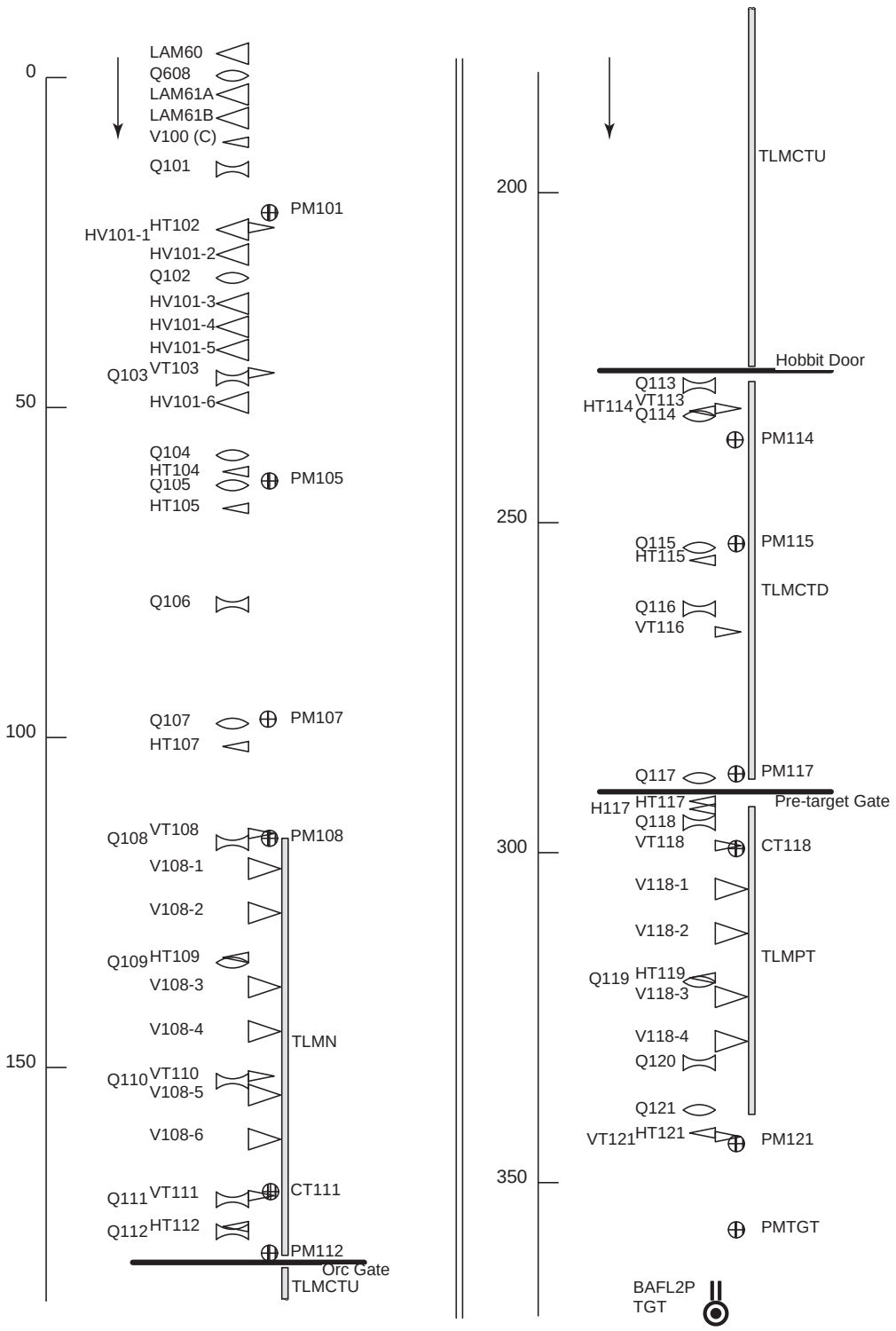

Figure 2.1: Beamline elements in NuMI. The scale is meters. The components designations are: Q=quadrupole (convex¿horiz focus, concave¿vert focus), V=vert. dipole, H=horiz. dipole, HV=rotated dipole, VT=vert. trim dipole, HT=horiz. trim dipole, LAM=labertson extraction magnet, PM=position monitor(wire scanner), CT=calibration target, TLM=loss monitor. Not shown: 45 sealed loss monitors on each magnet.

Chapter 3

Calculation Procedure

The MARS model of NuMI beamline was used to calculate

1. beam loss, star density
2. energy deposition in beam loss monitors
3. residual activity in beamline components

These calculations were performed for an appropriate set of variations in magnet current and the presence of wire scanners in the beam pipe.

First beam loss was simulated and the distribution of points where beam protons escaped the channel aperture was accumulated. If a beam proton exited the aperture it was stopped without production of secondary particles and was considered "lost". For all scenarios the number of "lost protons" was found for all the magnets and drift spaces. As a check for systematic errors, the simulation of beam loss distributions was performed by using two programs: MARS and STRUCT. Results of the two sets of calculations agree rather well (for example see figure 4.3), but STRUCT executes much faster. Hence, most results on beam loss were obtained using the STRUCT code. However, STRUCT does not provide the option to simulate cascades outside beam pipe. Therefore, star densities, energy deposition and residual activity were calculated using the MARS14 code.

A "star" is simply defined as an hadronic interaction vertex with at least one secondary particle which has a kinetic energy greater than 50 MeV. Average star densities were calculated for 7 regions around the NuMI tunnel as shown in figure 3.1. In most cases regions were defined for each section of the tunnel with constant cross section. For each region and any scenario, the maximum of star density distribution in the

rock near the tunnel (1 cm wide bins were used) are defined. Then the 99.9% volume boundary was determined by finding the transverse distance where the star density falls to 0.1% of maximum. For this volume the average star density, average radius and maximum radius are calculated.

In the simulation runs for residual activity a 20 MeV global threshold was used.

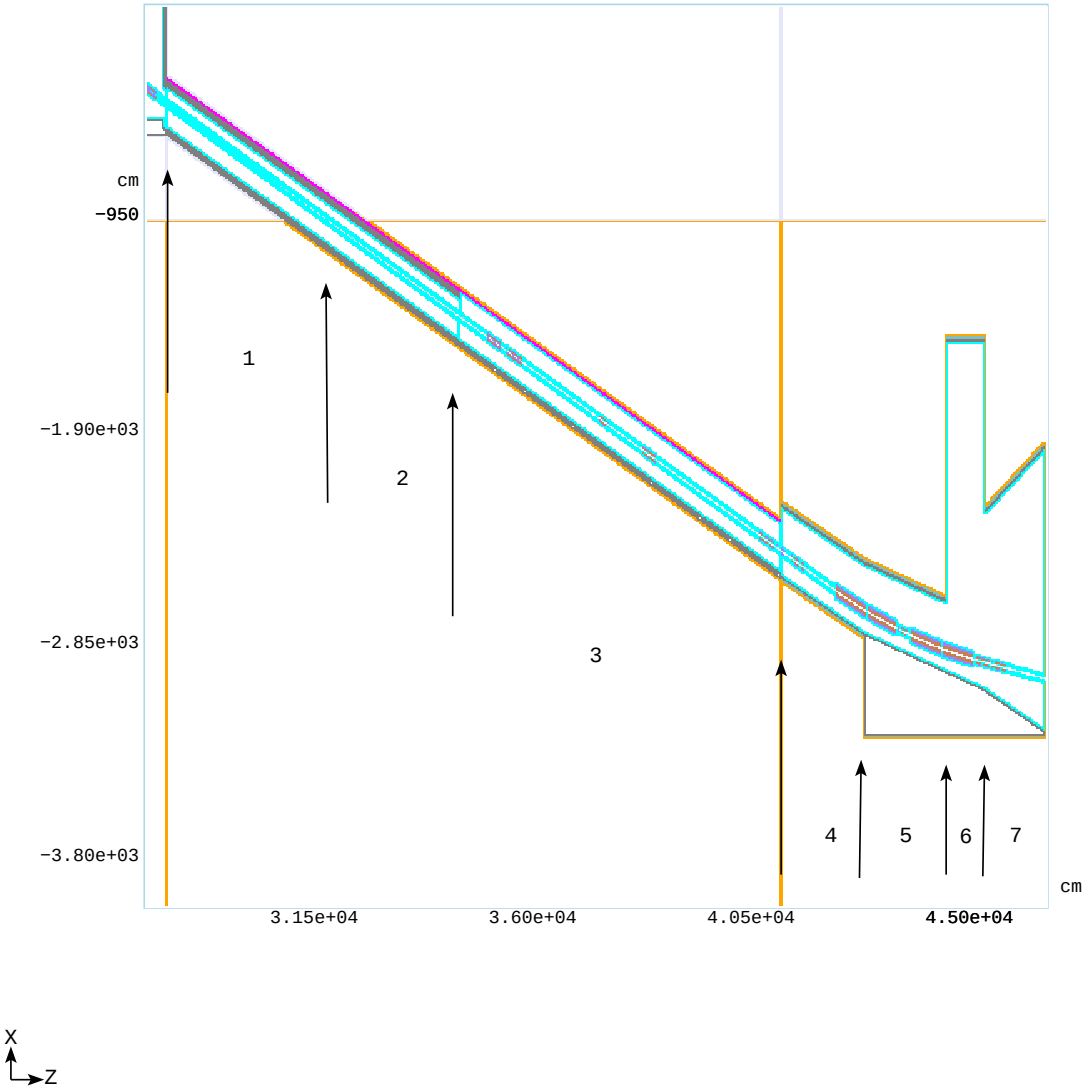

Figure 3.1: Regions for scoring star density distribution.

Chapter 4

Model Results

4.1 Effects of Beam Phase Space

The nominal phase space considered is 25π mm mrad 95% emittance with a 500π cut on beam tails. Momentum spread is $\delta p/p = 4 \times 10^{-4}$ at 95% with tails extending to 3×10^{-3}. Phase space distribution at the entrance to the first NuMI extraction Lambertson is shown in figure 4.1. These parameters are based on the measured performance of the Main Injector.

Beam size for 500π cut in comparison with beam-line apertures is presented in figure 4.2. It is clearly seen that beam losses for the normal tune are certainly less than 10^{-6} per proton (the last column in Table 4.1).

Beam profiles calculated using STRUCT and MARS at the end of NuMI channel are compared in figure 4.3. There is small shift of beam center (about 0.1 mm) in MARS calculations.

Beam of different emittances, from 25π to 60π, was transported through NuMI primary magnet system using old (prior to 2001) and current design. Resulting beam loss are presented in table 4.1. It is seen that the beam loss level is much lower for the present design. Beam losses only occur on the baffles, which are within the Target Hall shield pile, and are designed to withstand the mis-steering of the beam.

In addition, a worst case condition was simulated in STRUCT using an emittance of 40π mm mrad (95%) with a cut-off at 500π and momentum spread $\delta p/p$ of 4×10^{-4} with a cut-off at 3×10^{-3}. The losses at the end of the channel in front of the target (BAFL2P) with these conditions was found to be only 1.3×10^{-6} per proton.

Table.4.1 : Beam loss for normal tune (per primary proton). BAFFLE1 was only a part of the old beamline design)

95% emittance, $mm \cdot mrad$	60π	40π	60π	40π	25π
cuts, $mm \cdot mrad$	no	no	no	no	500π
$\delta p/p$	4×10^{-4}	2×10^{-4}	4×10^{-4}	2×10^{-4}	4×10^{-4}
design	old	old	new	new	new
HT107	2.0×10^{-3}	6.0×10^{-5}	0.	0.	0.
V110-1	8.7×10^{-4}	0.	0.	0.	0.
HT108	1.7×10^{-3}	2.0×10^{-3}	0.	0.	0.
BAFFLE1	4.0×10^{-3}	1.8×10^{-3}	NA	NA	NA
BAFL2P	3.4×10^{-3}	5.2×10^{-4}	$1. \times 10^{-4}$	$9. \times 10^{-7}$	0.
total	1.2×10^{-2}	4.4×10^{-3}	$1. \times 10^{-4}$	$9. \times 10^{-7}$	0.

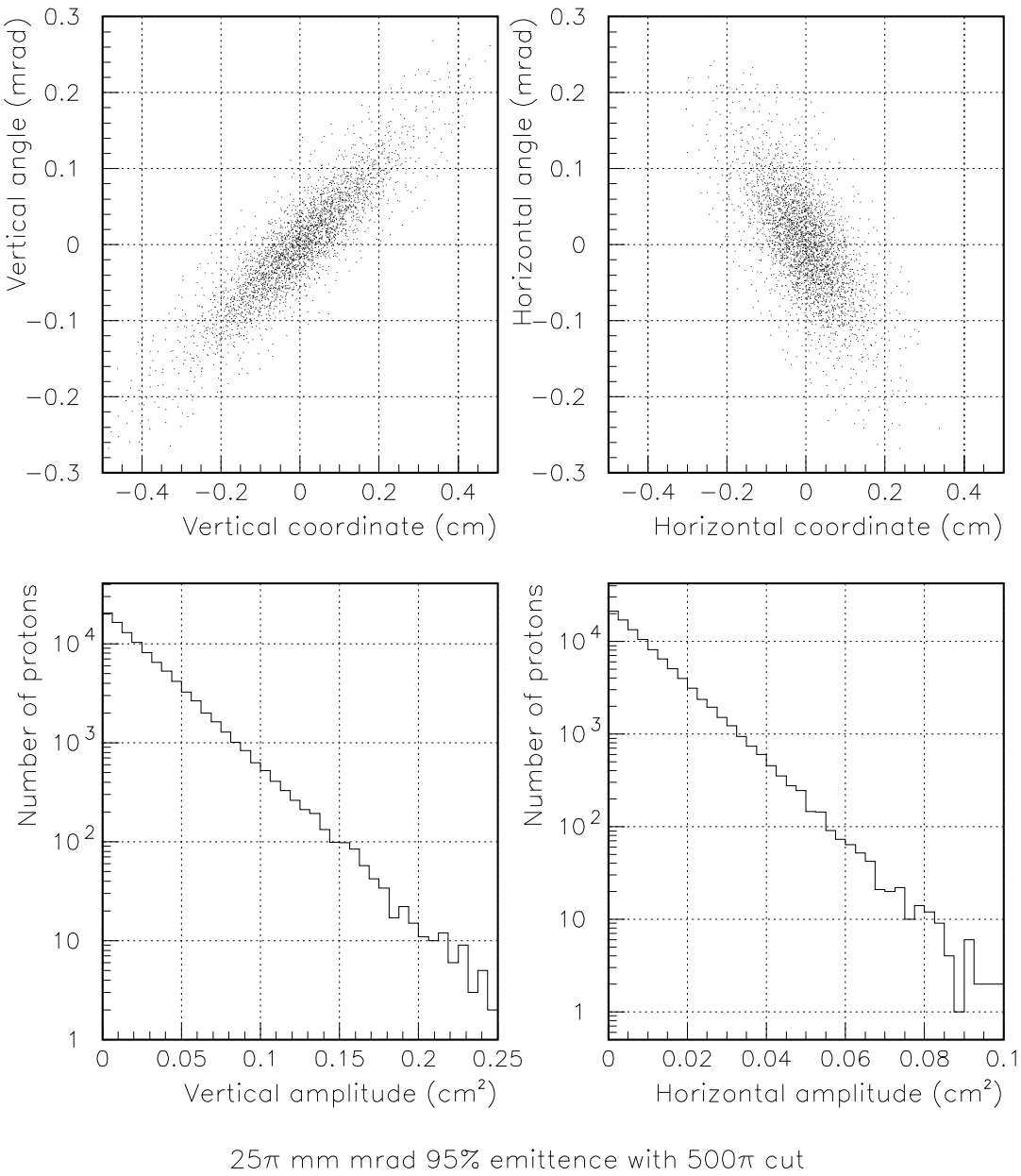

Figure 4.1: Beam distribution at first Lambertson.

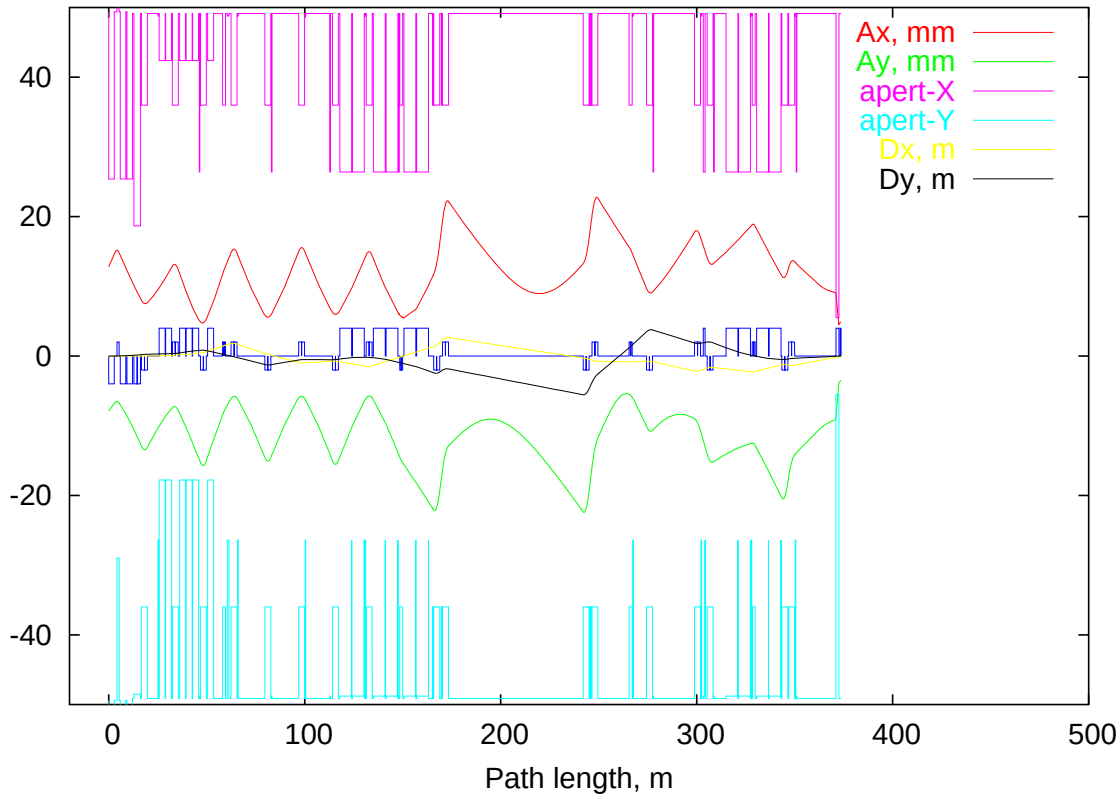

Figure 4.2: Beam size along NuMI beam-line. Maximum amplitude is 500 π mm mrad.

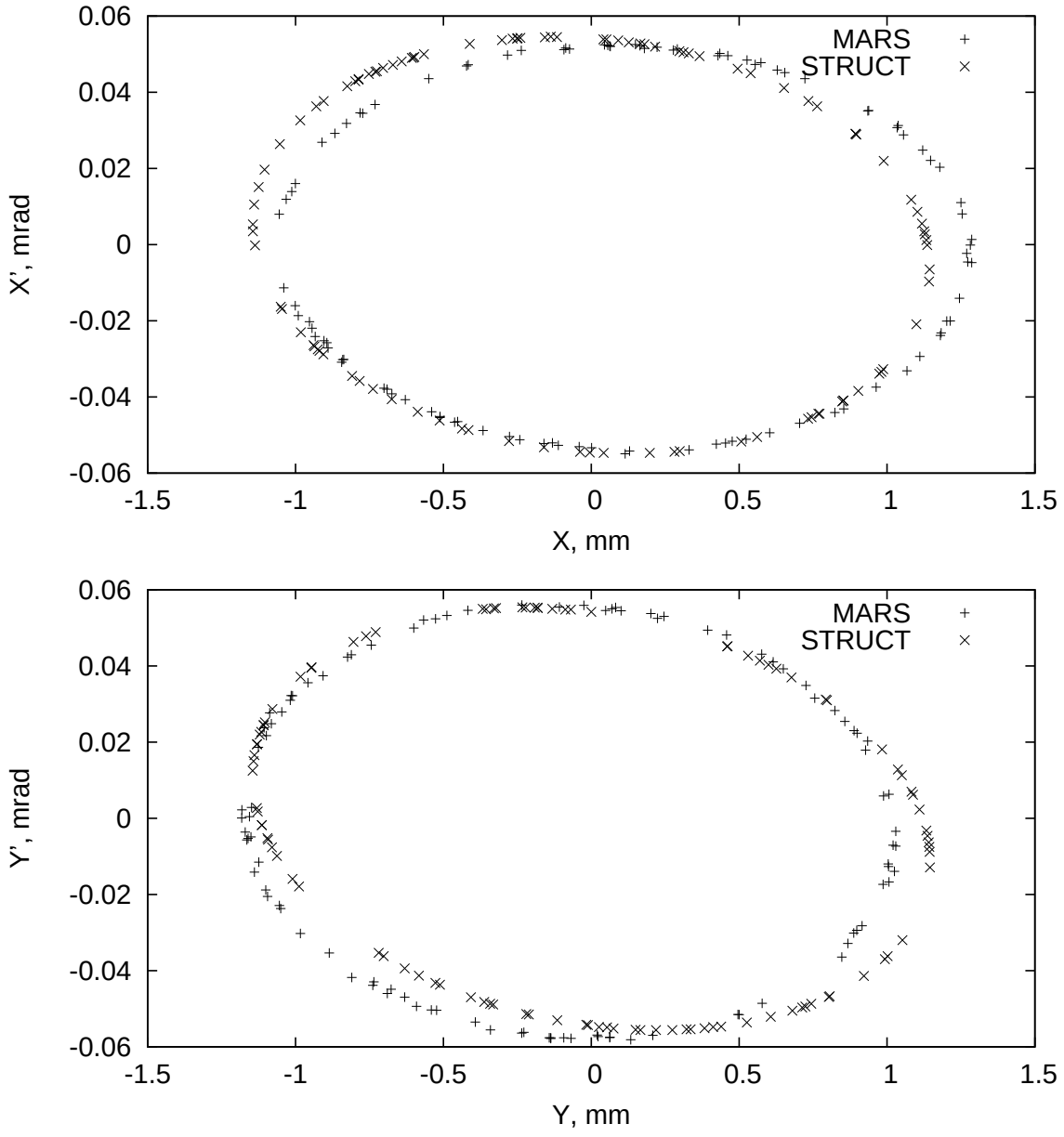

Figure 4.3: Beam distribution at BAFL2P.

4.2 Beam Loss vs. Magnet Current Variations

An important consideration in the operational control of beam loss is the stability of beam positions due to NuMI power supply current variations. The power supply current regulation limits achievable for NuMI are shown in Table 4.2.

Beam losses due to current variations for individual NuMI magnets are presented in figures 4.4-6. It is seen that significant beam losses are only possible for power supply current regulation much poorer than the limits of Table 4.2. But the combined effect, when some or all magnets have deviations from nominal field, could be much larger. There are 64 possible combinations of positive-negative deviations for six magnet power supplies. For each scenario, the shift in the beam position at the end of channel (at the BAFL2P) was calculated. Maximum displacement was obtained when LAM60A, LAM61AB, V100, V118 had negative and HV101, V108 positive deviations from nominal currents. Note that if all magnets have positive (or negative) deviations the beam shift is lower by a factor of ten. These results can be simply explained - the first four magnets move the beam up, the second two move it down. So, positive deflections in first magnets are compensated by positive deviations, or worsened by negative deflection in second pair. The dipole magnets deflect the beam horizontally only.

The kicker is not a part of the model. Using STRUCT the following relations were found between current variation (δ in %) in the kicker and the shift of horizontal coordinate (δh in cm) and angle ($\delta h^{'}$ in mrad)

$$\Delta h = 3.786 \times 10^{-2} \delta$$

and

$$\Delta h^{'} = 1.94 \times 10^{-2} \delta.$$

In most cases, the accidental beam loss due to power supply regulation problems will occur in the baffle (BAFL2P), as intended. There are a few conditions, with very large deviations from normal in V108 and HV101, which can cause losses on other elements. The values for $\Delta B/B$ causing loss points other than in BAFL2P can be extracted from Fig. 4.4 and 4.5. For field variations in V108 exceeding 0.6% the beam begins to be intercepted upstream of the baffle at HT111, HQ111 and HQ113 at levels exceeding 10^{-4}. For variations in the field of HV101 greater than 0.9%, 10^{-4} of the beam is lost on V118-2. As deviations continue to increase in HV101, the beam is lost further upstream: successively in HQ112, HT112 and finally in HQ111 (at $\Delta B/B >$ 1.5%). These are very large deviations: 200 times the nominal allowed.

The beam loss due to current variations from 3× limits to 10× normal limits (in Table 4.2) for all magnets simultaneously was simulated using MARS and STRUCT.

The resulting beam losses are shown in figure 4.6. It is seen that horizontal shift in both positive and negative directions due to current variation in kicker power supply gives the same beam loss.

Table.4.2 : Power supply current regulations.

Lam60A	Lam61AB	V100	HV101	V108	V118	kicker
$300ppm$	$150ppm$	$150ppm$	$50ppm$	$50ppm$	$50ppm$	0.5%

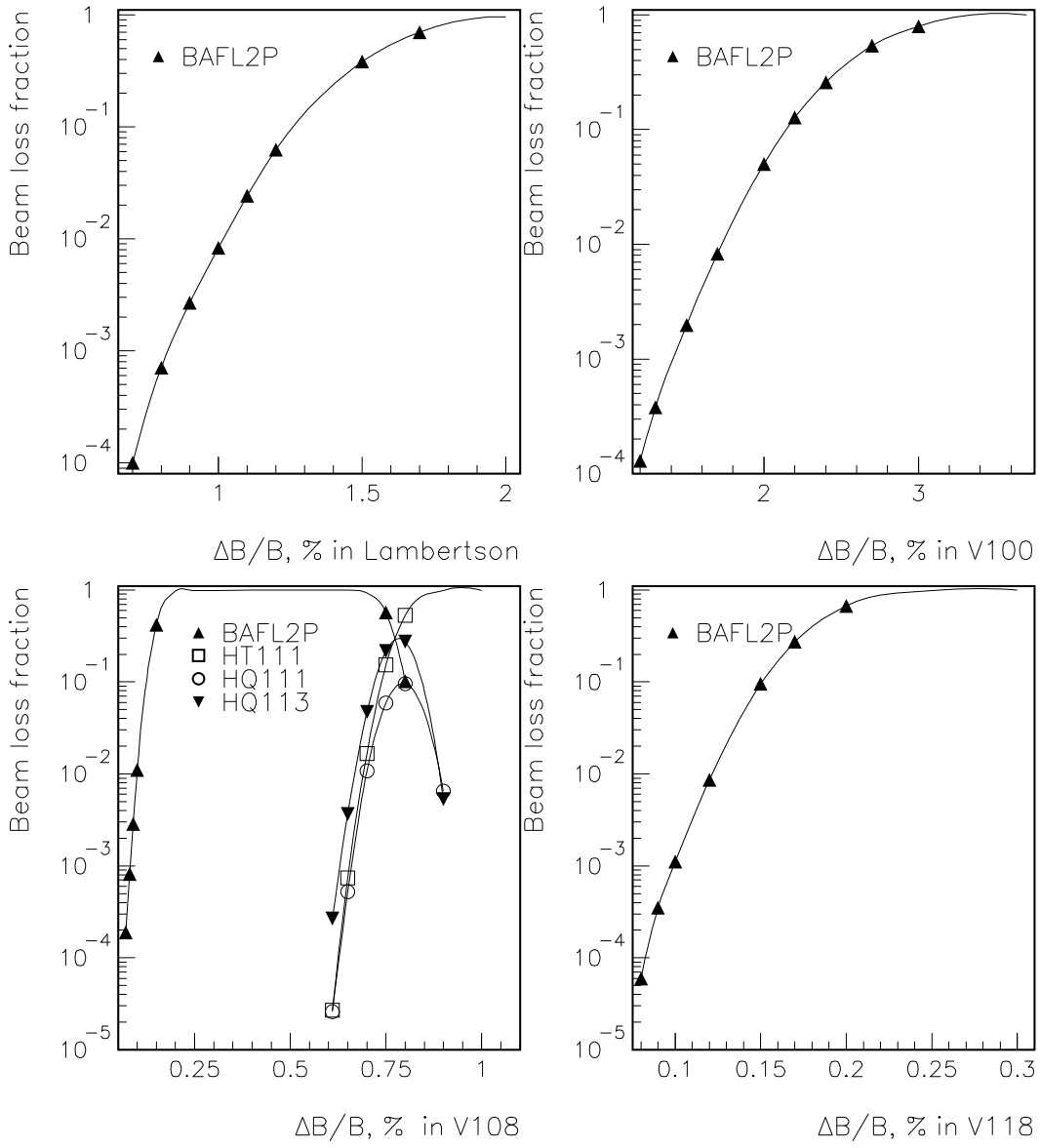

Figure 4.4: Beam loss vs. magnetic field variations.

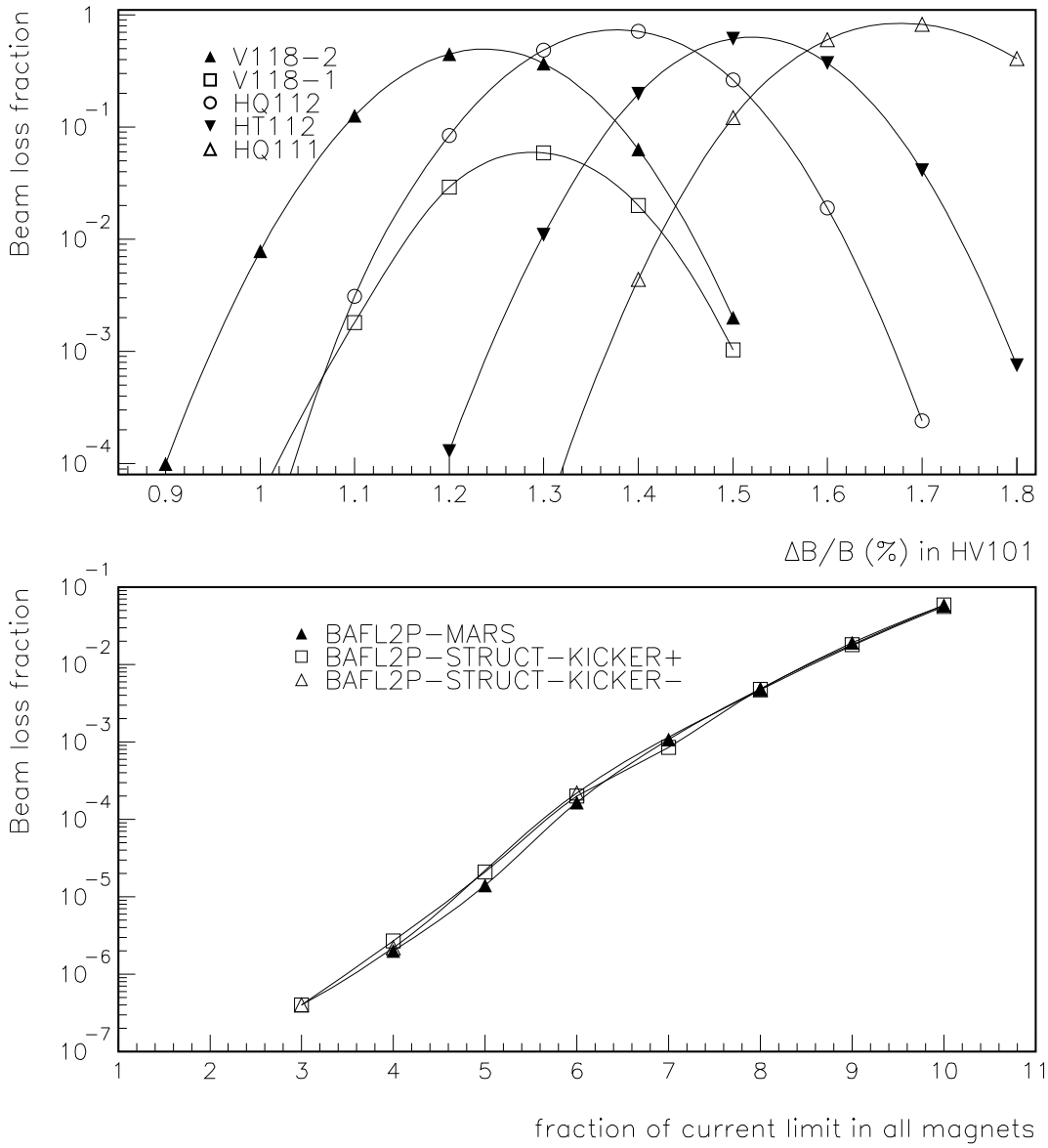

Figure 4.5: Beam loss vs. magnetic field deviation. The bottom plot represents the losses in BAFL2P as a function of the fractional deviation from the limits in Table 4.2. The loss is less than 10^{-6} when all magnets exceed three times their normal operating limits. The three curves show the insensitivity of the losses to the sign of the kicker magnet.

4.3 Star Density vs. Beam Loss Models

Star density distributions resulting from 11 scenarios of beam loss due to magnet current variations were considered. Using results from the previous section one can find a scenario with most of the beam loss in one region. This case gives the maximum of star density for this region. A summary of beam losses for all cases are presented in table 4.3. Note that in Tables 4-3, 4-4 and 4-5 the results listed in the row labeled "wire" are inclusive: all wire scanners were IN.

Typical star density distributions for the first one centimeter of depth as a function of distance along the tunnel are shown in figures 4.6-7. Typical spatial distributions of star density are presented on figures 4.8-9. A complete set of figures for star density for all scenarios are contained in Appendix B. The maximum and average star densities in the 99.9% volume for the 7 regions and the 12 beam loss scenarios are presented in tables 4.4-5. The mean and maximal radial extent of the 99.9% volume are shown in tables 4.6-7.

Accident-condition star density limits are compared with the simulations in table 4.8. It is seen that for the worst case, the acceptable level is about 20 times greater than the star density due to the total beam loss on one magnet. The star density and losses due to beam interaction with the wire scanners will be discussed in the next section. It is important to note that star densities per lost proton are practically the same for 100% and 0.01% beam loss.

Table.4.3 : Worst case beam loss (particle/proton) for the regions. Note that the largest potential losses are from directly hitting HQ111 and HQ112

source/region	HQ111	HQ112	3	4	5	6	7
HV101 1.20%	-	0.1505	-	0.3929	0.2265	-	-
HV101 1.25%	-	0.3552	-	0.4100	0.1401	-	-
HV101 1.40%	0.005	0.944	-	0.045	0.004	-	-
HV101 1.50%	0.1141	0.7635	-	0.002	-	-	-
V108 0.75%	0.2678	-	0.0775	-	-	0.03	0.6032
V108 0.78%	0.5144	-	0.1262	-		0.0542	0.3040
V108 0.85%	0.9442	-	0.0485	-		0.038	0.0029
V108 0.90%	0.9921	-	0.035	-		0.001	-
comb1	-	0.902	0.0015	0.0908	0.0038	-	-
comb2	0.0087	-	0.9912	-	-	-	0.0001
comb3	0.0474	-	0.0116	-	-	0.941	-
wire	8.3×10^{-5}	7.2×10^{-6}	2.2×10^{-5}	8.3×10^{-5}	-	-	7.2×10^{-6}

comb1 - HV101 1.4% @ V108 0.1%
comb2 - HV101 0.5% @ V108 0.8%
comb3 - V118 1.0% @ V108 0.7%
wire - all wire scanners IN

Table.4.4 : Star density (star/cc/pot) for the worst-case beam loss.

source/region	1	2	3	4	5	6	7
HV101 1.20%	5.0×10^{-8}	1.3×10^{-8}	2.8×10^{-7}	6.5×10^{-7}	8.0×10^{-8}	7.9×10^{-9}	6.9×10^{-9}
HV101 1.25%	1.3×10^{-7}	2.8×10^{-8}	2.9×10^{-7}	9.5×10^{-7}	5.6×10^{-8}	1.1×10^{-8}	4.9×10^{-9}
HV101 1.40%	1.8×10^{-7}	3.7×10^{-8}	5.7×10^{-8}	1.2×10^{-7}	6.7×10^{-9}	3.6×10^{-9}	1.7×10^{-9}
HV101 1.50%	2.2×10^{-7}	4.6×10^{-8}	1.9×10^{-7}	6.5×10^{-8}	7.8×10^{-9}	2.3×10^{-9}	2.0×10^{-9}
V108 0.75%	3.8×10^{-8}	1.0×10^{-8}	2.0×10^{-7}	2.7×10^{-9}	3.2×10^{-9}	7.8×10^{-9}	1.4×10^{-7}
V108 0.78%	8.8×10^{-8}	1.0×10^{-8}	4.0×10^{-7}	4.4×10^{-9}	5.7×10^{-9}	8.9×10^{-9}	7.3×10^{-8}
V108 0.85%	2.5×10^{-7}	3.6×10^{-8}	2.7×10^{-7}	4.4×10^{-9}	3.0×10^{-9}	7.2×10^{-9}	2.7×10^{-9}
V108 0.90%	2.5×10^{-7}	5.7×10^{-8}	2.9×10^{-7}	9.8×10^{-9}	4.7×10^{-9}	1.9×10^{-8}	5.5×10^{-9}
comb 1	2.1×10^{-7}	5.2×10^{-8}	7.3×10^{-8}	1.8×10^{-8}	1.1×10^{-8}	2.8×10^{-9}	2.4×10^{-9}
comb 2	2.3×10^{-9}	1.1×10^{-9}	3.8×10^{-6}	3.6×10^{-8}	6.0×10^{-9}	4.5×10^{-9}	2.2×10^{-9}
comb 3	5.7×10^{-9}	1.9×10^{-9}	2.6×10^{-8}	5.9×10^{-10}	5.2×10^{-8}	2.5×10^{-7}	5.5×10^{-8}
wire	1.1×10^{-11}	3.2×10^{-12}	2.9×10^{-11}	1.4×10^{-10}	3.1×10^{-11}	7.2×10^{-12}	2.6×10^{-12}
limit	1×10^{-4}	1×10^{-6}	1×10^{-4}	1×10^{-4}	1×10^{-4}	1×10^{-4}	1×10^{-4}

Table.4.5 : Worst-case beam loss average star density (star/cc/pot) in 99.9% volume.

source/region	1	2	3	4	5	6	7
HV101 1.20%	3.4×10^{-9}	1.1×10^{-9}	3.9×10^{-9}	3.2×10^{-8}	6.0×10^{-9}	6.9×10^{-10}	3.4×10^{-10}
HV101 1.25%	7.4×10^{-9}	2.3×10^{-9}	5.9×10^{-9}	3.1×10^{-8}	3.9×10^{-9}	5.4×10^{-10}	2.8×10^{-10}
HV101 1.40%	1.3×10^{-8}	3.8×10^{-9}	6.7×10^{-9}	4.0×10^{-9}	4.8×10^{-10}	1.8×10^{-10}	9.1×10^{-11}
HV101 1.50%	1.3×10^{-8}	4.4×10^{-9}	1.3×10^{-8}	3.5×10^{-9}	5.3×10^{-10}	1.8×10^{-10}	8.2×10^{-11}
V108 0.75%	2.5×10^{-9}	5.2×10^{-10}	6.8×10^{-9}	8.8×10^{-11}	1.0×10^{-10}	7.0×10^{-10}	9.2×10^{-9}
V108 0.78%	5.2×10^{-9}	9.1×10^{-10}	1.3×10^{-8}	1.4×10^{-10}	1.3×10^{-10}	6.8×10^{-10}	5.0×10^{-9}
V108 0.85%	1.5×10^{-8}	3.4×10^{-9}	1.3×10^{-8}	2.5×10^{-10}	1.6×10^{-10}	6.2×10^{-10}	1.7×10^{-10}
V108 0.90%	1.7×10^{-8}	6.5×10^{-9}	1.9×10^{-8}	4.7×10^{-10}	2.7×10^{-9}	1.5×10^{-9}	3.0×10^{-10}
comb 1	1.4×10^{-8}	4.4×10^{-9}	7.1×10^{-9}	9.0×10^{-9}	6.8×10^{-10}	2.4×10^{-10}	1.2×10^{-10}
comb 2	1.0×10^{-10}	3.7×10^{-11}	1.3×10^{-7}	3.2×10^{-9}	3.5×10^{-10}	1.9×10^{-10}	1.3×10^{-10}
comb 3	3.7×10^{-10}	1.1×10^{-10}	9.2×10^{-10}	1.5×10^{-11}	2.3×10^{-9}	1.9×10^{-8}	2.6×10^{-9}
wire	1.7×10^{-12}	3.8×10^{-13}	3.3×10^{-12}	6.4×10^{-12}	1.2×10^{-12}	3.1×10^{-13}	1.6×10^{-13}

Table.4.6 : Star-density-weighted mean radial thickness (cm)

source/region	1	2	3	4	5	6	7
HV101 1.20%	56	55	50	28	31	30	31
HV101 1.25%	57	55	50	36	37	32	37
HV101 1.40%	60	55	50	36	36	31	40
HV101 1.50%	62	53	50	27	29	30	33
V108 0.75%	62	51	53	29	77	30	28
V108 0.78%	67	52	52	27	49	32	29
V108 0.85%	65	51	49	28	33	32	25
V108 0.90%	63	51	49	26	35	32	38
comb 1	59	55	49	28	29	29	31
comb 2	67	52	50	28	29	32	33
comb 3	63	52	51	71	63	35	51
wire	72	52	47	36	33	30	35

Table.4.7 : Radial thickness (cm) of the 99.9% volume.

source/region	1	2	3	4	5	6	7
HV101 1.20%	428	278	188	195	195	195	285
HV101 1.25%	428	293	203	165	225	165	285
HV101 1.40%	503	323	233	195	255	165	285
HV101 1.50%	488	378	233	195	165	195	285
V108 0.75%	518	248	248	195	285	195	195
V108 0.78%	503	293	248	195	285	225	165
V108 0.85%	488	263	233	195	285	195	285
V108 0.90%	488	233	233	195	285	195	285
comb 1	458	308	248	165	255	225	285
comb 2	458	248	333	195	255	195	285
comb 3	563	353	233	285	285	195	285
wire	503	383	248	195	195	135	285

Table.4.8 : Accidental beam loss.

region	star density limit star/cc/proton	maximum star/cc/lost proton	origin	wire scanners star/cc/lost proton
1	5.3×10^{3}	1.7×10^{-8}	99% loss on HT111	1.8×10^{-8}
2	2.8×10^{-6}	6.6×10^{-9}	99% loss on HT111	4.2×10^{-9}
3	2.7×10^{-6}	1.3×10^{-7}	99% loss on HQ113	1.5×10^{-7}
4	2.7×10^{-6}	8.2×10^{-8}	39% loss on HT117	7.7×10^{-8}
5	2.7×10^{-6}	2.6×10^{-8}	23% loss on V118-2	
6	2.7×10^{-6}	2.0×10^{-8}	94% loss on V118-4	
7	2.7×10^{-6}	1.5×10^{-8}	60% loss on HT121	2.2×10^{-8}

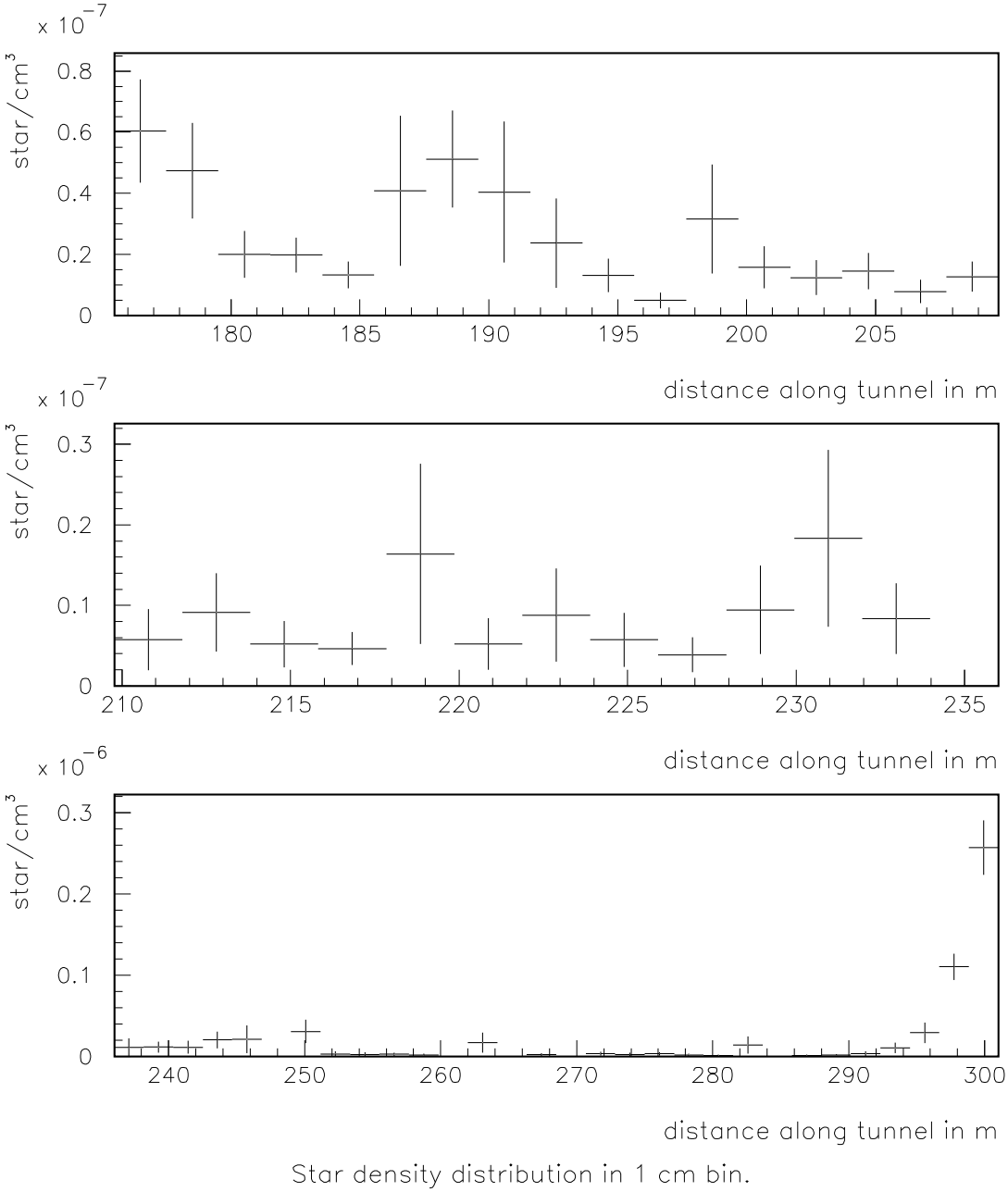

Figure 4.6: Star density distribution for first three regions. Magnet current variation on 1.2% in HV101. The top plot begins at the gate just downstream of Q112. The bottom plot ends at the Pre-target gate.

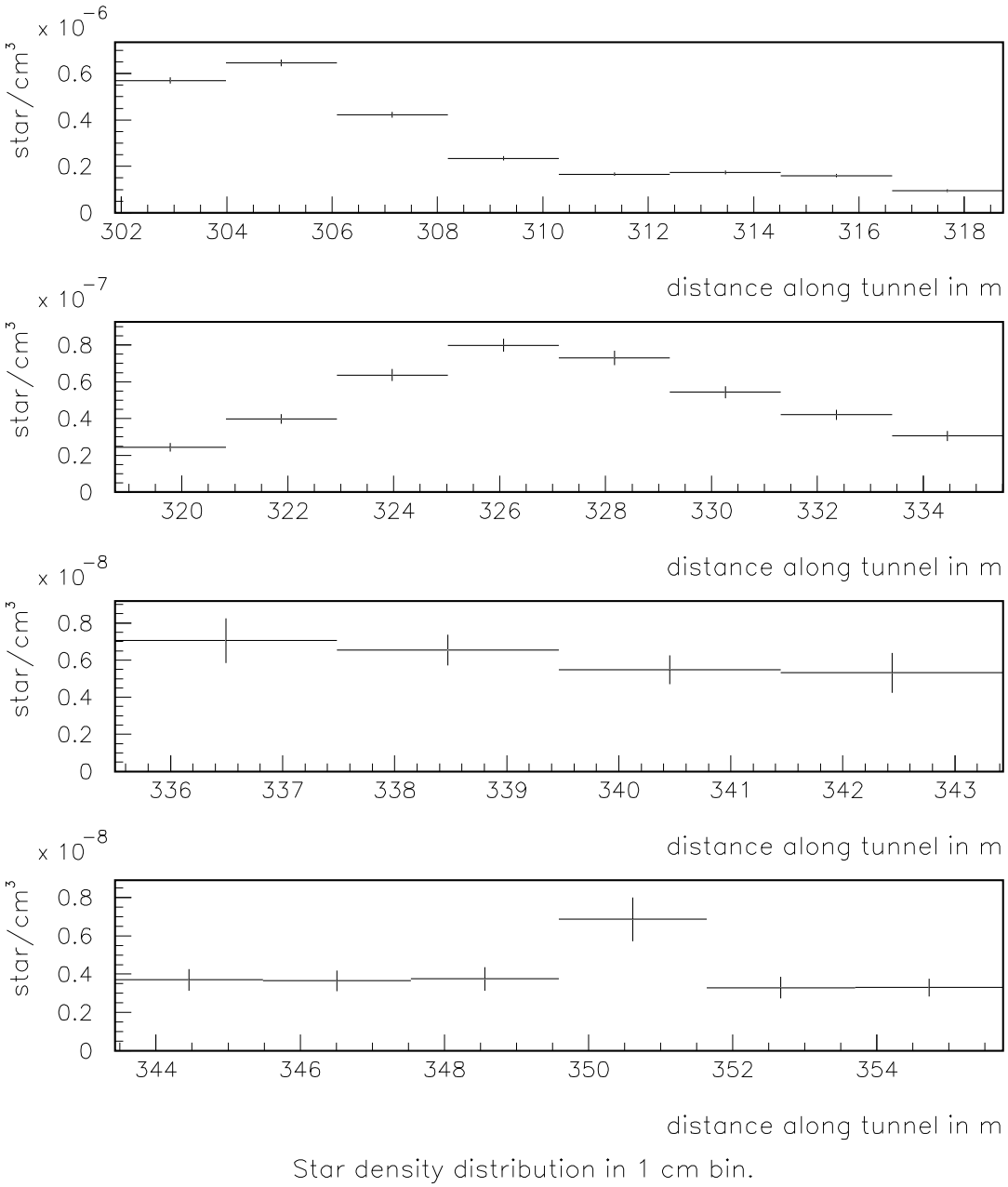

Figure 4.7: Star density distribution for last four regions. Magnet current variation on 1.2% in HV101. The top plot begins at the Pre-target gate.

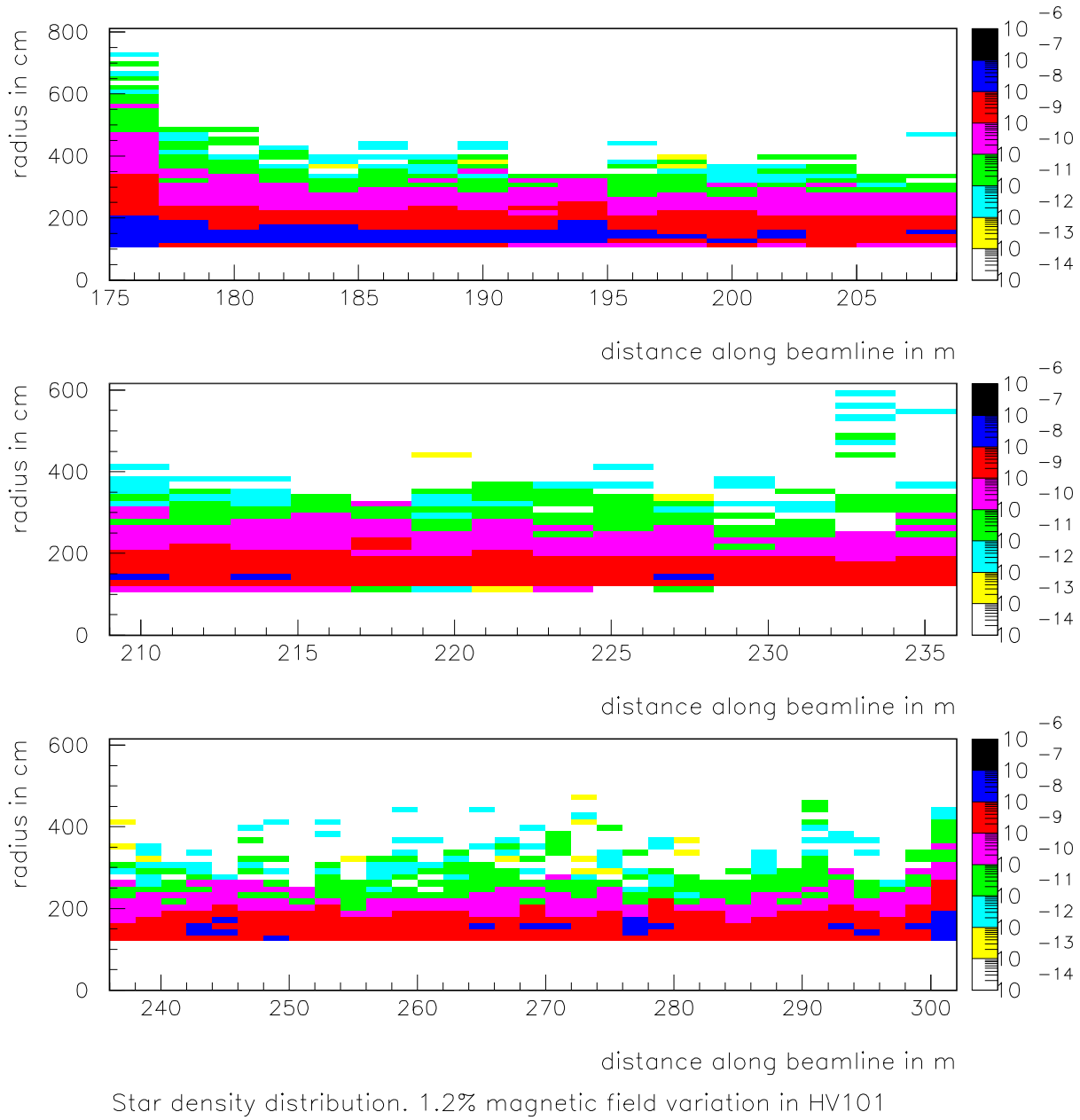

Figure 4.8: Star density distribution for first three regions. The top plot begins at the gate just downstream of Q112. The bottom plot ends at the Pre-target gate.

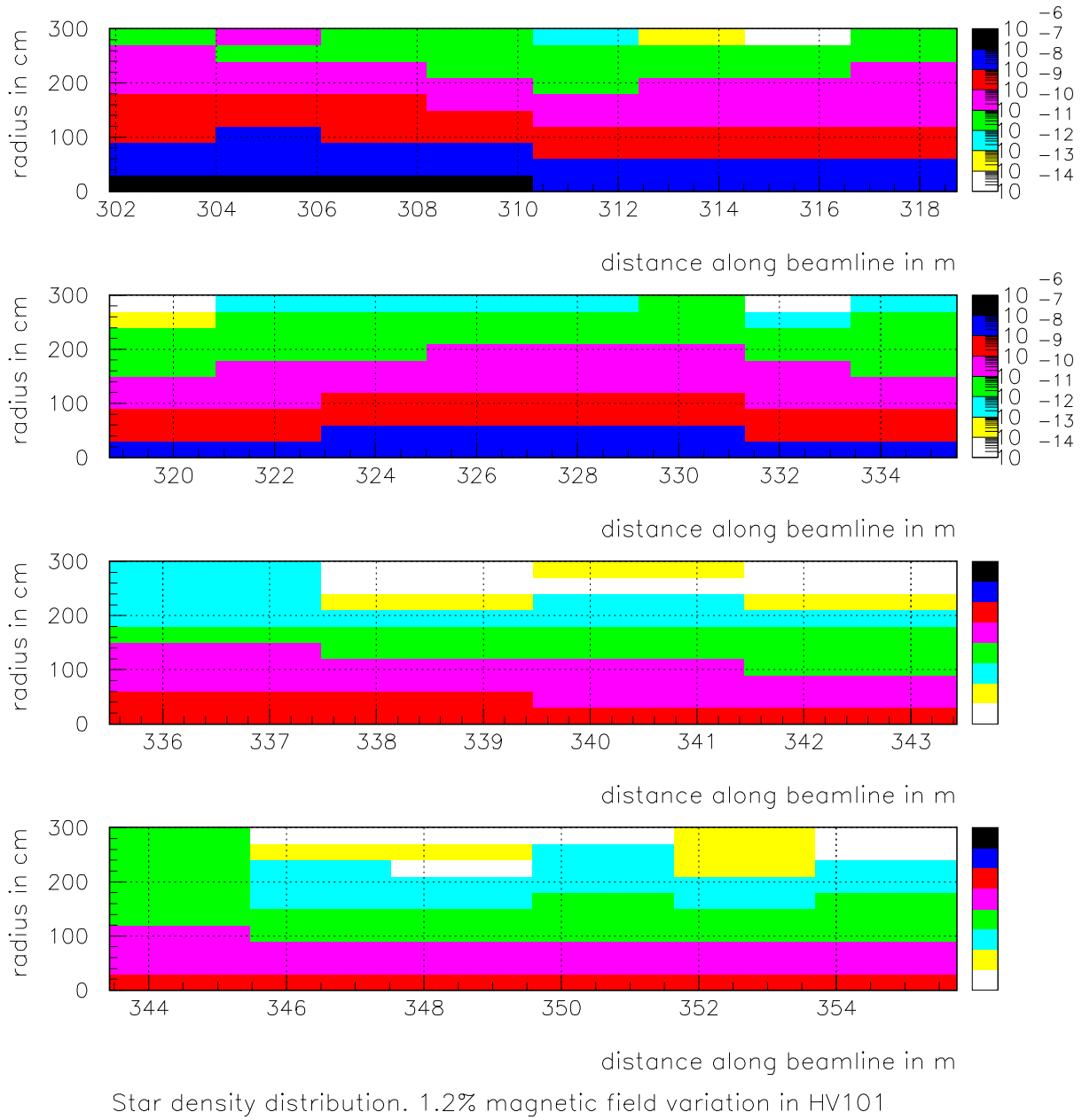

Figure 4.9: Star density distribution for last four regions. The top plot begins at the Pre-target gate.

4.4 Multi-wire Beam Loss

Two types of wire scanners are to be used in the NuMI channel. The first consists of two planes of tungsten wires, each wire 75 microns in diameter. The separation between wires is 1 mm. The probability of a primary proton interacting with this device is 8.3×10^{-5}. There are only two such scanners in the channel - PM111 and PM118.

All the other multi-wires are much thinner and use strips instead of wires. Each strip thickness is 5 microns of titanium, and the width is 0.25 mm. The strips are separated by 1 mm. Again each device has two planes of strips. The probability of interactions with this scanner is ten times smaller: 8.3×10^{-6}.

In the Tables and Figures that follow, the results are calculated with all wire scanners IN, simultaneously. Star densities due to beam interactions with wire scanners are shown in figures 4.10-4.13. A summary of beam losses is presented in Table 4.3. The average star density in the 99.9% volume, and the average and maximum radius of this volume are shown in Tables 4.4-4.7.

Star densities due to beam interaction with all wire scanners IN are compared with operational limits in Table 4.9. The effects of losses on the wire scanners is within the acceptable limits.

Residual activity due to interaction of beam protons with wire scanners is presented in figure 4.14. It is important to note that the data shown in fig. 4.14 represents the residual dose on contact for the various beamline elements assuming a continuous 30-day irradiation at full beam intensity with *all* wirescanner IN simultaneously. While this mode will not be part of NuMI running conditions, for the purposes of this study it represents a worst-case scenario. Even so, residual dose on contact is within accepted limits. The neutron flux and prompt dose, averaged over the surface of the magnet facing the wire scanners, is also given in tabular form in Table 4.10. Finally, the calculated losses for each wire chamber are given in Table 4.11.

Table.4.9 : Operational beam loss, star/cc/proton. All wire scanners are IN.

region	star density limit	star density - wire
1	6.4×10^{-4}	1.7×10^{-12}
2	2.1×10^{-12}	3.8×10^{-13}
3	5.7×10^{-10}	3.3×10^{-12}
4	4.8×10^{-10}	6.4×10^{-12}
5	6.4×10^{-10}	1.2×10^{-12}
6	6.4×10^{-10}	3.1×10^{-13}
7	6.4×10^{-10}	1.6×10^{-13}

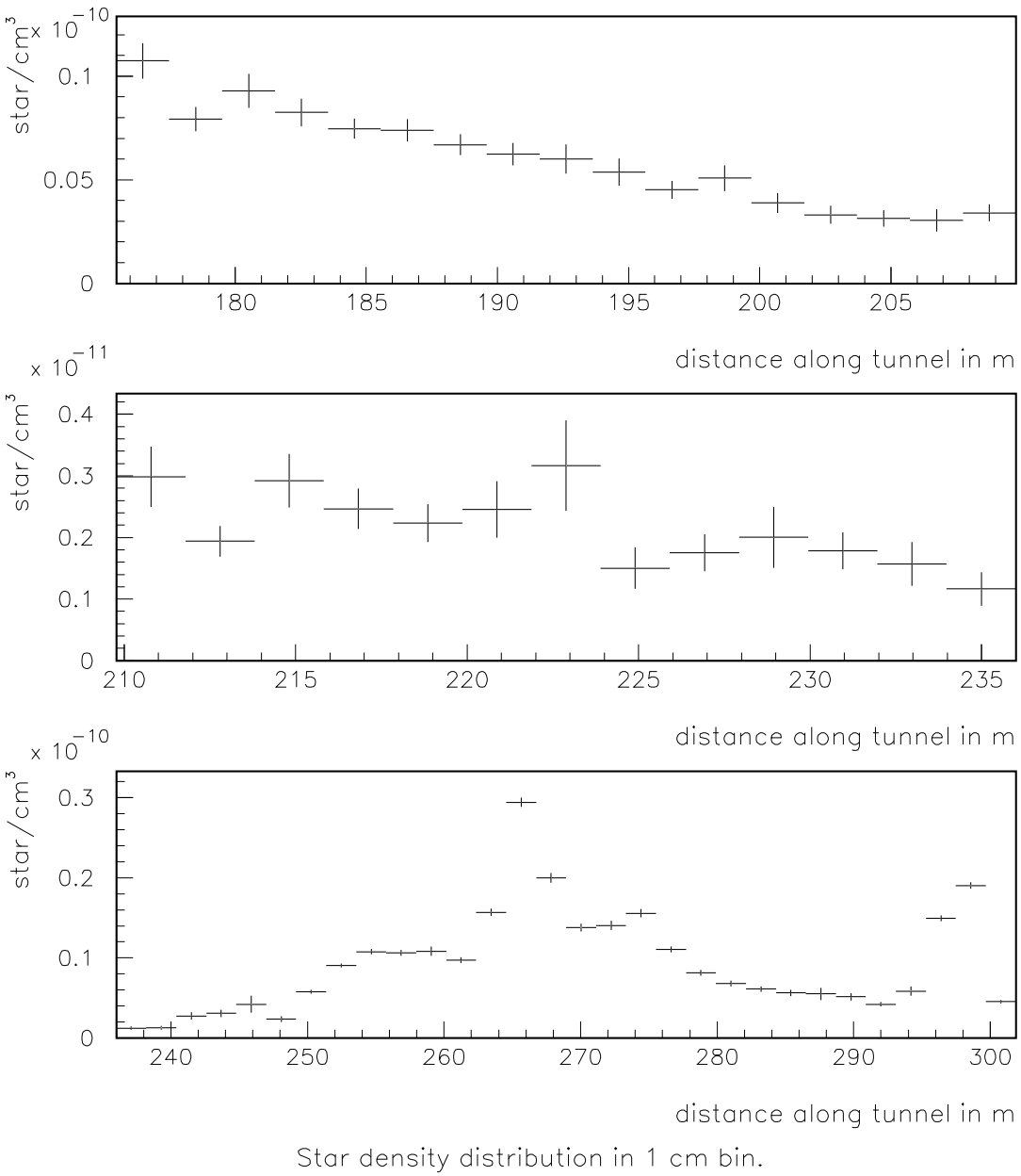

Figure 4.10: Star density distribution for first three regions. Wire scanners. The top plot begins at the gate just downstream of Q112. The bottom plot ends at the Pre-target gate.

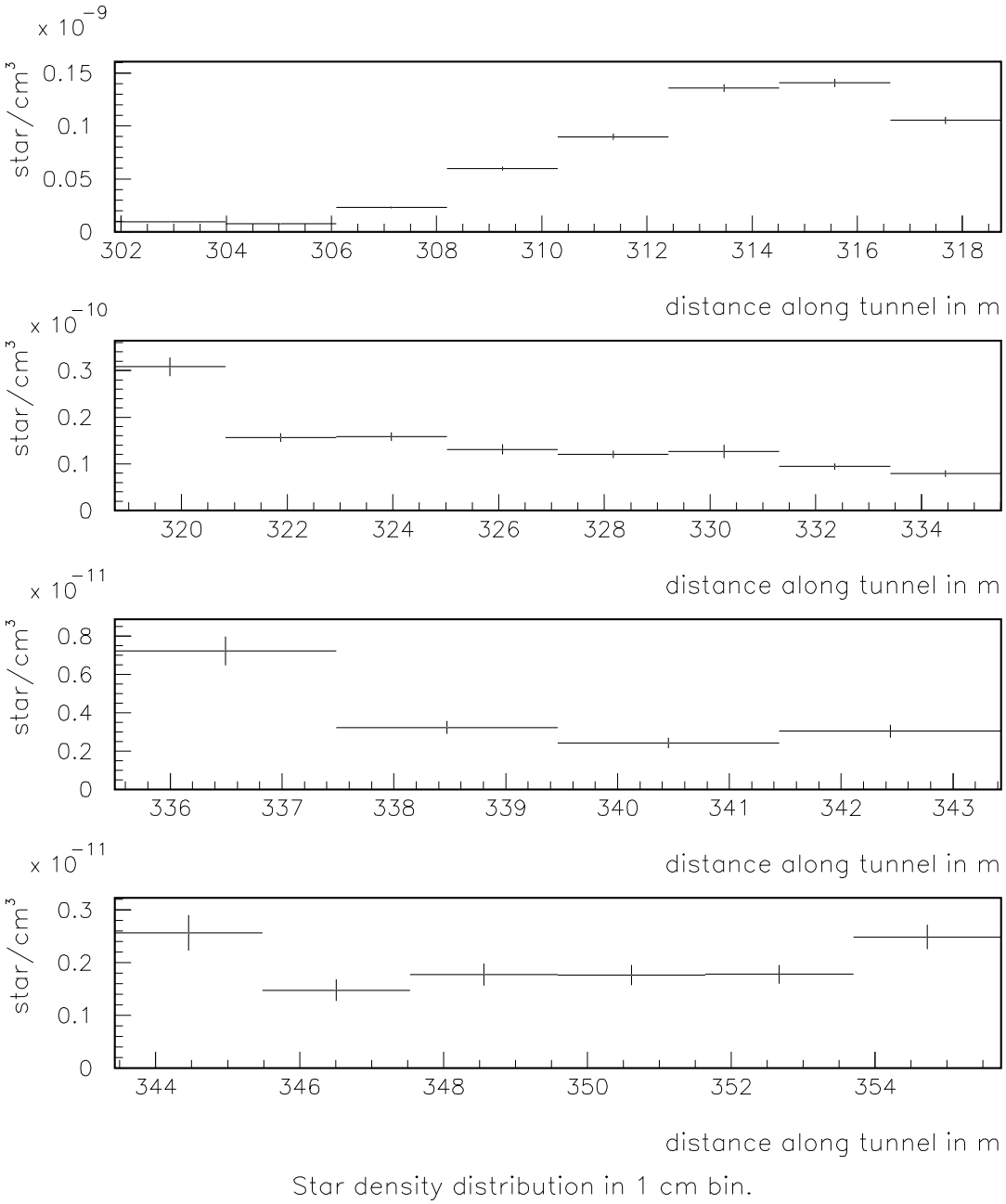

Figure 4.11: Star density distribution for last four regions. Wire scanners. The top plot begins at the Pre-target gate.

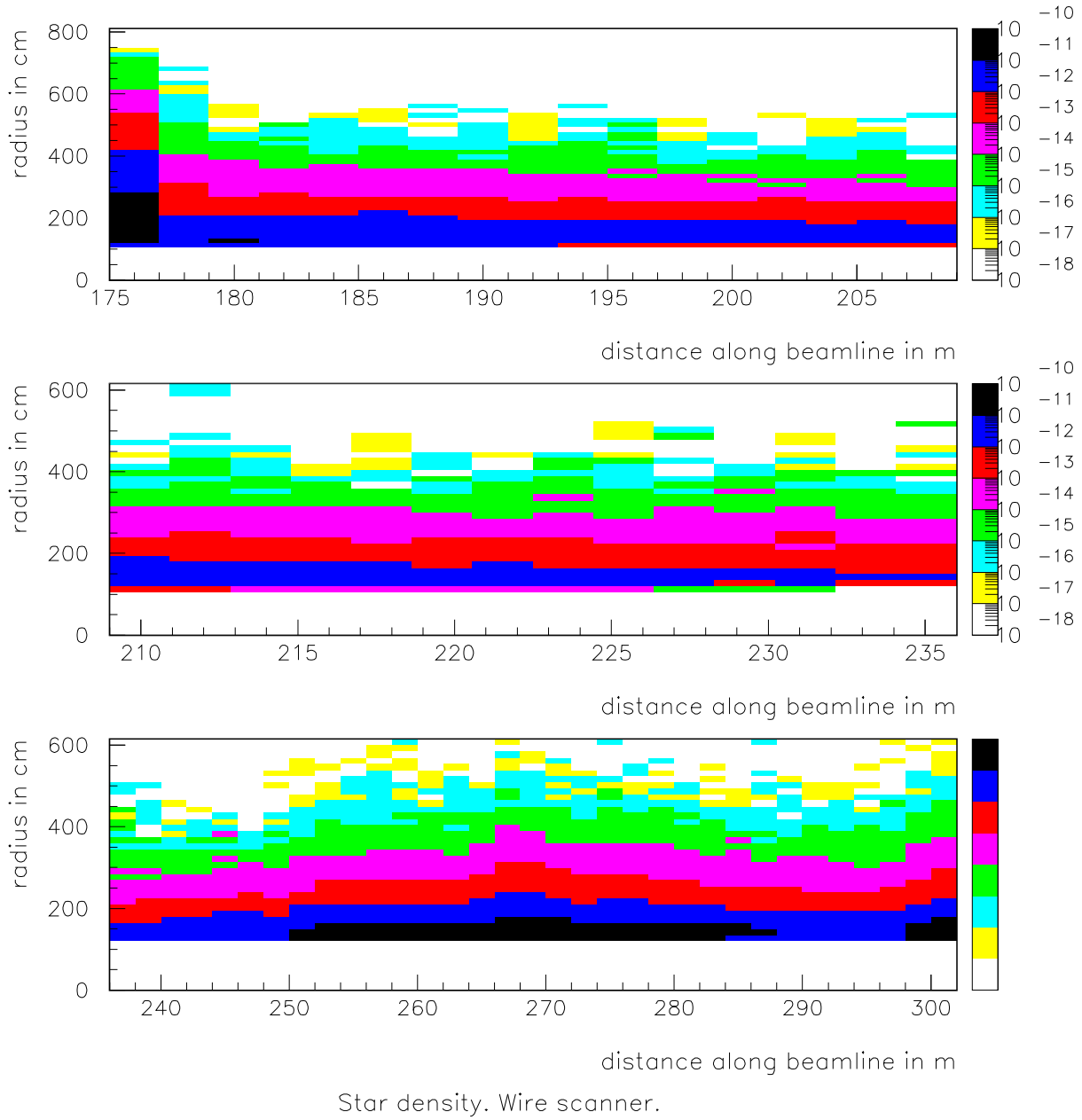

Figure 4.12: Star density distribution for first three regions. The top plot begins at the gate just downstream of Q112. The bottom plot ends at the Pre-target gate.

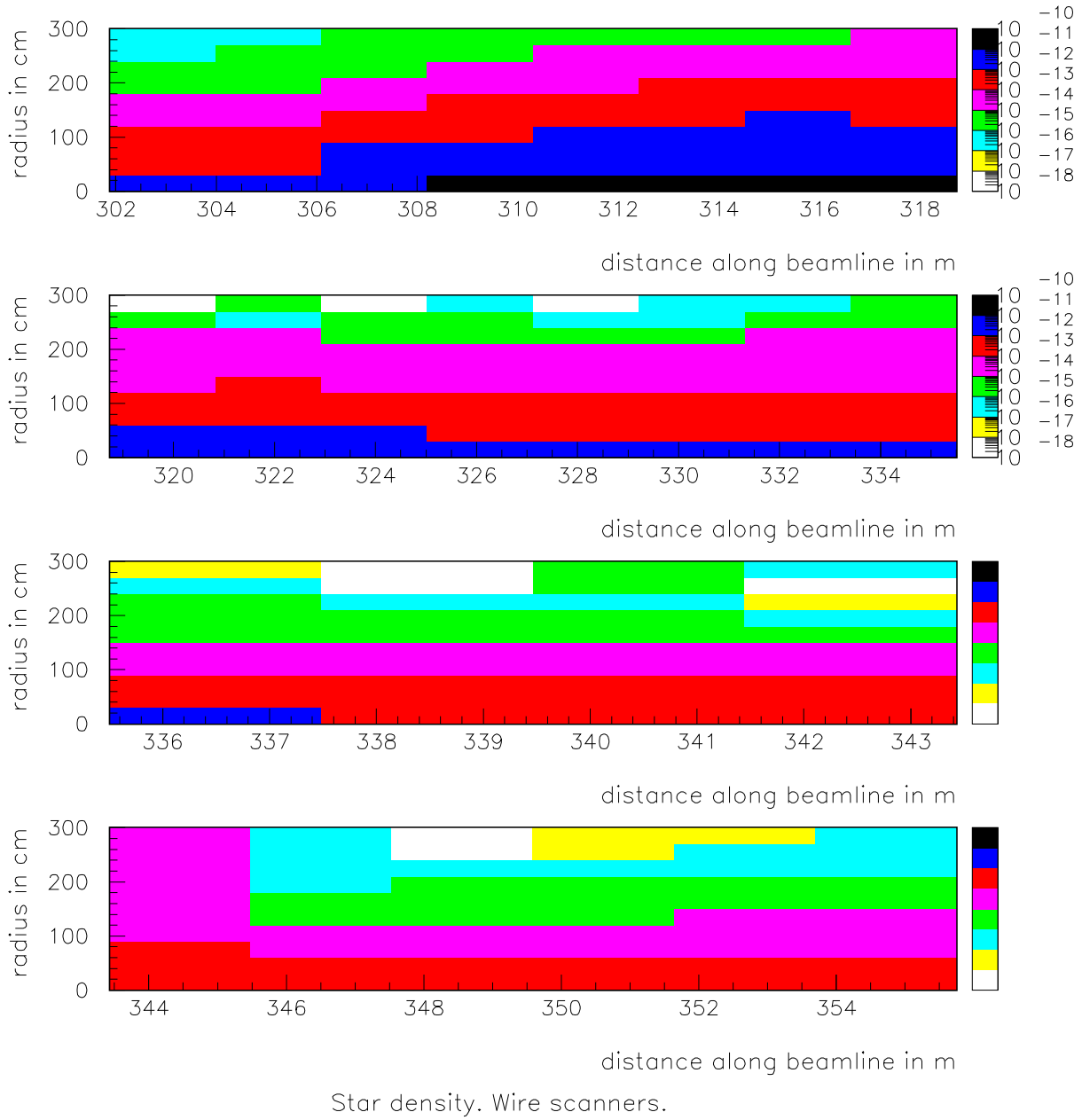

Figure 4.13: Star density distribution for last four regions. The top plot begins at the Pre-target gate.

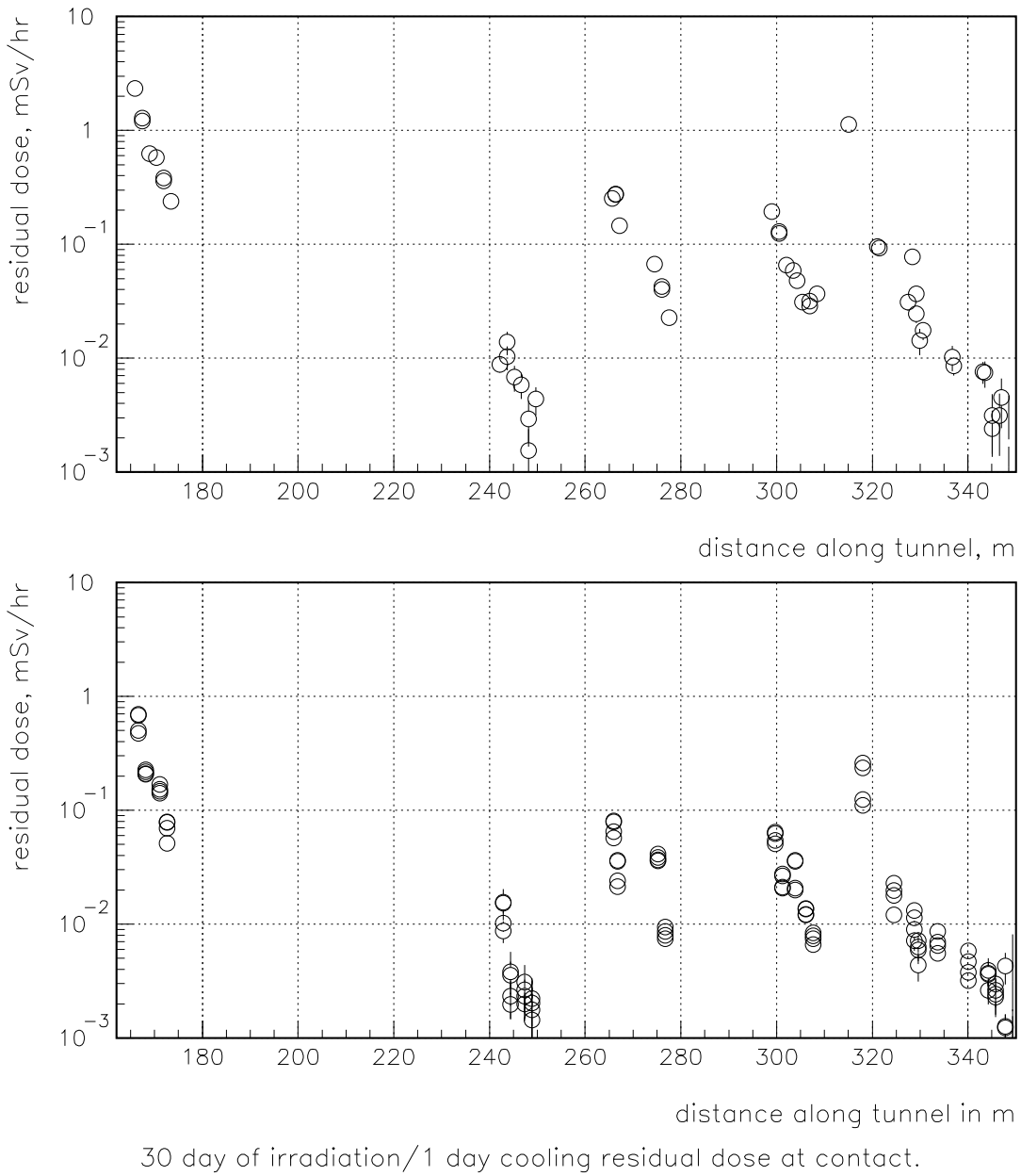

Figure 4.14: Residual dose from interaction of beam protons with all wire scanners IN (1 mSv/hr is equal to 100 mRem/hr). (*top*) dose averaged over the front face of each magnet and (*bottom*) dose averaged along the side of each magnet

Table.4.10 : Flux and prompt dose at the suface of magnets along the beamline from interactions with the wire scanners. The distance is measured from the upstream face of the first Lambertson magnet (see Fig. 2.1).

Z (m)	neutrons (cm^{-2} p^{-1})	charged hadrons (cm^{-2} p^{-1})	Dose (mSv p^{-1})	Dose Error (mSv p^{-1})
166.638	4.02220E-07	1.03390E-07	2.01025E-13	3.99820E-15
168.162	1.56740E-07	2.59310E-08	5.89600E-14	2.01873E-15
171.111	1.07030E-07	2.64700E-08	5.22475E-14	2.70801E-15
172.635	4.97600E-08	8.62200E-09	1.95575E-14	1.29979E-15
242.892	8.10800E-09	4.78690E-09	7.21350E-15	1.22445E-15
244.416	1.81140E-09	3.53420E-10	5.36850E-16	7.74645E-17
247.370	1.42680E-09	7.10300E-10	7.97800E-16	1.17803E-16
248.894	9.93300E-10	8.18560E-10	1.07730E-15	3.26427E-16
265.981	4.28190E-08	1.95300E-08	3.23100E-14	7.56394E-16
266.743	2.08480E-08	5.24180E-09	1.03170E-14	3.45683E-16
275.213	2.40640E-08	8.68600E-09	1.50800E-14	4.30139E-16
276.737	5.79600E-09	1.32020E-09	3.12625E-15	2.75150E-16
299.718	3.95730E-08	1.16980E-08	2.06900E-14	3.43889E-16
301.242	1.65880E-08	3.11710E-09	6.88575E-15	2.30324E-16
303.869	1.89040E-08	5.99880E-09	1.05438E-14	3.38311E-16
306.151	9.26300E-09	2.42640E-09	4.47475E-15	2.42883E-16
307.675	5.34000E-09	9.44600E-10	2.07425E-15	1.30185E-16
318.047	1.18610E-07	4.40360E-08	7.79100E-14	1.58536E-15
324.472	1.25380E-08	3.18020E-09	6.83725E-15	3.60763E-16
328.793	6.75900E-09	2.25410E-09	3.48225E-15	3.35601E-16
329.555	3.47610E-09	9.90800E-10	2.88100E-15	4.43202E-16
333.655	3.99770E-09	1.86170E-09	3.32475E-15	2.02556E-16
340.081	2.57910E-09	1.28170E-09	2.43050E-15	1.75595E-16
344.272	2.26090E-09	8.17200E-10	1.36680E-15	1.49879E-16
345.796	1.66390E-09	8.46400E-10	1.24925E-15	1.74580E-16
347.749	1.12540E-09	6.37840E-10	8.93950E-16	1.04203E-16
349.273	1.13290E-09	1.01223E-09	1.89555E-15	3.64679E-16

Table.4.11 : Losses for each wire scanner (number per primary proton).

Wire Scanner	Loss (p^{-1})	Dist from L61 (m)
PM111 (wire)	8.30E-5	164.74
PM112 (wire)	7.23E-6	173.85
PM114 (wire)	7.23E-6	250.11
PM115 (foil)	7.23E-6	265.01
PM117 (foil)	7.23E-6	298.33
PM118 (foil)	8.30E-5	309.11
PM121 (foil)	7.23E-6	351.86
PMTGT (foil)	7.23E-6	364.31

4.5 Beam Loss Correlations

There are no magnetic elements in first two regions. The main source of radiation there is from beam loss near the HQ111 or HQ112 quadrupoles. It is natural to suppose the following simple relations:

$$S_1 = \alpha_1^{111} \cdot L_{HQ111}$$
$$S_1 = \alpha_1^{112} \cdot L_{HQ112}$$
$$S_2 = \alpha_2^{111} \cdot L_{HQ111}$$
$$S_2 = \alpha_2^{112} \cdot L_{HQ112}$$

where S_1, S_2 are average star densities in regions 1,2 and L_{HQ111}, L_{HQ112} are number of protons lost on HQ111, HQ112, respectively. For other regions we suppose

$$S_i = \alpha_i \cdot L_i,$$

where S_i is average star density in region i and L_i is beam loss in this region. Using data from tables 4.3 and 4.5 one can estimate the correlation constants. Results are presented in tables 4.12-13. It is seen that in most cases α_i has a weak dependence on the loss scenario.

Using the above relations, constants from tables 4.12-13 and star density limits, it is possible to estimate the maximum beam loss which could be allowed on different magnets. Acceptable beam loss limits are presented in table 4.14.

Table.4.12 : Constants for estimation of the average star density (star/cc/proton) in 99.9% volume.

source	α_1^{111}	α_1^{112}	α_2^{111}	α_2^{112}
HV101 1.20%		2.3×10^{-8}		7.3×10^{-9}
HV101 1.25%		2.1×10^{-8}		6.5×10^{-9}
HV101 1.40%		1.4×10^{-8}		4.0×10^{-9}
HV101 1.50%		1.5×10^{-8}		5.6×10^{-9}
V108 0.75%	9.3×10^{-9}		1.9×10^{-9}	
V108 0.78%	1.0×10^{-8}		1.8×10^{-9}	
V108 0.85%	1.6×10^{-8}		3.6×10^{-9}	
V108 0.90%	1.7×10^{-8}		6.5×10^{-9}	
comb 1		1.6×10^{-8}		4.9×10^{-9}
comb 2	1.1×10^{-8}		4.3×10^{-9}	
comb 3	0.8×10^{-8}		2.2×10^{-9}	
wire	1.8×10^{-8}	1.8×10^{-8}	4.2×10^{-9}	4.2×10^{-9}
average	1.3×10^{-8}	1.8×10^{-8}	3.5×10^{-9}	5.4×10^{-9}

Table.4.13 : Constants for estimation of the average star density (star/cc/proton) in 99.9% volume.

source	α_3	α_4	α_5	α_6	α_7
HV101 1.20%		8.1×10^{-8}	2.7×10^{-8}		
HV101 1.25%		7.6×10^{-8}	2.8×10^{-8}		
HV101 1.40%		8.9×10^{-8}			
HV101 1.50%					
V108 0.75%				2.3×10^{-8}	1.5×10^{-8}
V108 0.78%				1.3×10^{-8}	1.6×10^{-8}
V108 0.85%				1.8×10^{-8}	
V108 0.90%					
comb 1					
comb 2	1.3×10^{-7}	9.9×10^{-8}			
comb 3				2.0×10^{-8}	
wire	1.5×10^{-7}	7.7×10^{-8}			2.2×10^{-8}
average	1.4×10^{-7}	8.4×10^{-8}	2.8×10^{-8}	1.9×10^{-8}	1.8×10^{-8}

Table.4.14 : Maximum acceptable losses from operational beam loss limit.

region	star density limit star/cc/proton	beam loss limit particle/proton	place
1	6.4×10^{-4}	1	HQ111,HQ112
2	2.1×10^{-12}	6.0×10^{-4}	HQ111
2	2.1×10^{-12}	4.0×10^{-4}	HQ112
3	5.7×10^{-10}	4.1×10^{-3}	HQ113
4	4.8×10^{-10}	5.7×10^{-3}	V118-1 or HT117
5	6.4×10^{-10}	2.3×10^{-2}	V118-2
6	6.4×10^{-10}	3.4×10^{-2}	V118-4
7	6.4×10^{-10}	3.6×10^{-2}	HT121

Appendix A

MARS Model Elements

This Appendix contains drawings of the MARS model beamline, showing transverse and longitudinal cross sections of magnets and cross sections of the NuMI tunnel as modeled.

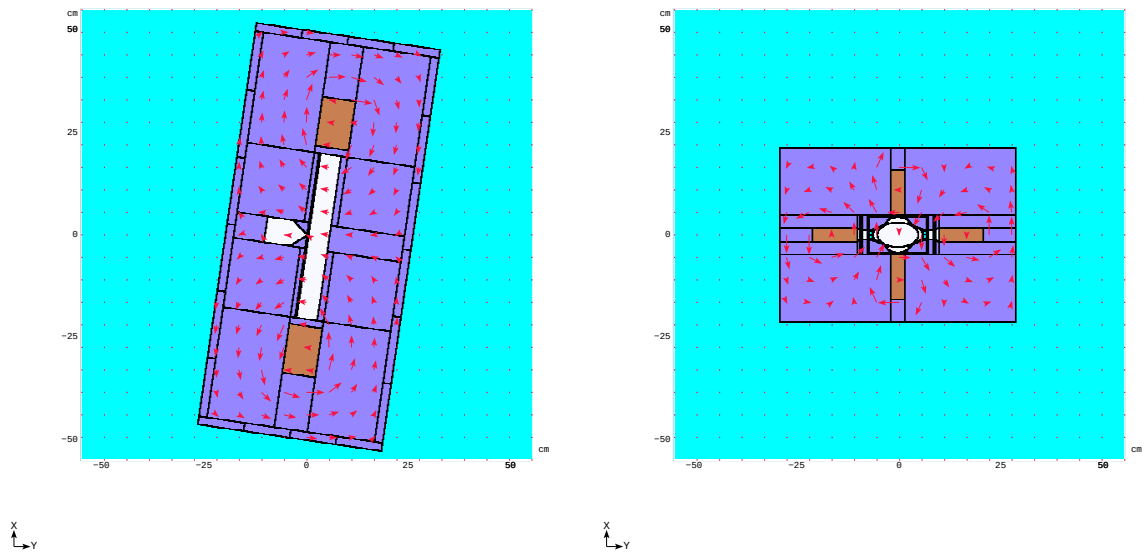

Figure A.1: LAM60 (Lambertson) and Q608 (3Q84) magnets.

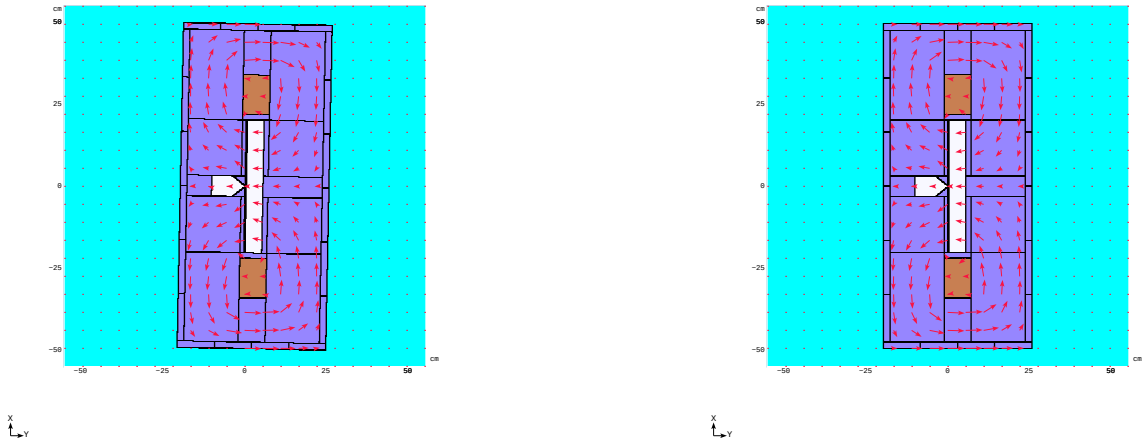

Figure A.2: LAM61A and LAM61B (Lambertson) magnets.

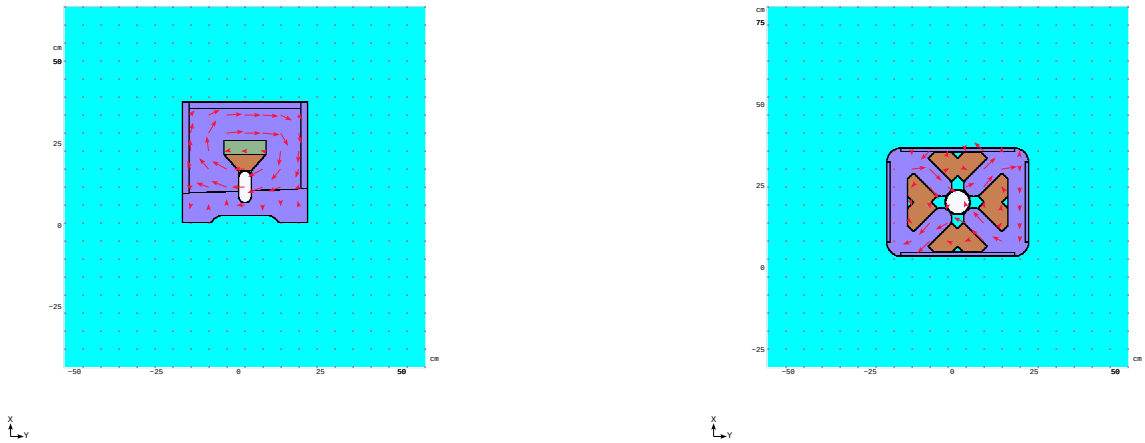

Figure A.3: V100 (C) and Q101 (3Q120-old) magnets.

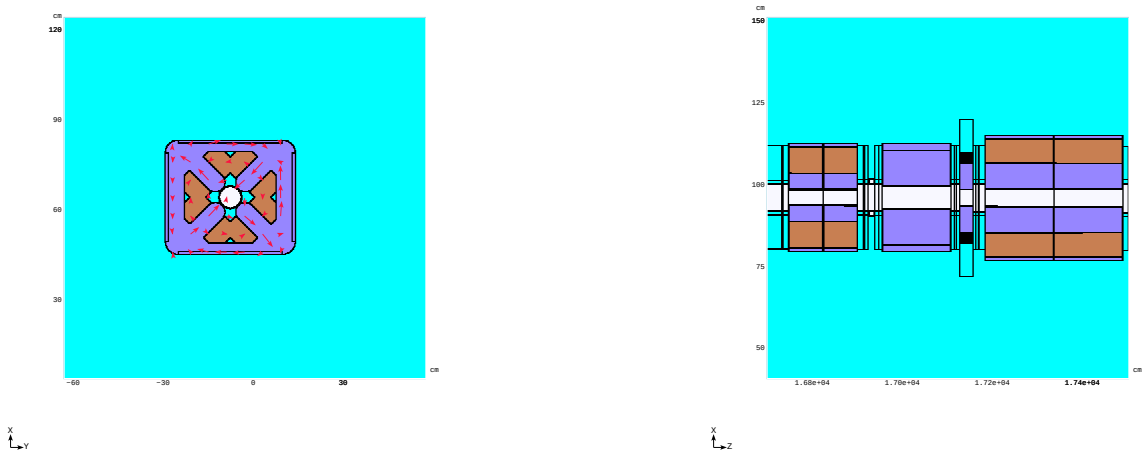

Figure A.4: Q102(3Q120) and Q104(3Q60)-H104(trim)-HT105(trim)-Q105(3Q120) magnets.

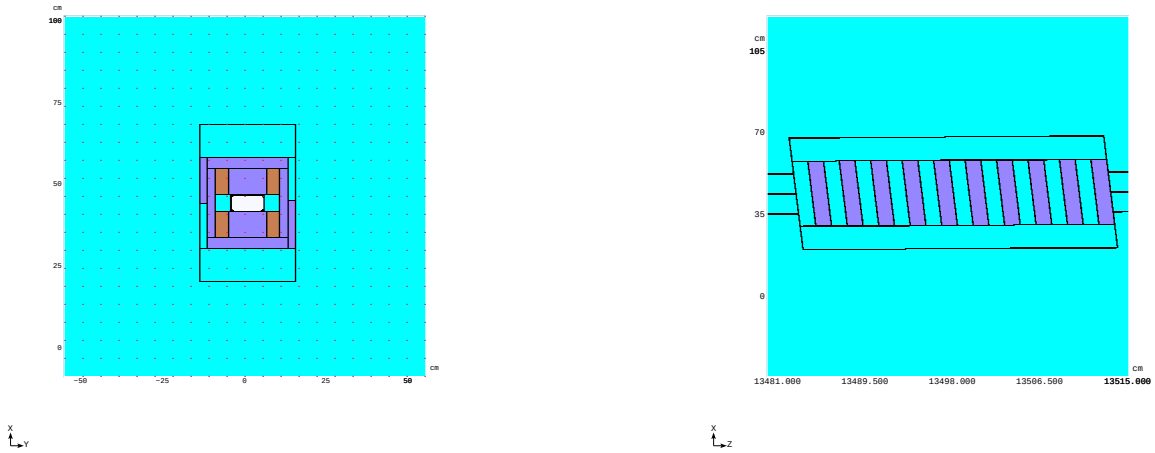

Figure A.5: HT102 (trim) magnet.

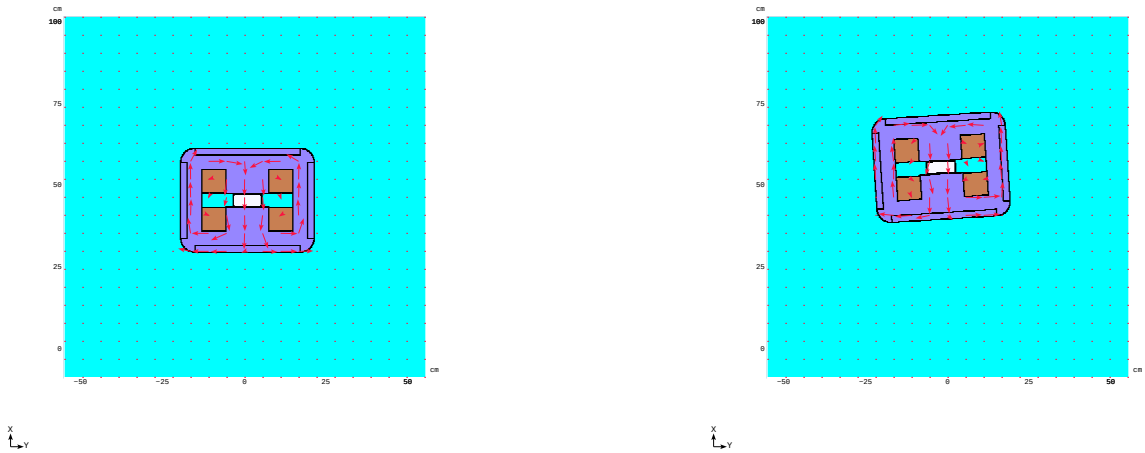

Figure A.6: HV101-1 and HV101-2 (EPB) magnets.

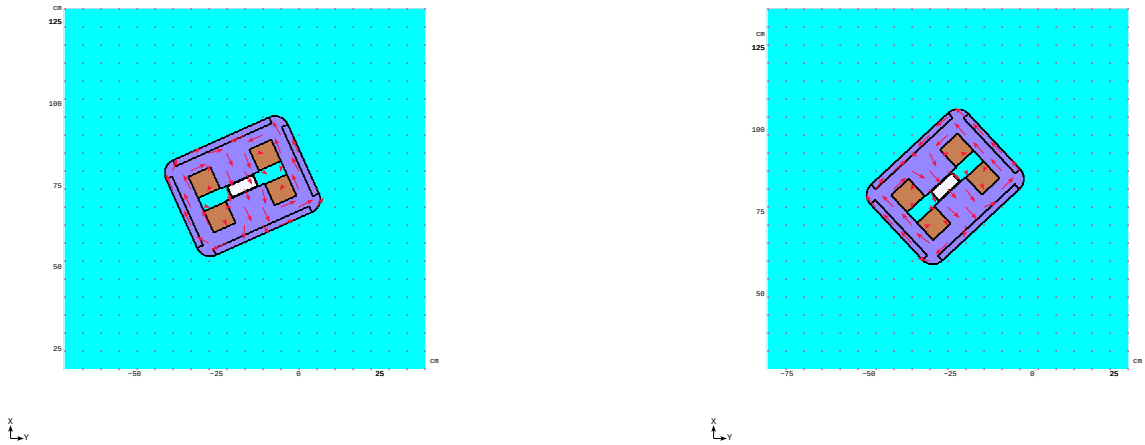

Figure A.7: HV101-3 and HV101-4 (EPB) magnets.

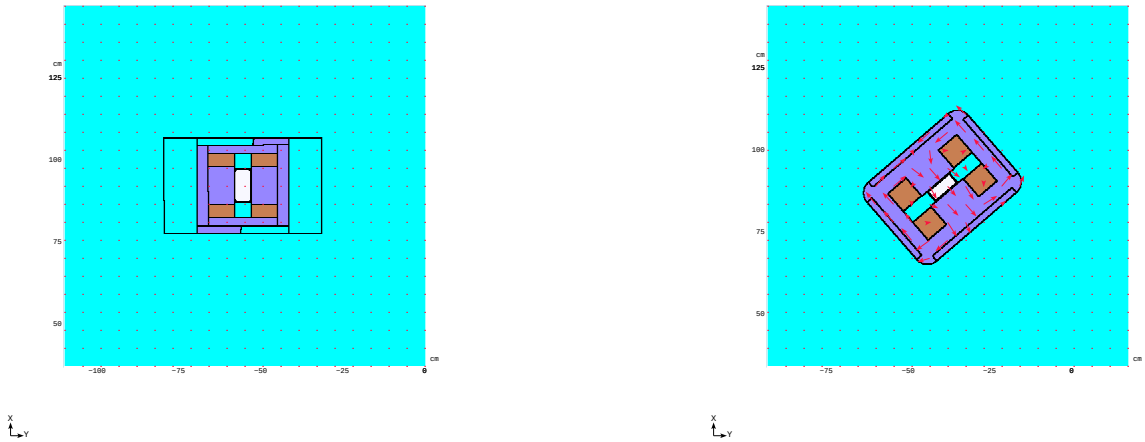

Figure A.8: VT103 (trim) and HV101-5 (EPB) magnets.

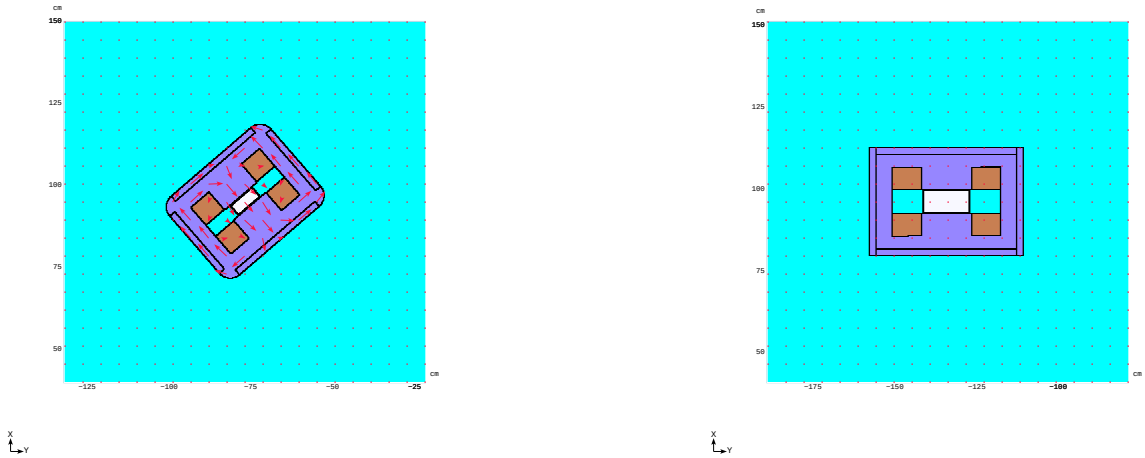

Figure A.9: HV101-6 (EPB) and H104 (trim dipole) magnets.

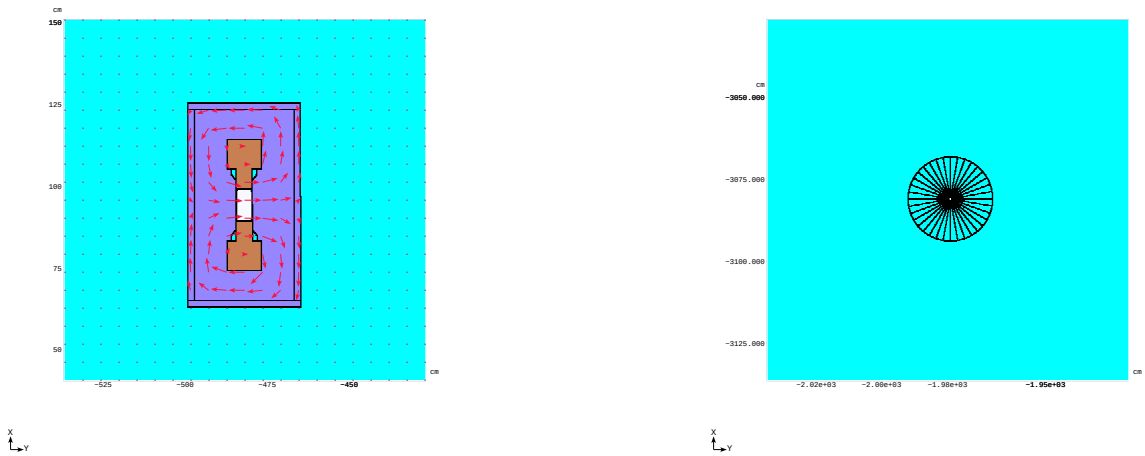

Figure A.10: V108-1 (B2) magnet and baffle.

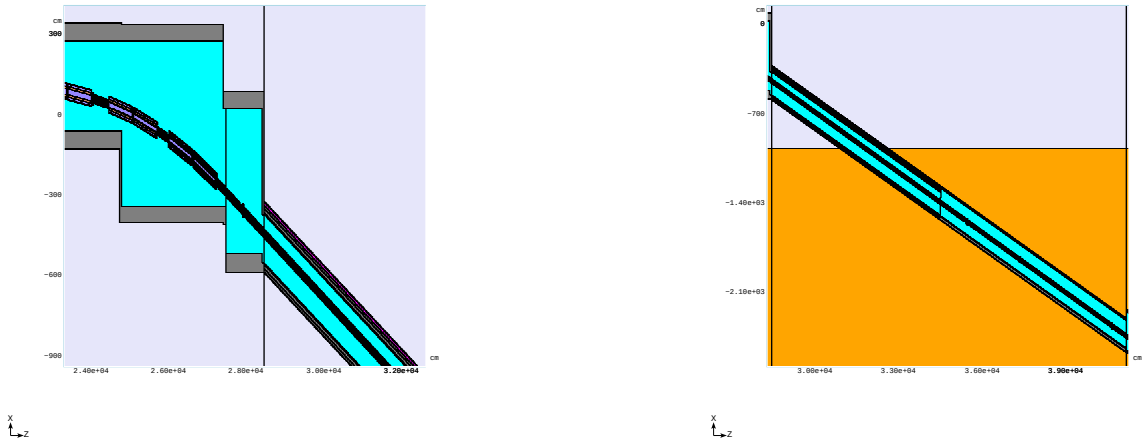

Figure A.11: Extraction enclosure, extraction enclosure extension and carrier tunnel.

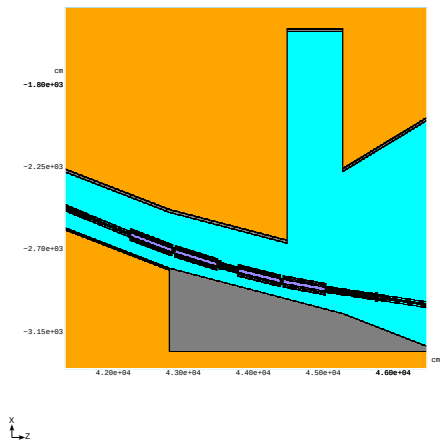

Figure A.12: Pretarget hall.

Figure A.13: Transverse cross section of NuMI tunnel in extraction enclosure (137 m) and extraction enclosure extension (164 m).

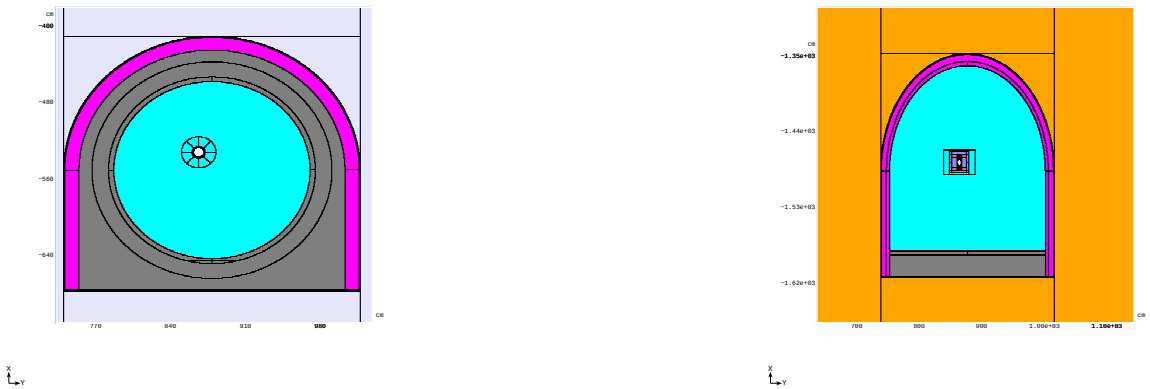

Figure A.14: Transverse cross section of NuMI tunnel in carrier tunnel 177 m and at 237 m).

Figure A.15: Transverse cross section of NuMI tunnel in carrier tunnel 307 m and at 317 m).

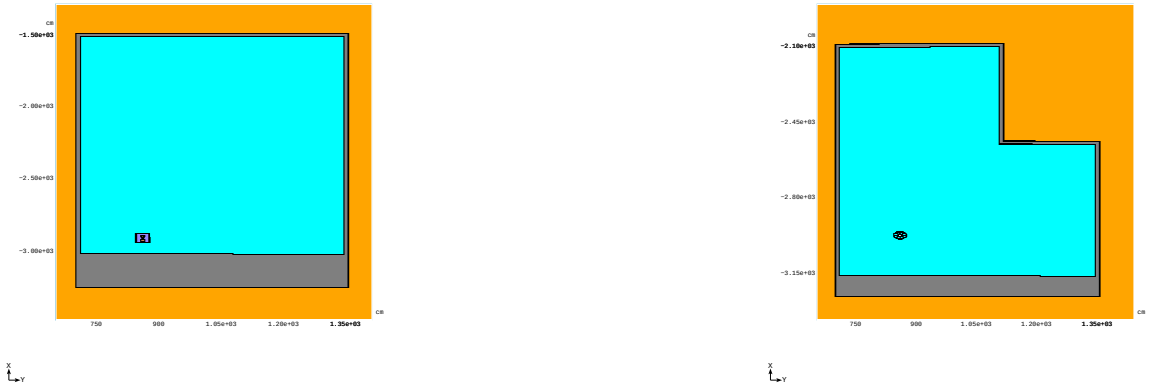

Figure A.16: Transverse cross section of NuMI tunnel in carrier tunnel 337 m and at 347 m).

Appendix B

Star Density Distributions

Star densities and residual dose distributions along the NuMI beamline for nine loss scenarios are presented this Appendix. For each case, four figures are shown: star density just within (1 cm) the tunnel wall for regions 1 through 3, and 4 through 7, spatial star density distribution for regions 1 through 3, and 4 through 7.

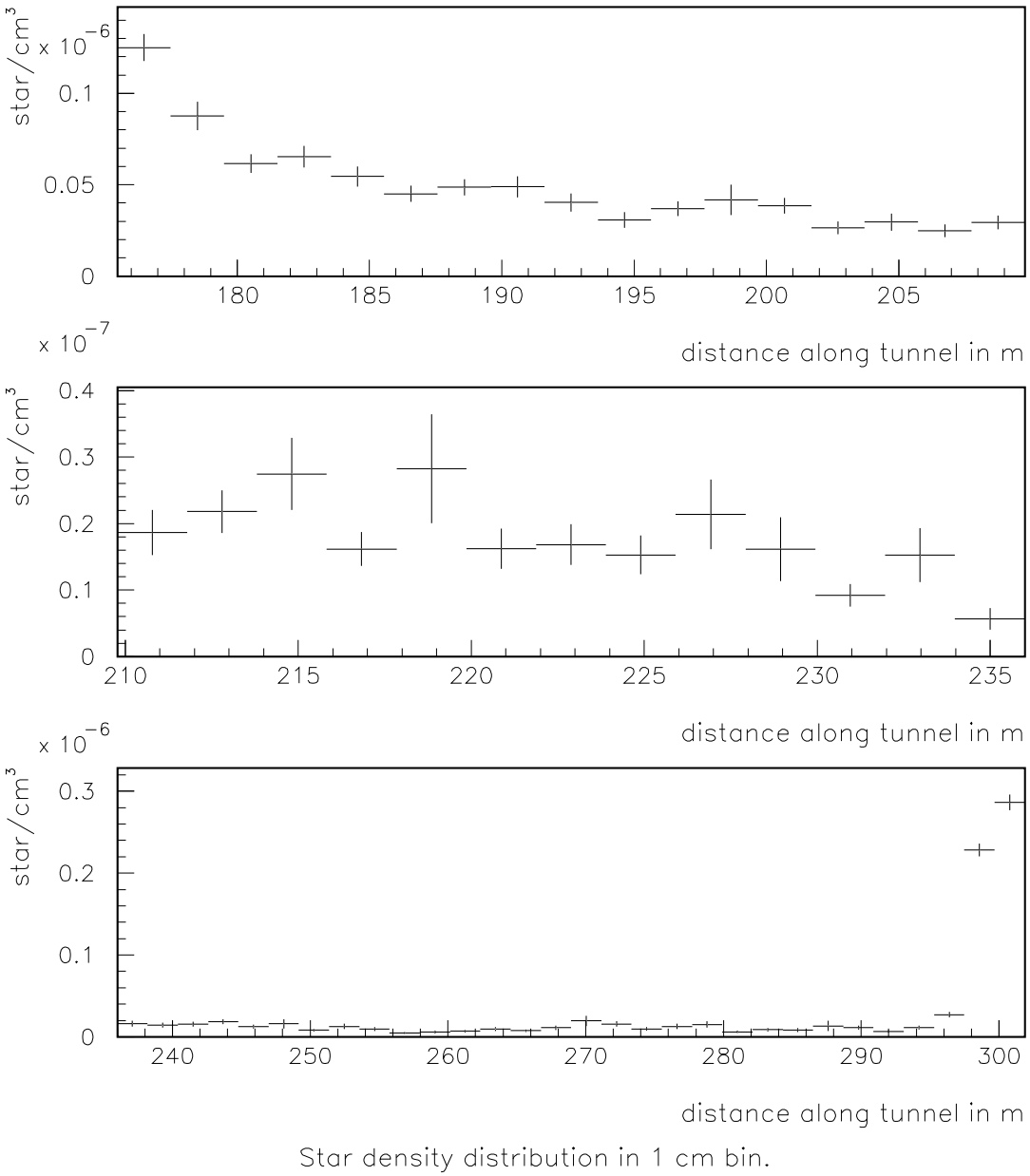

Figure B.1: Star density distribution for first three regions. Magnet current variation on 1.25% in HV101.

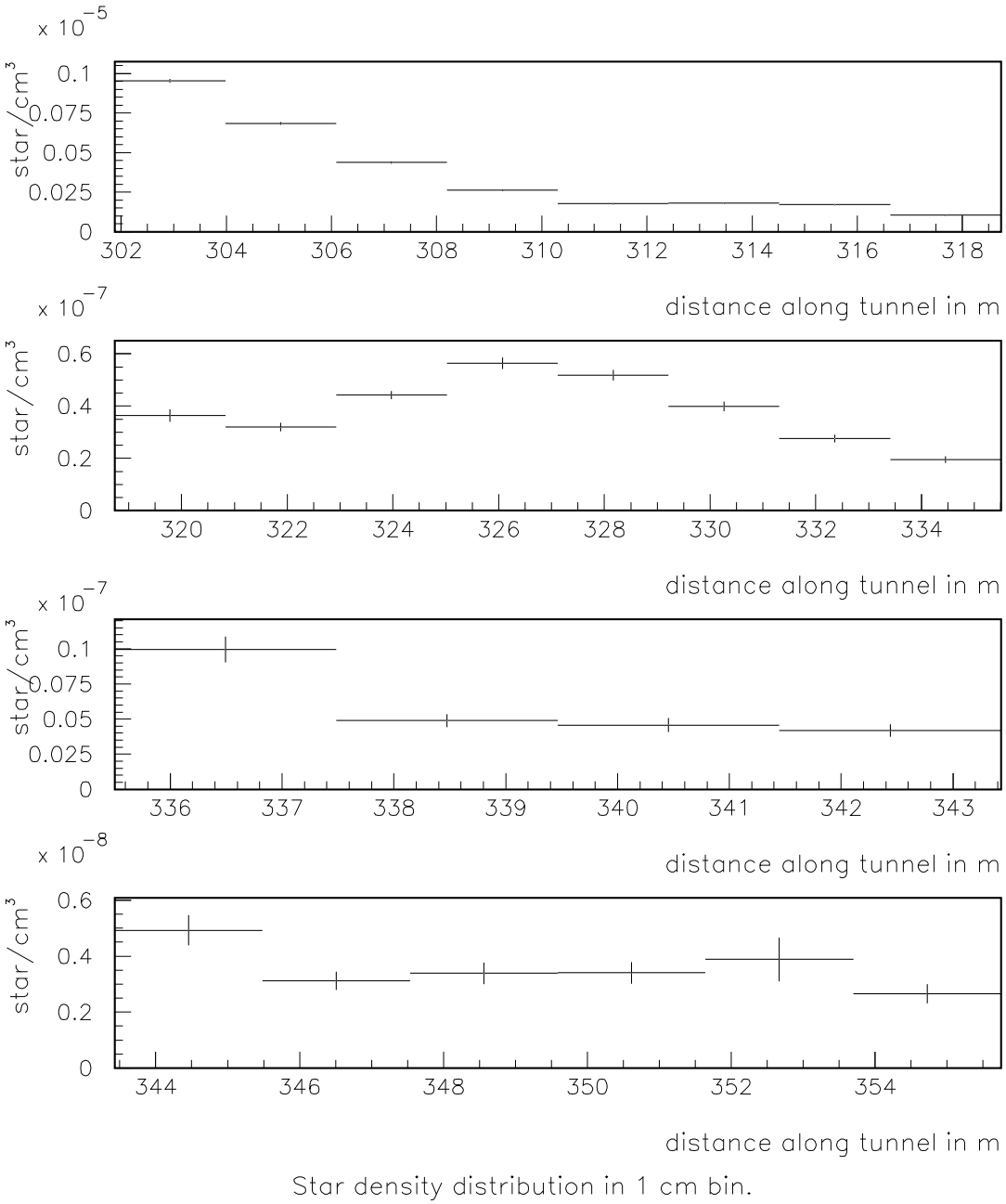

Figure B.2: Star density distribution for last four regions. Magnet current variation on 1.25% in HV101.

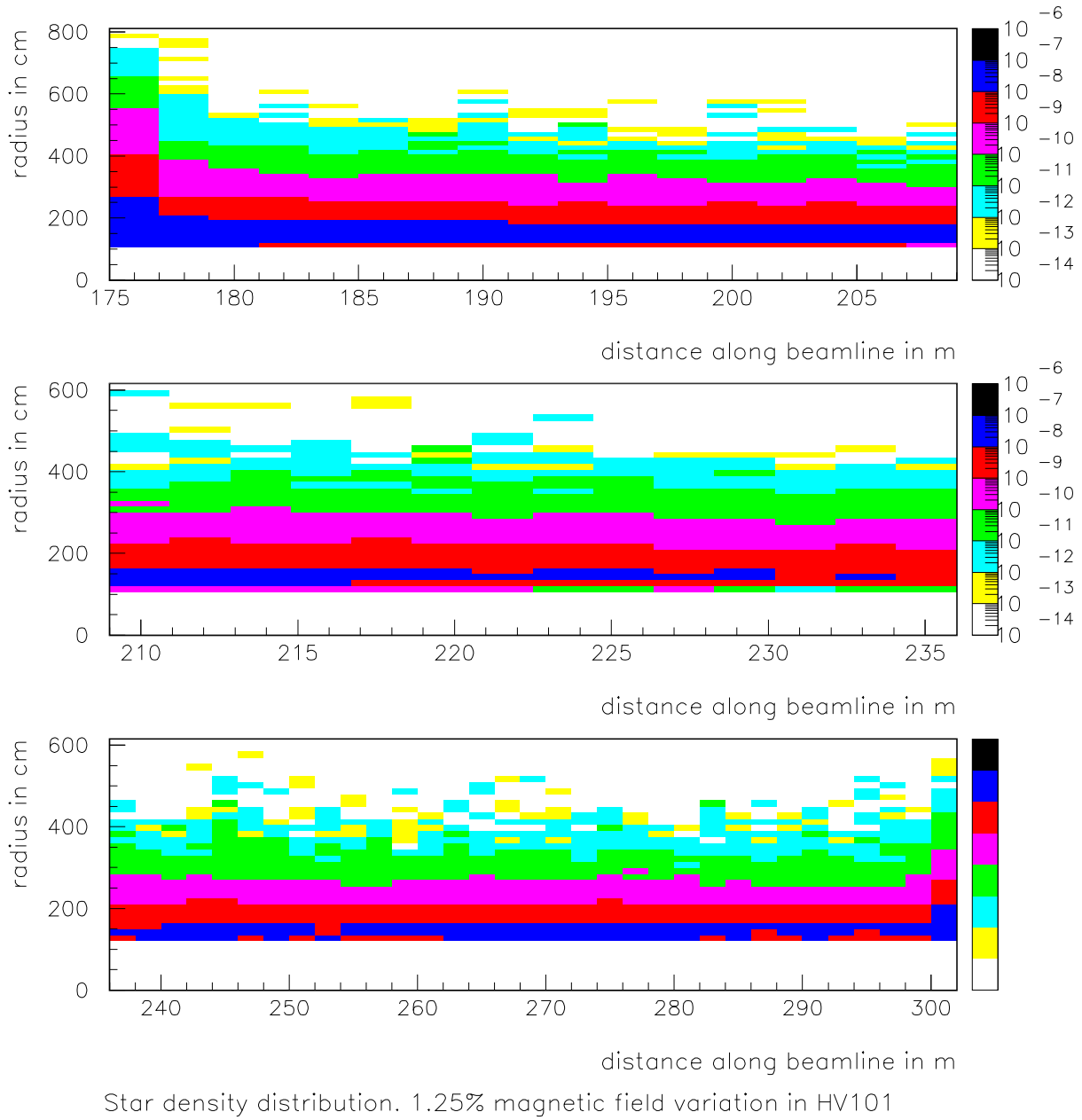

Figure B.3: Star density distribution for first three regions.

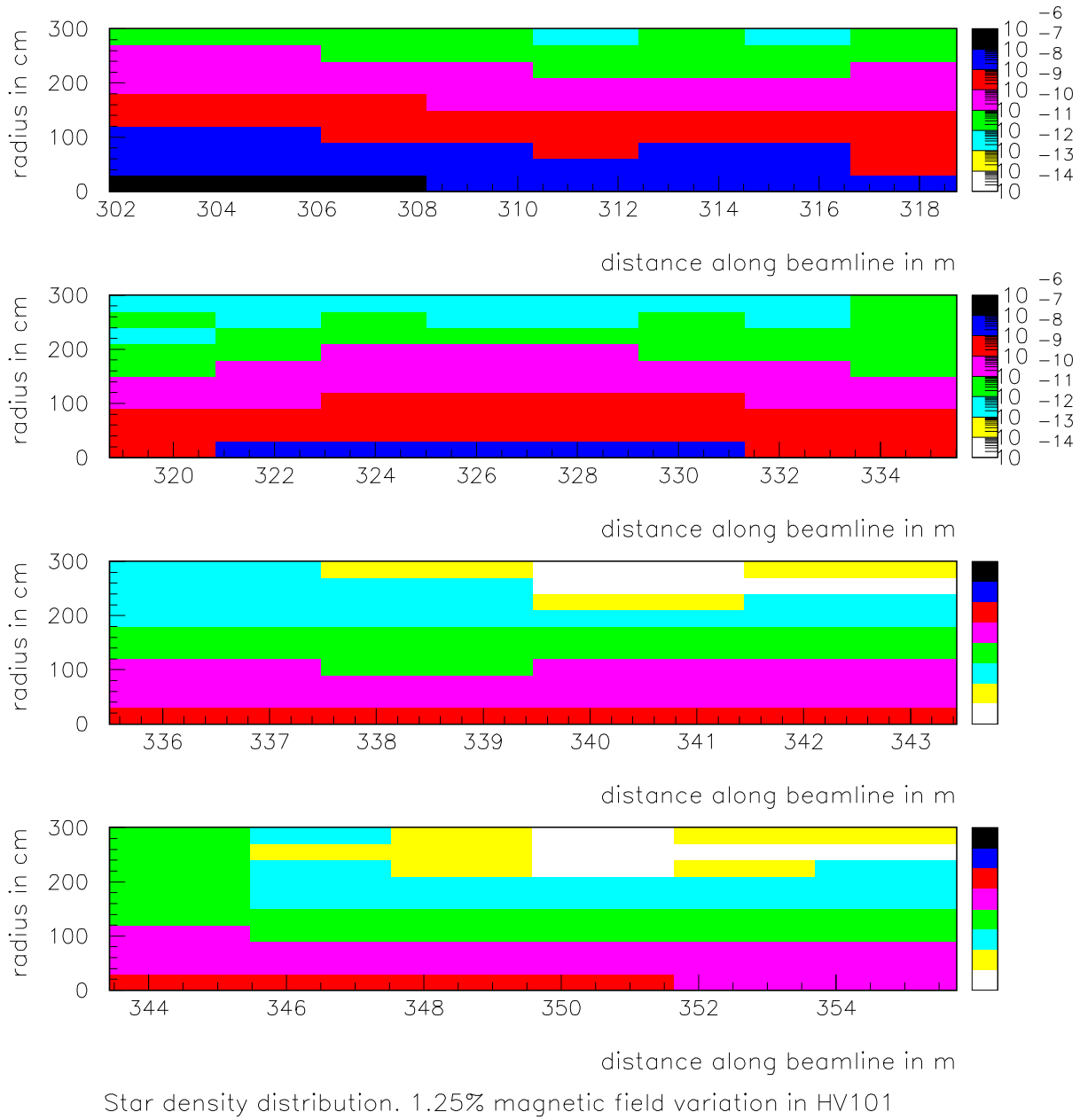

Figure B.4: Star density distribution for last four regions.

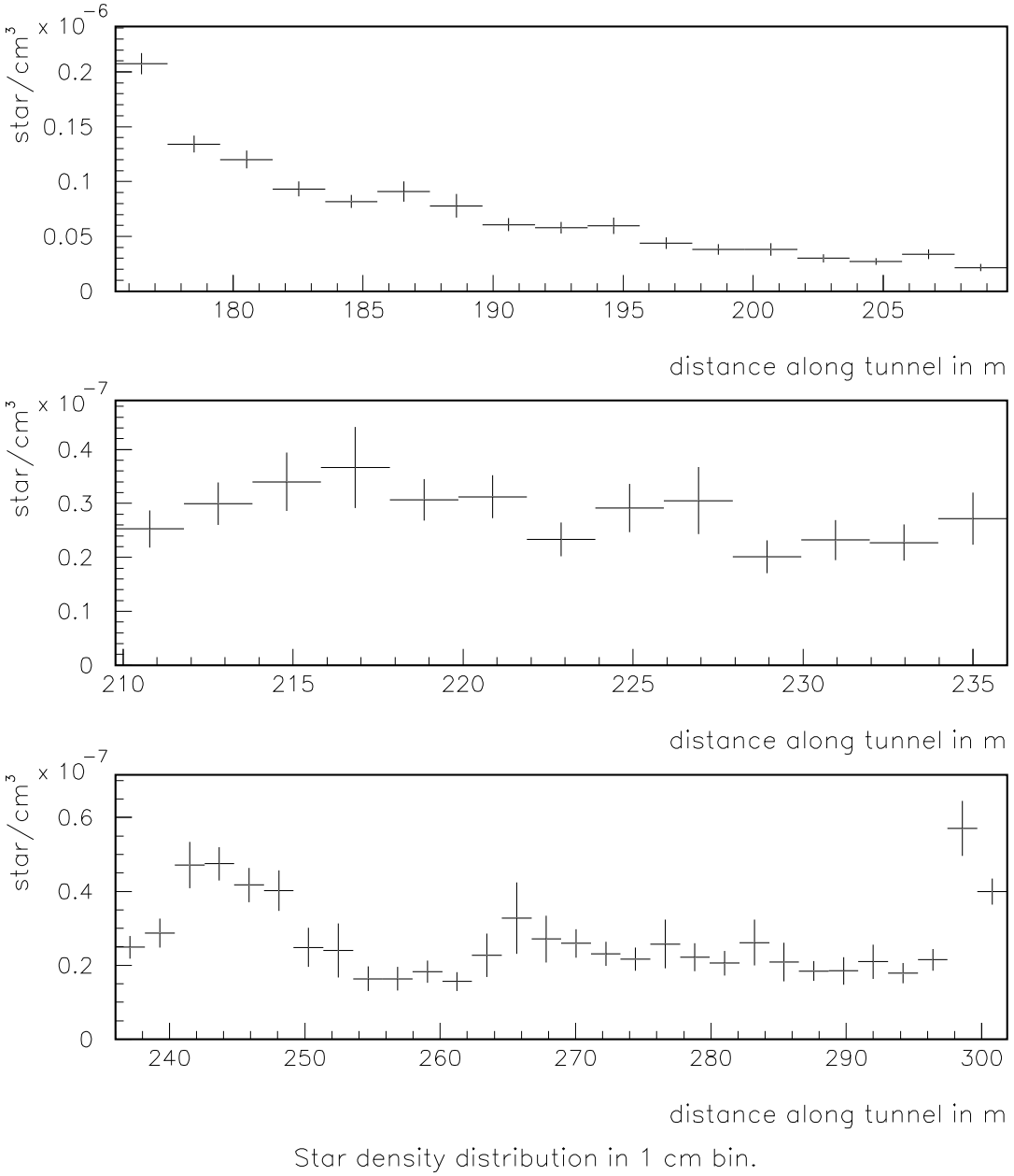

Figure B.5: Star density distribution for first three regions. Magnet current variation on 1.4% in HV101.

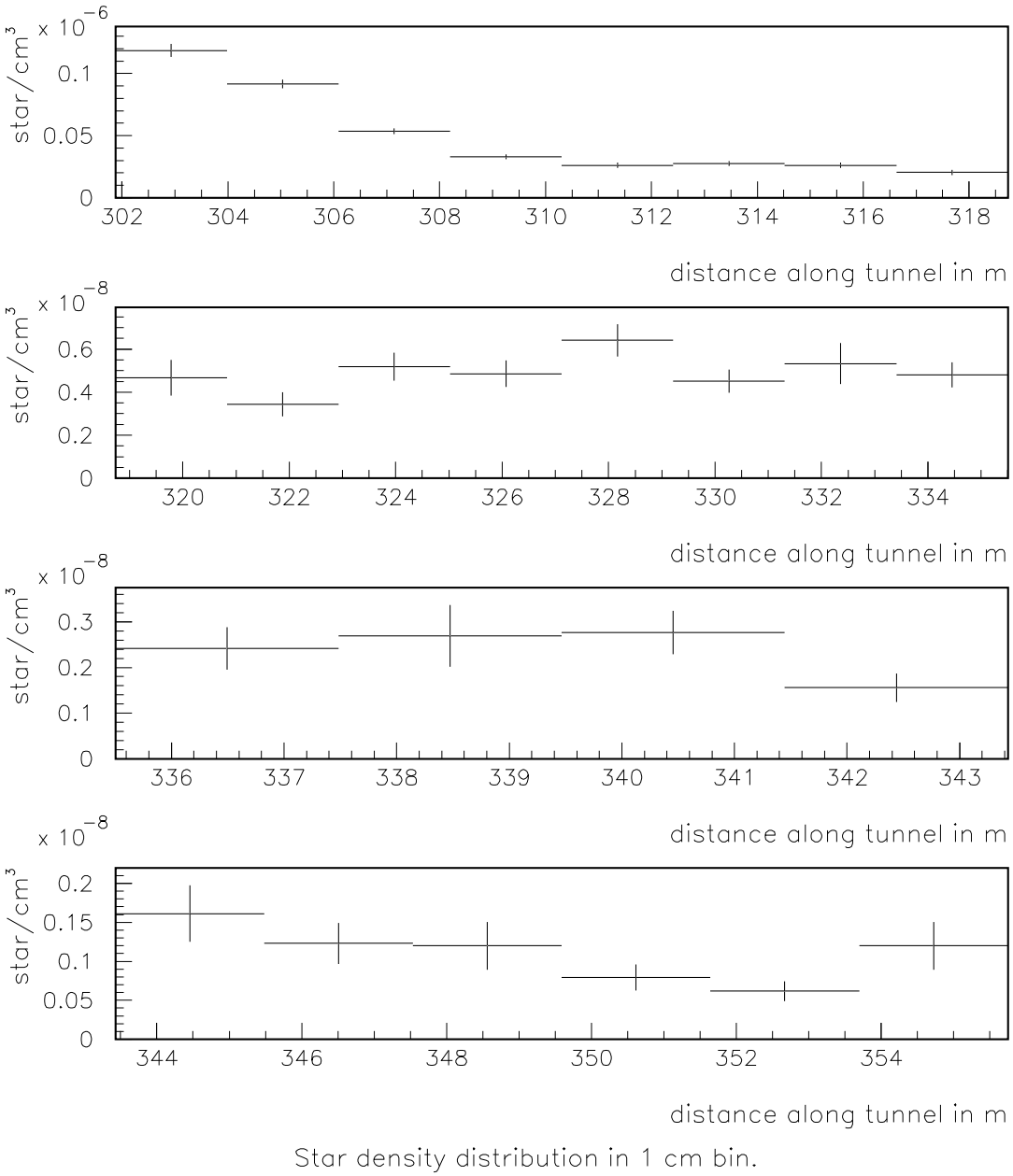

Figure B.6: Star density distribution for last four regions. Magnet current variation on 1.4% in HV101.

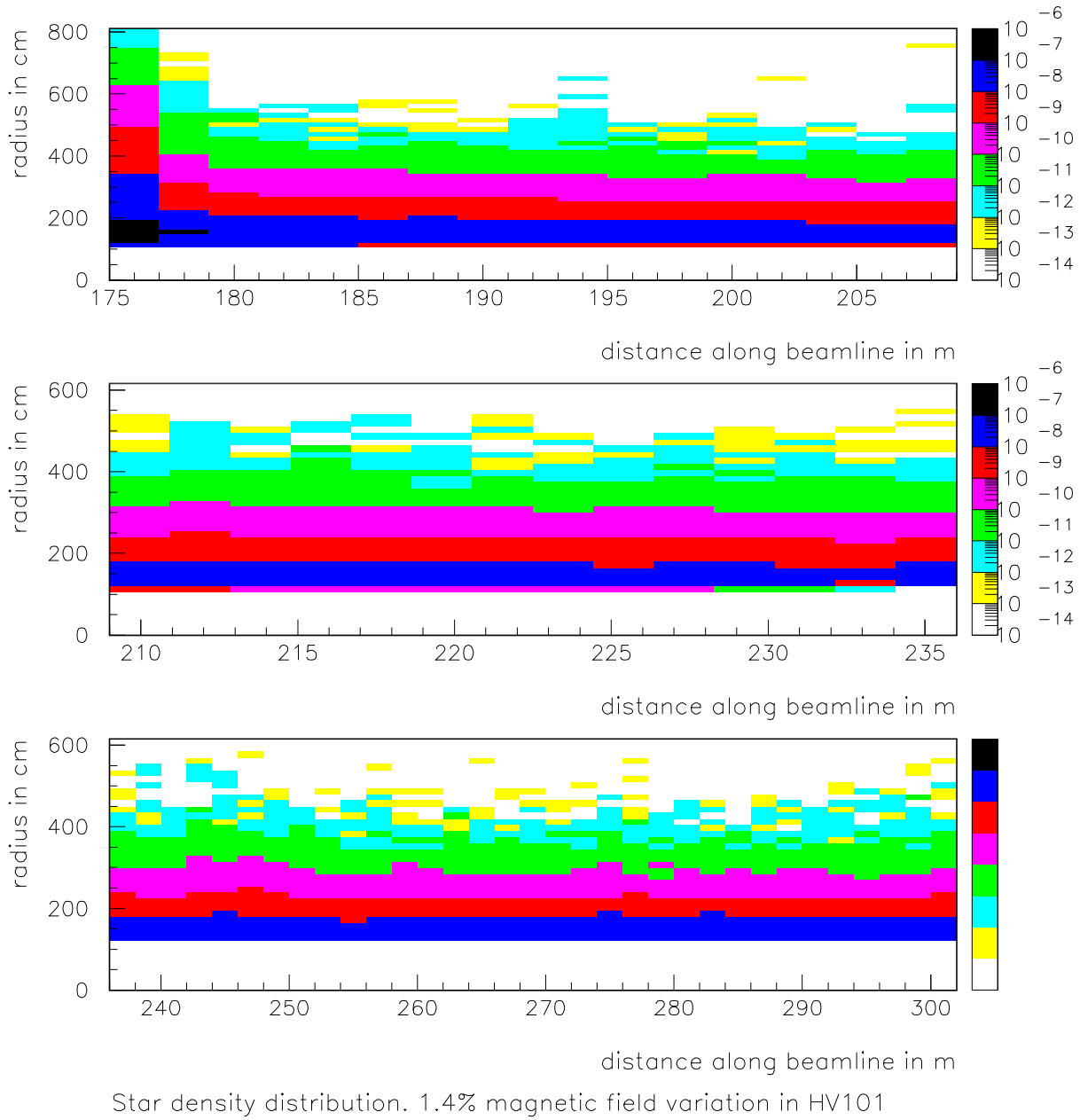

Figure B.7: Star density distribution for first three regions.

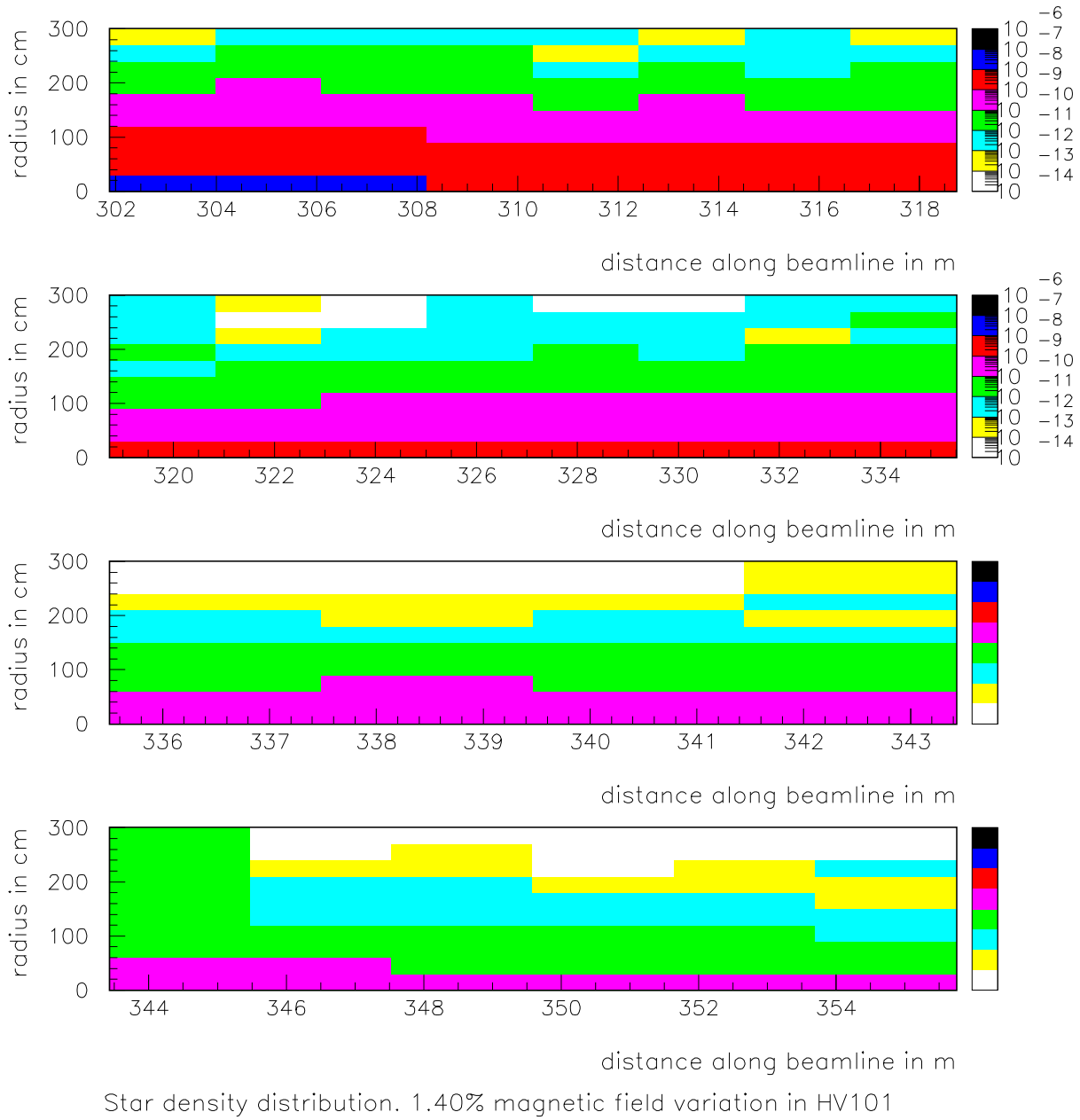

Figure B.8: Star density distribution for last four regions.

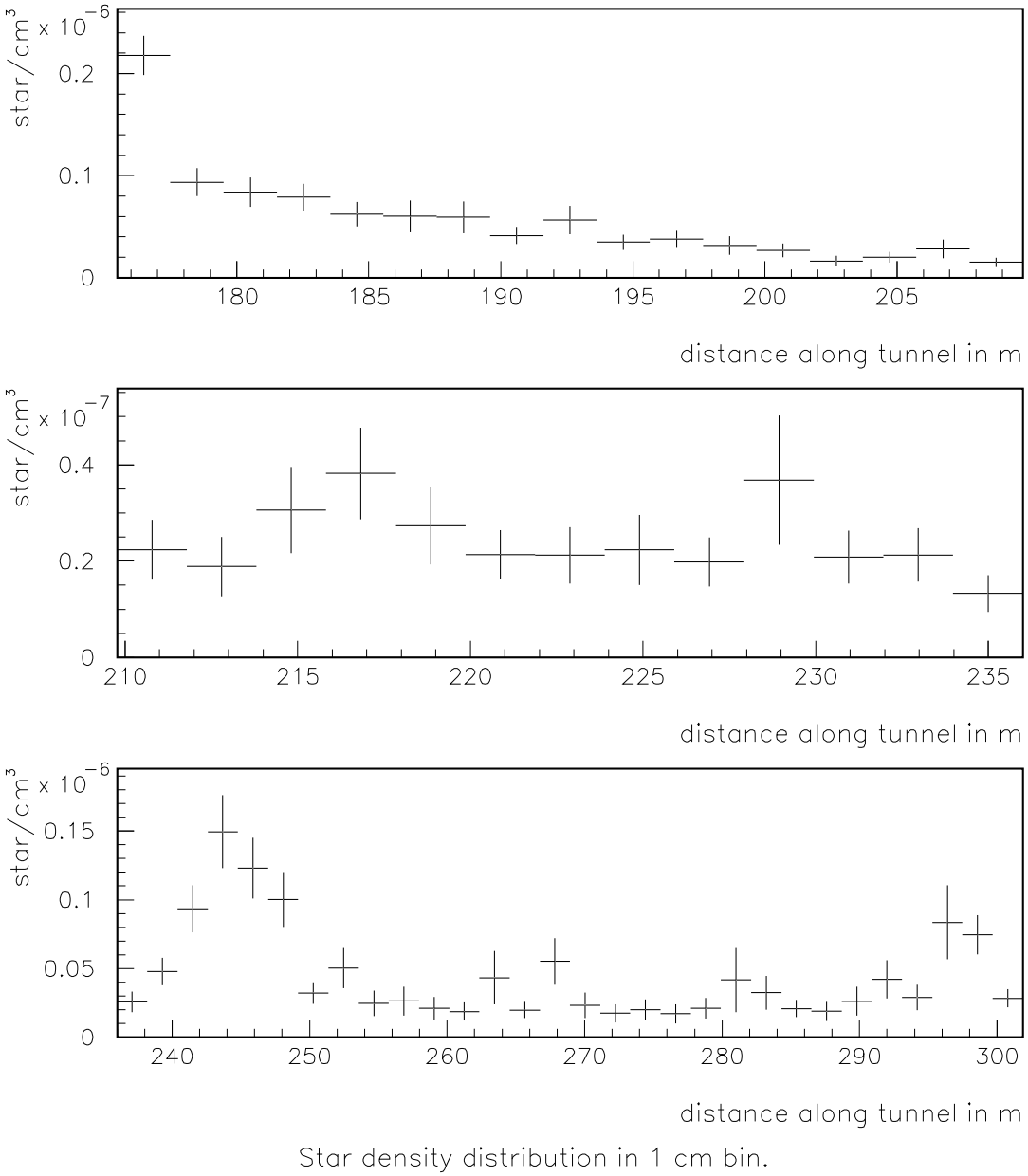

Figure B.9: Star density distribution for first three regions. Magnet current variation on 1.5% in HV101.

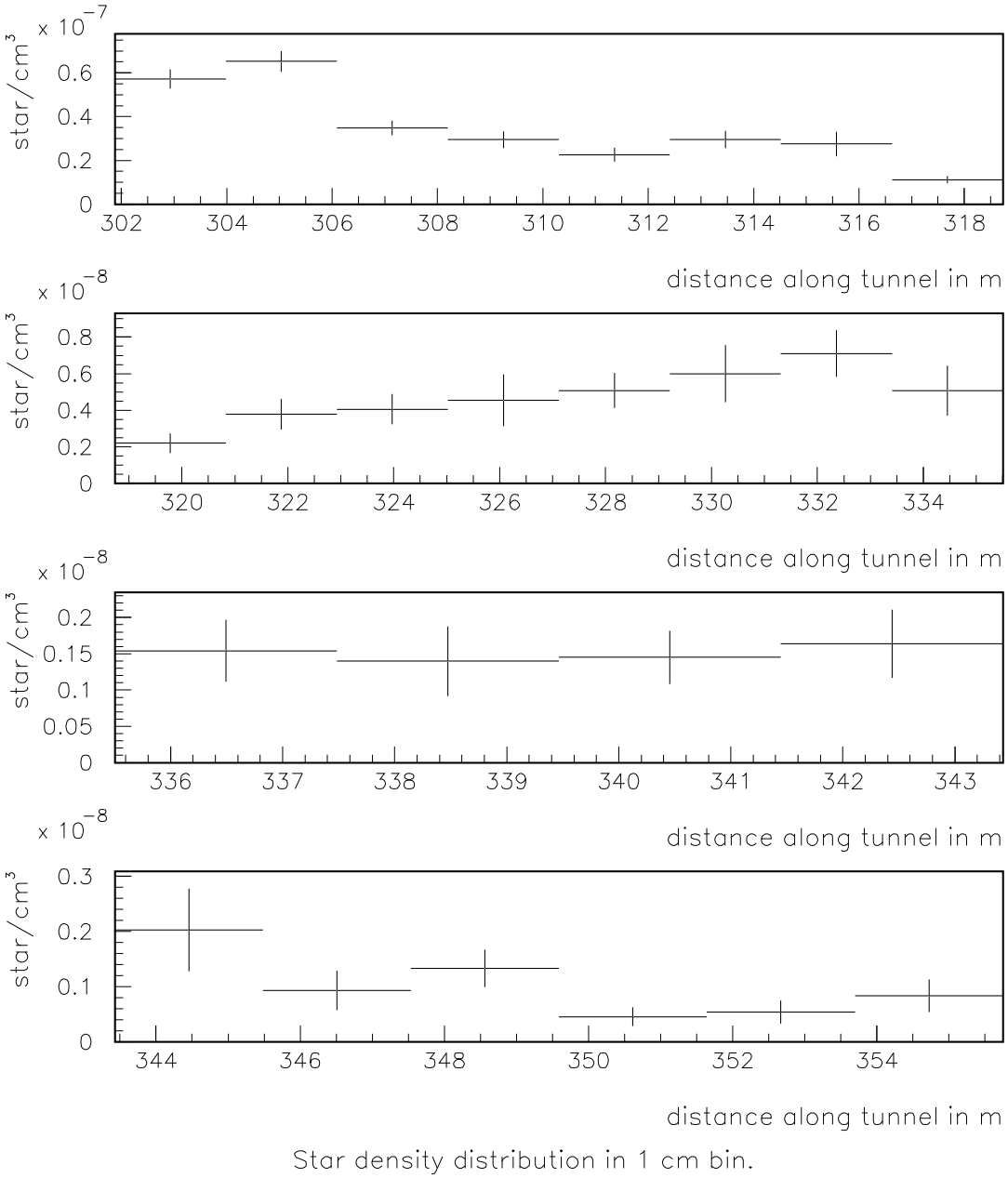

Figure B.10: Star density distribution for last four regions. Magnet current variation on 1.5% in HV101.

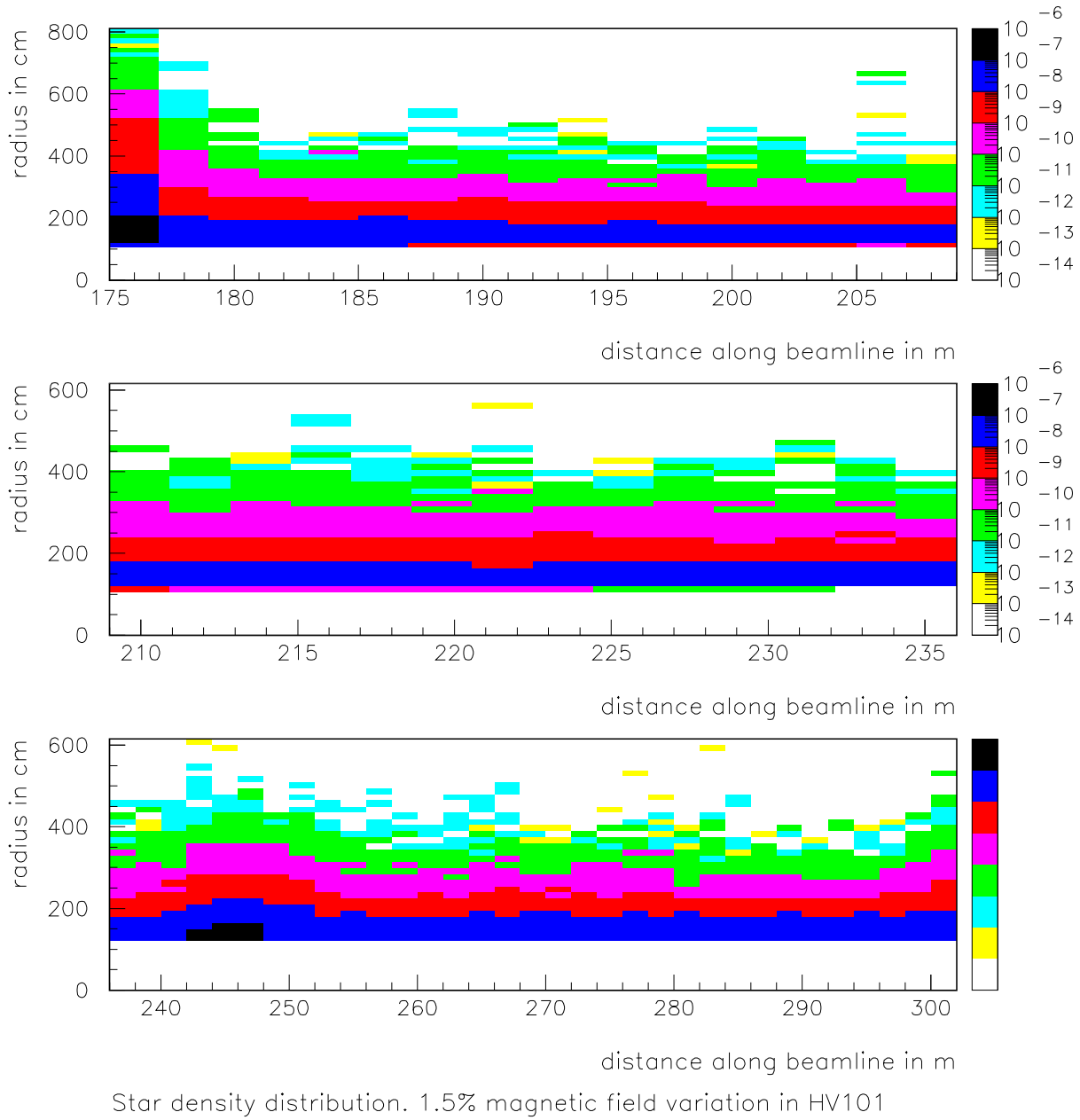

Figure B.11: Star density distribution for first three regions.

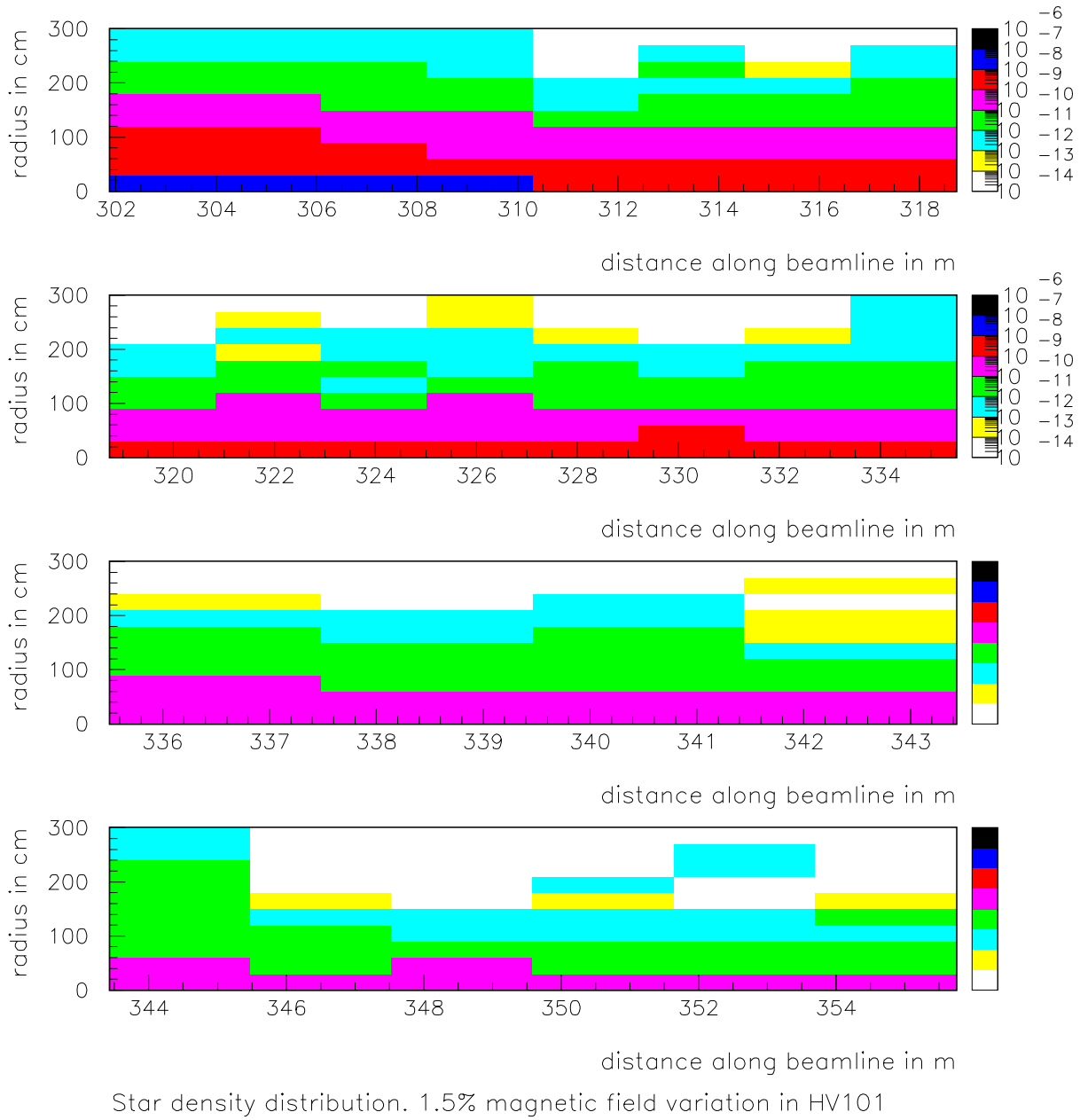

Figure B.12: Star density distribution for last four regions.

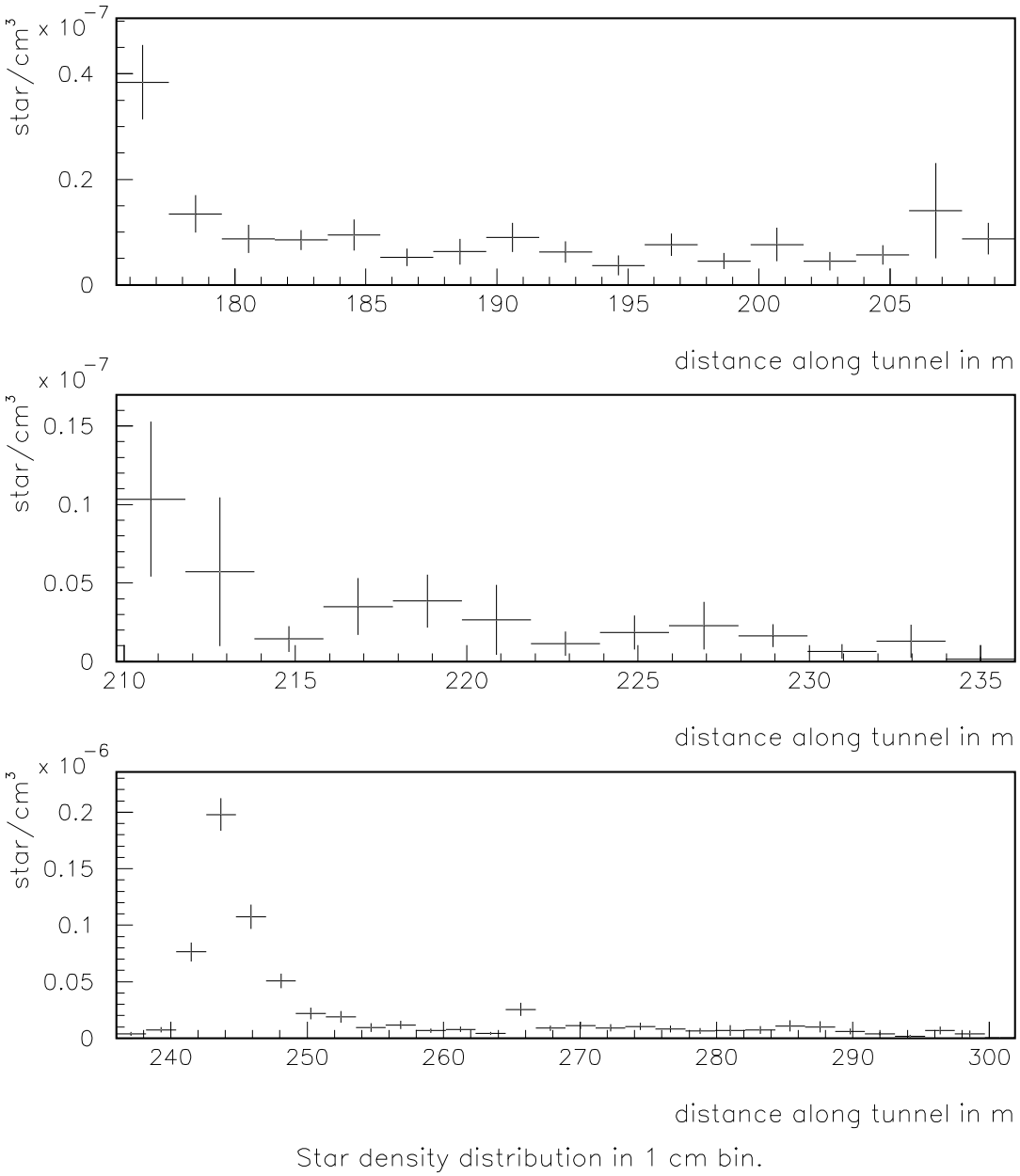

Figure B.13: Star density distribution for first three regions. Magnet current variation on 0.75% in V108.

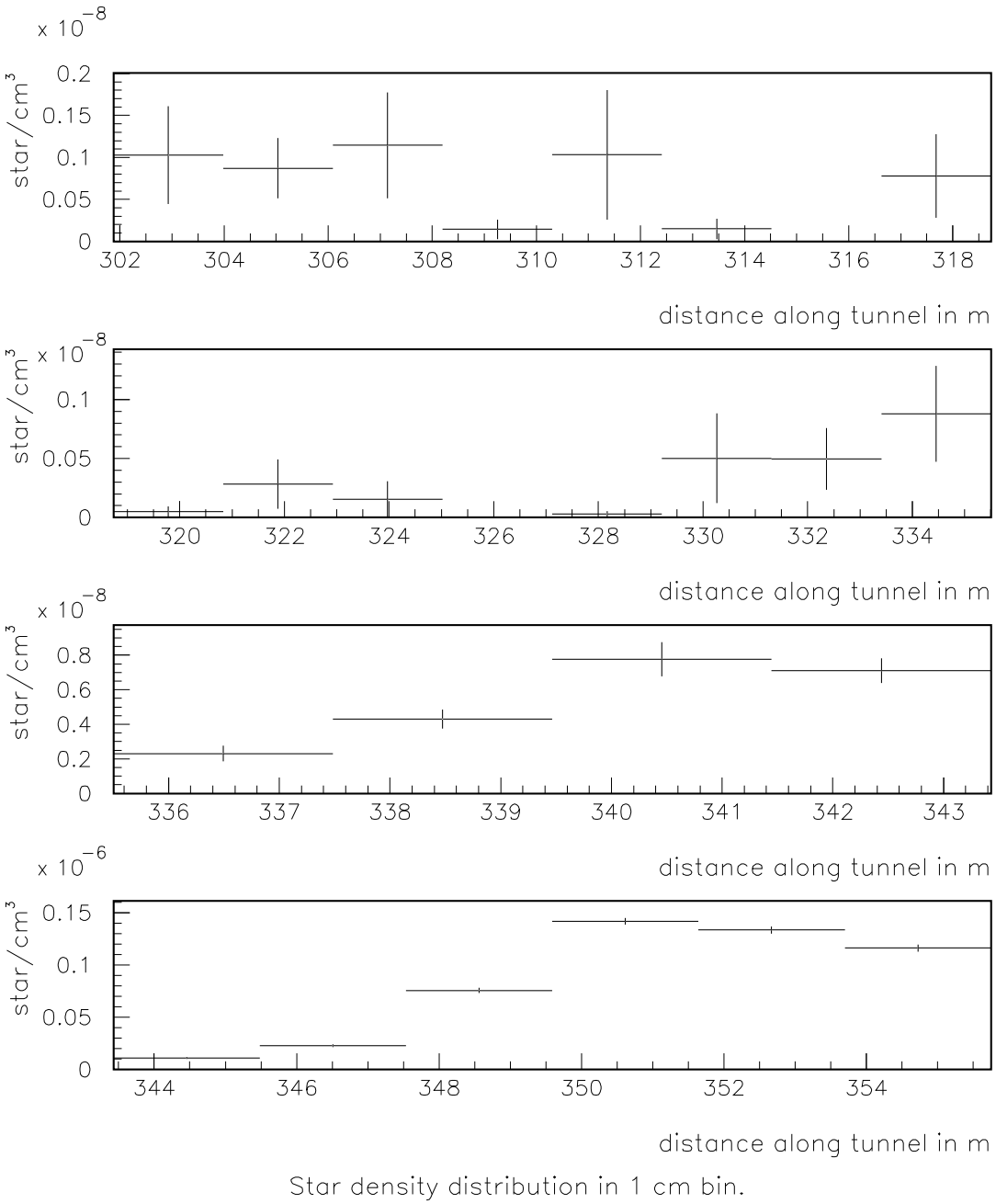

Figure B.14: Star density distribution for last four regions. Magnet current variation on 0.75% in V108.

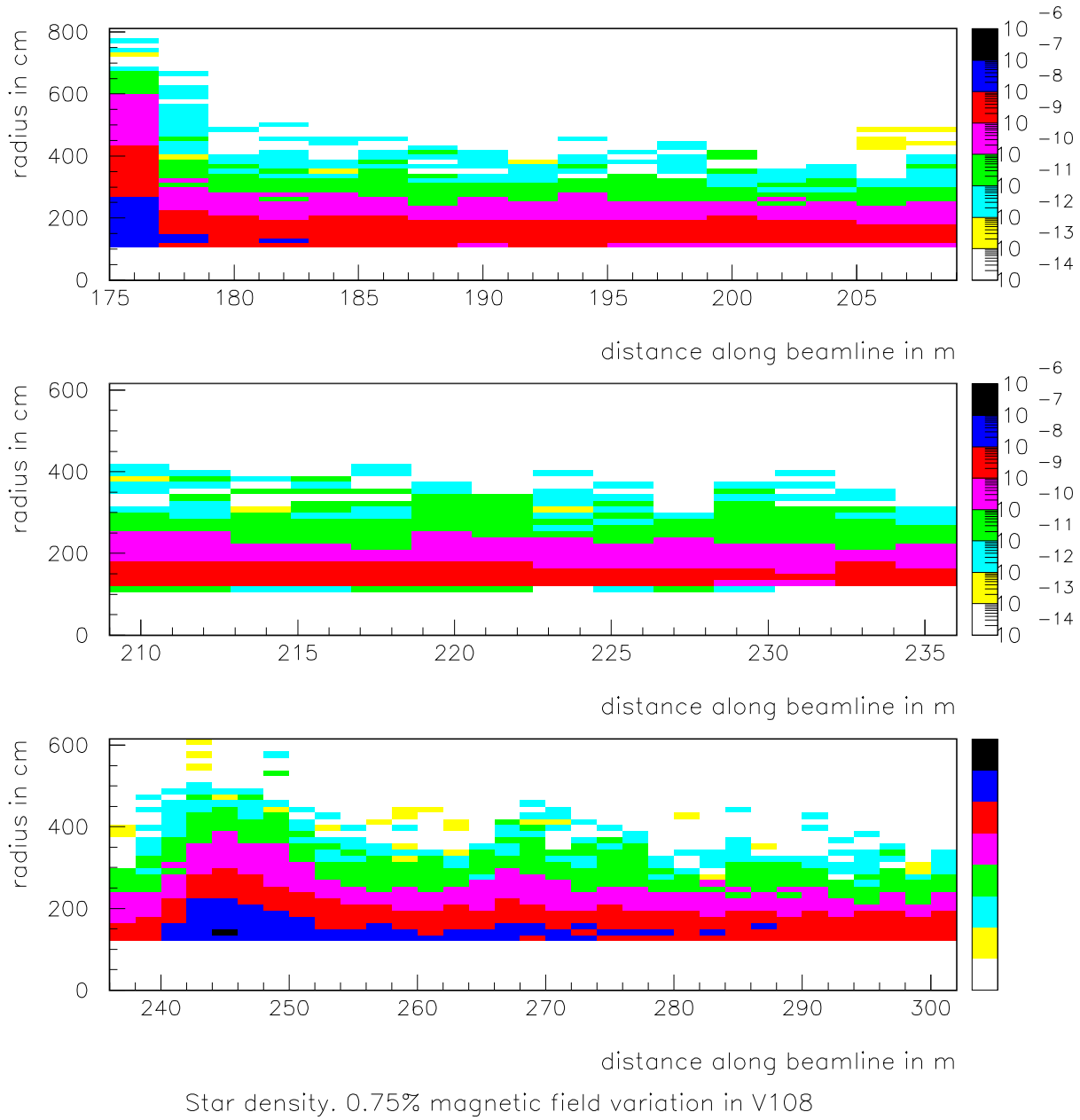

Figure B.15: Star density distribution for first three regions.

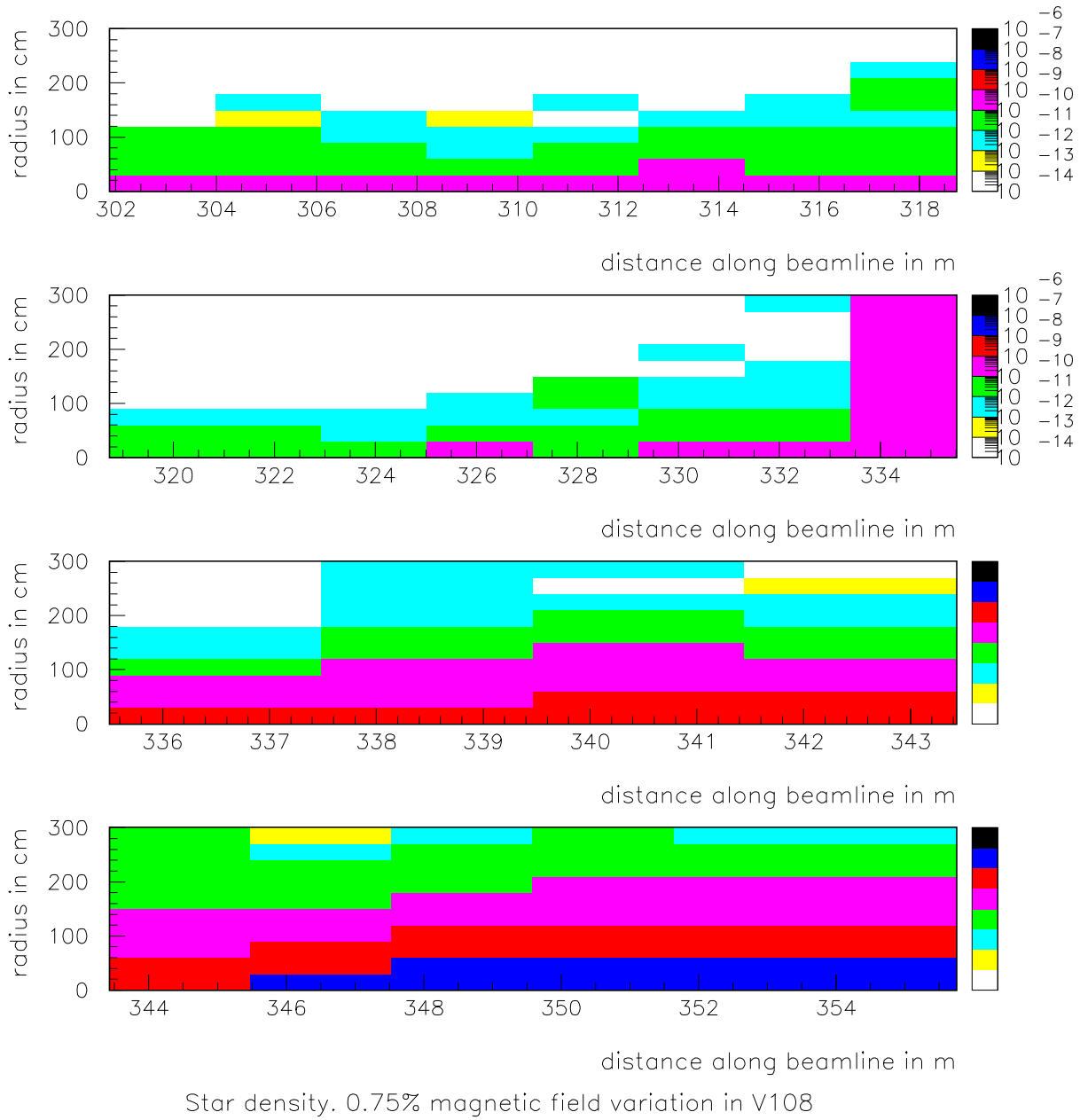

Figure B.16: Star density distribution for last four regions.

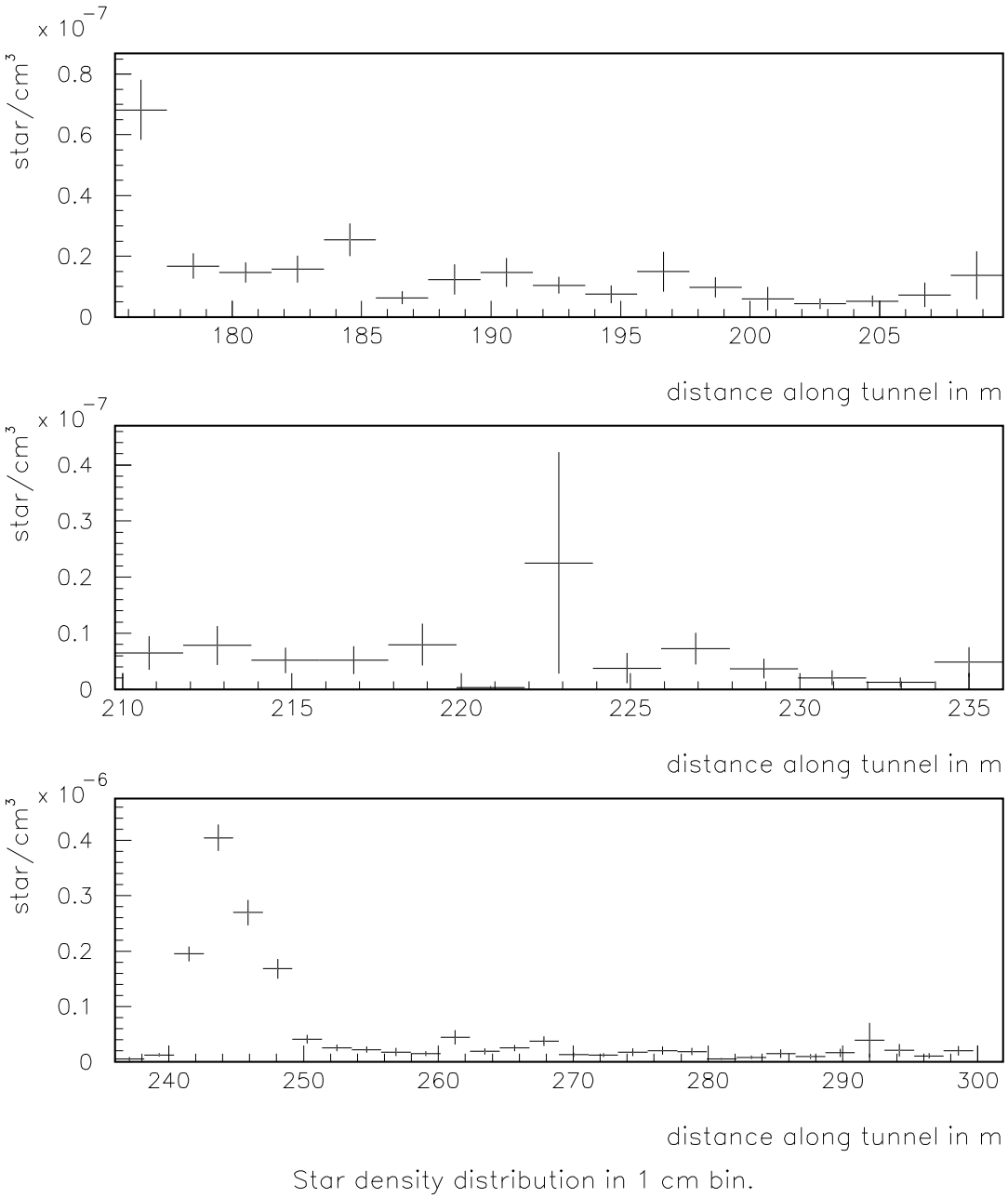

Figure B.17: Star density distribution for first three regions. Magnet current variation on 0.78% in V108.

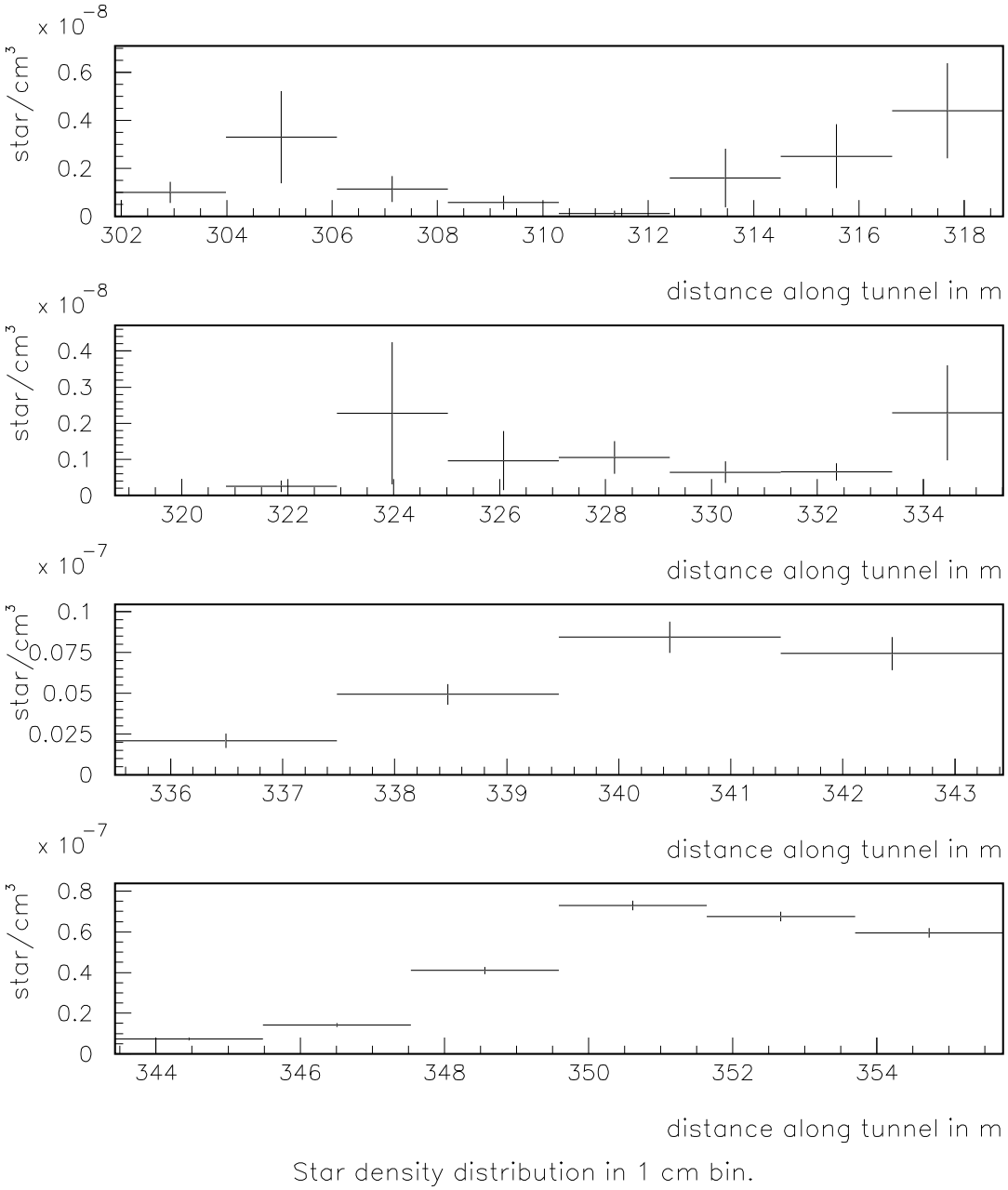

Figure B.18: Star density distribution for last four regions. Magnet current variation on 0.78% in V108.

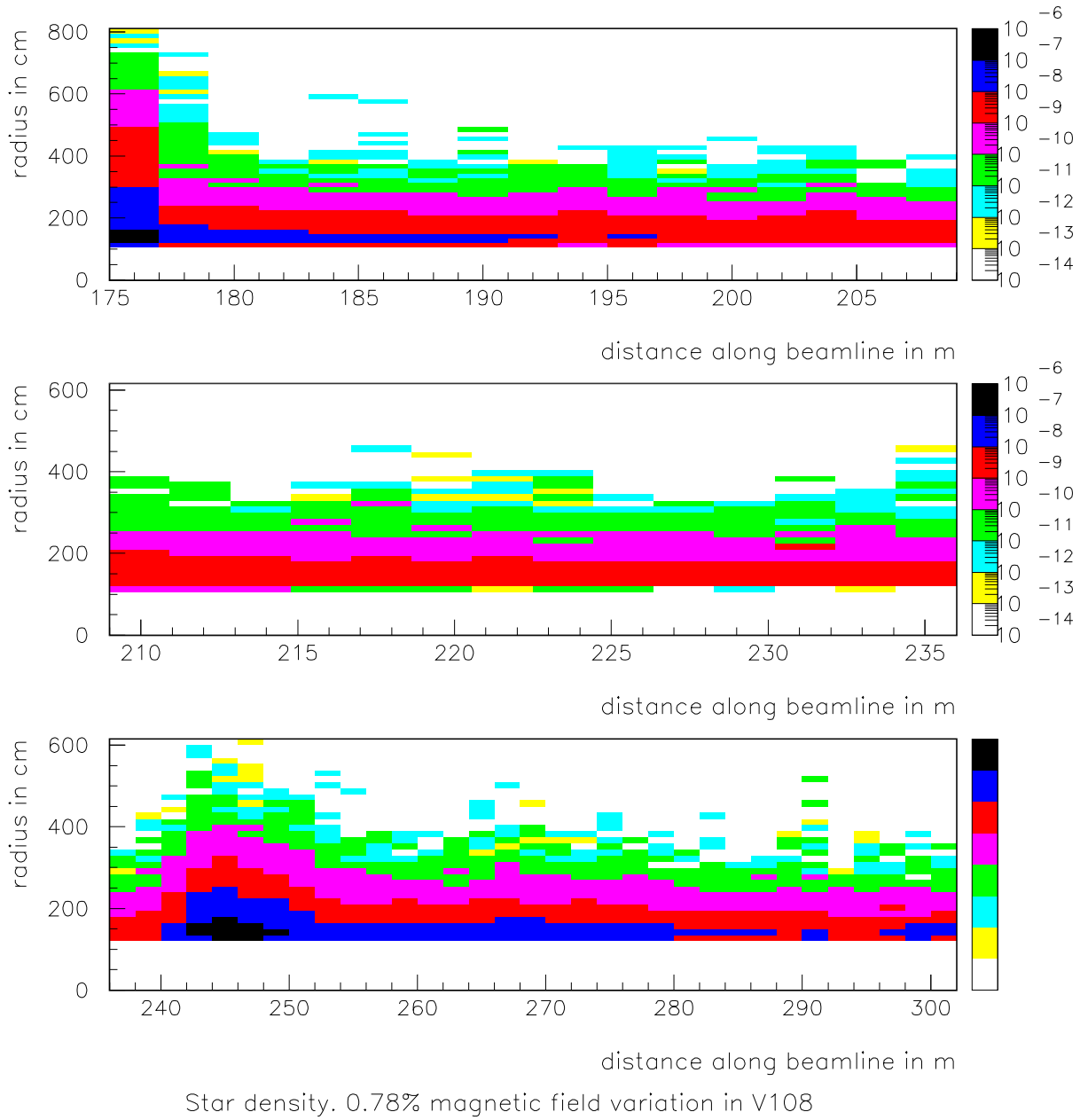

Figure B.19: Star density distribution for first three regions.

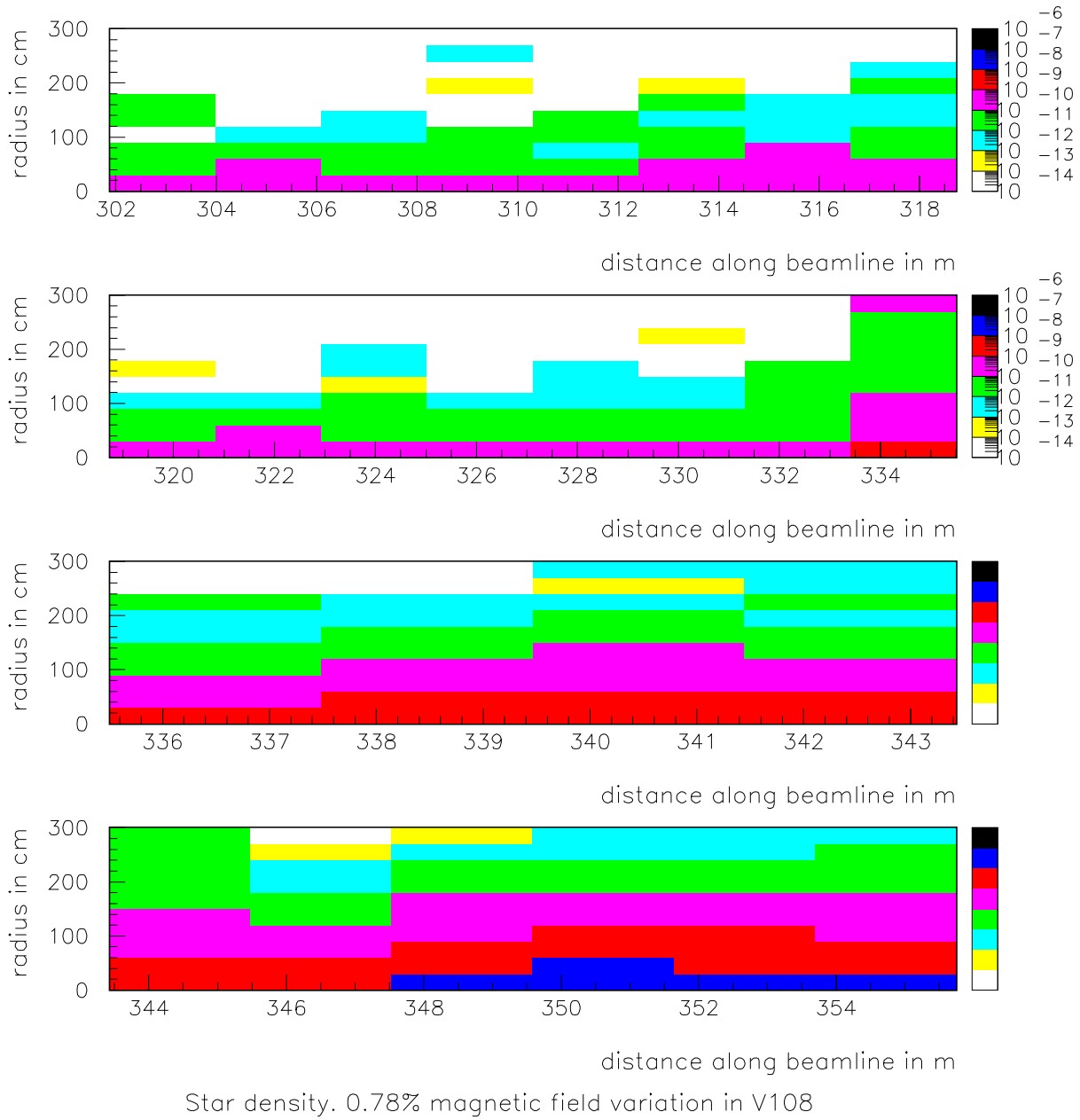

Figure B.20: Star density distribution for last four regions.

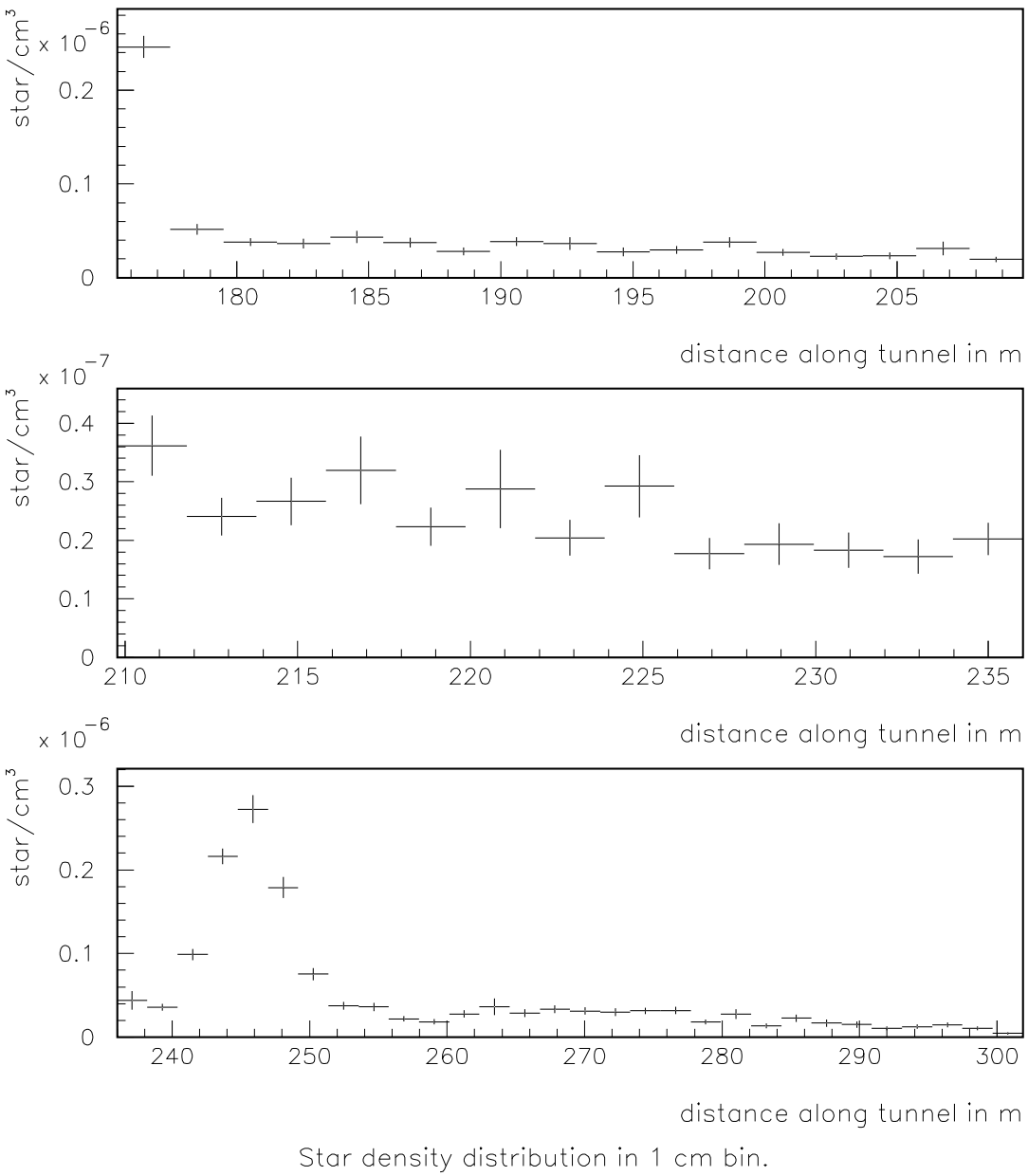

Figure B.21: Star density distribution for first three regions. Magnet current variation on 0.85% in V108.

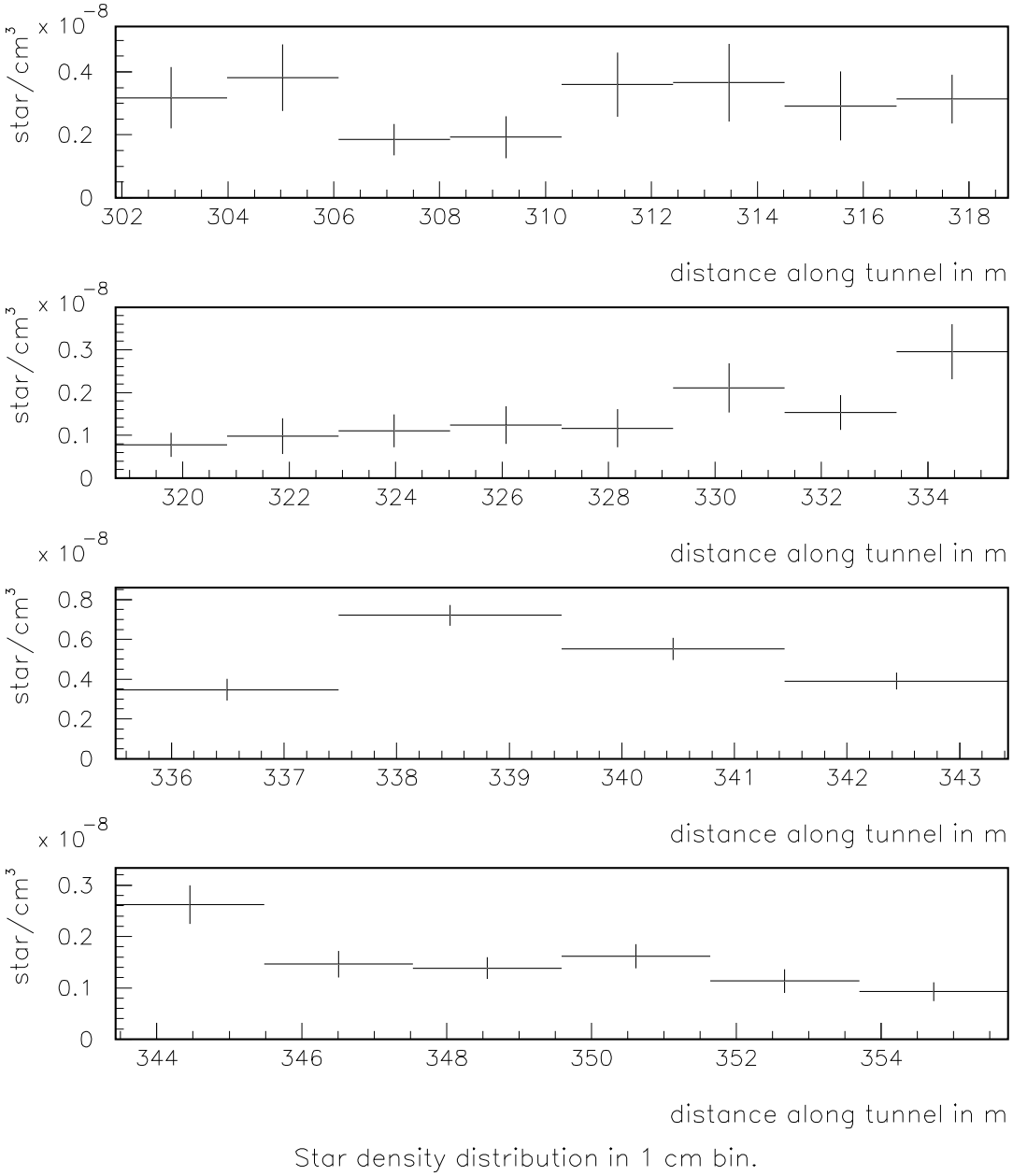

Figure B.22: Star density distribution for last four regions. Magnet current variation on 0.85% in V108.

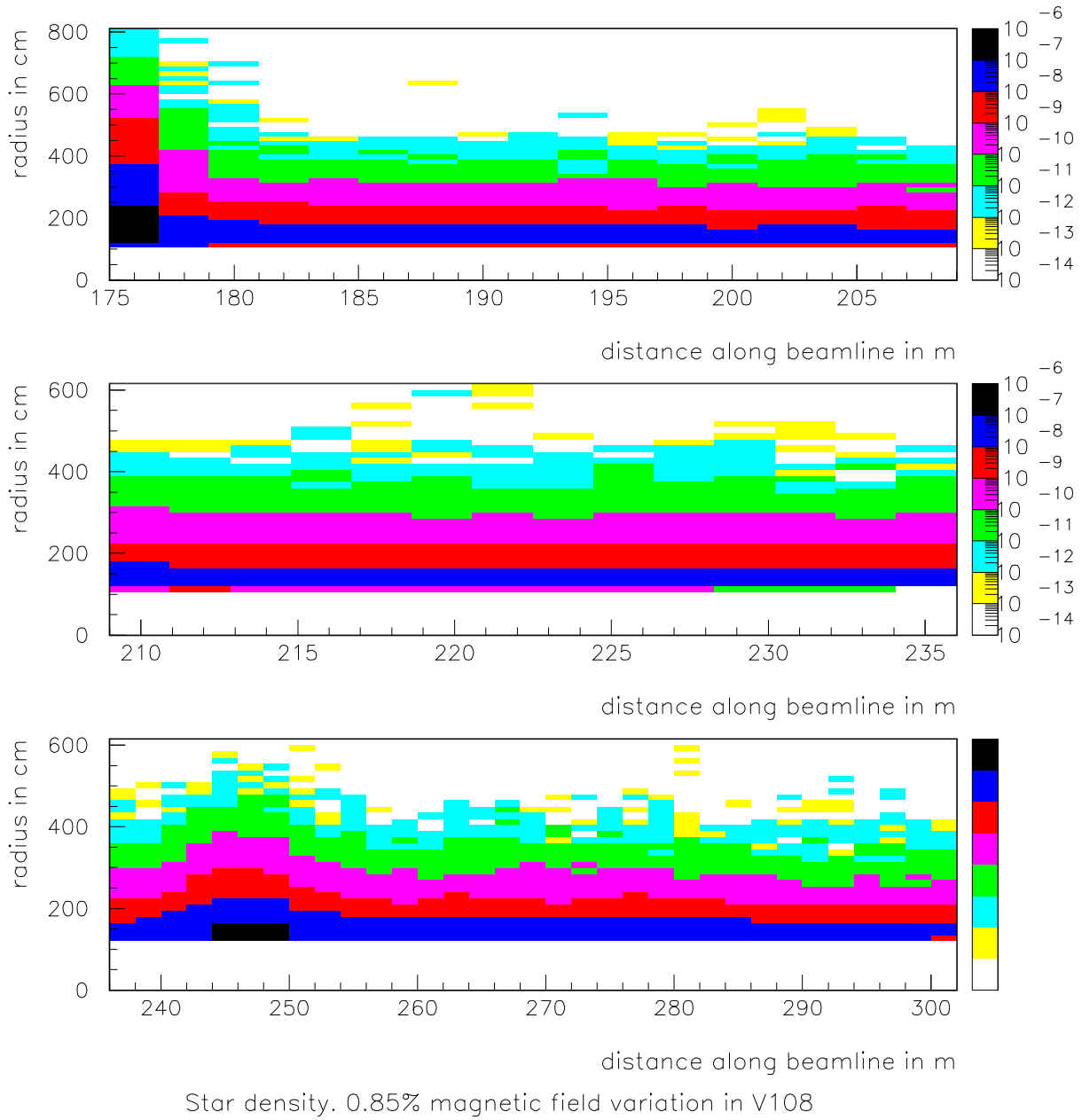

Figure B.23: Star density distribution for first three regions.

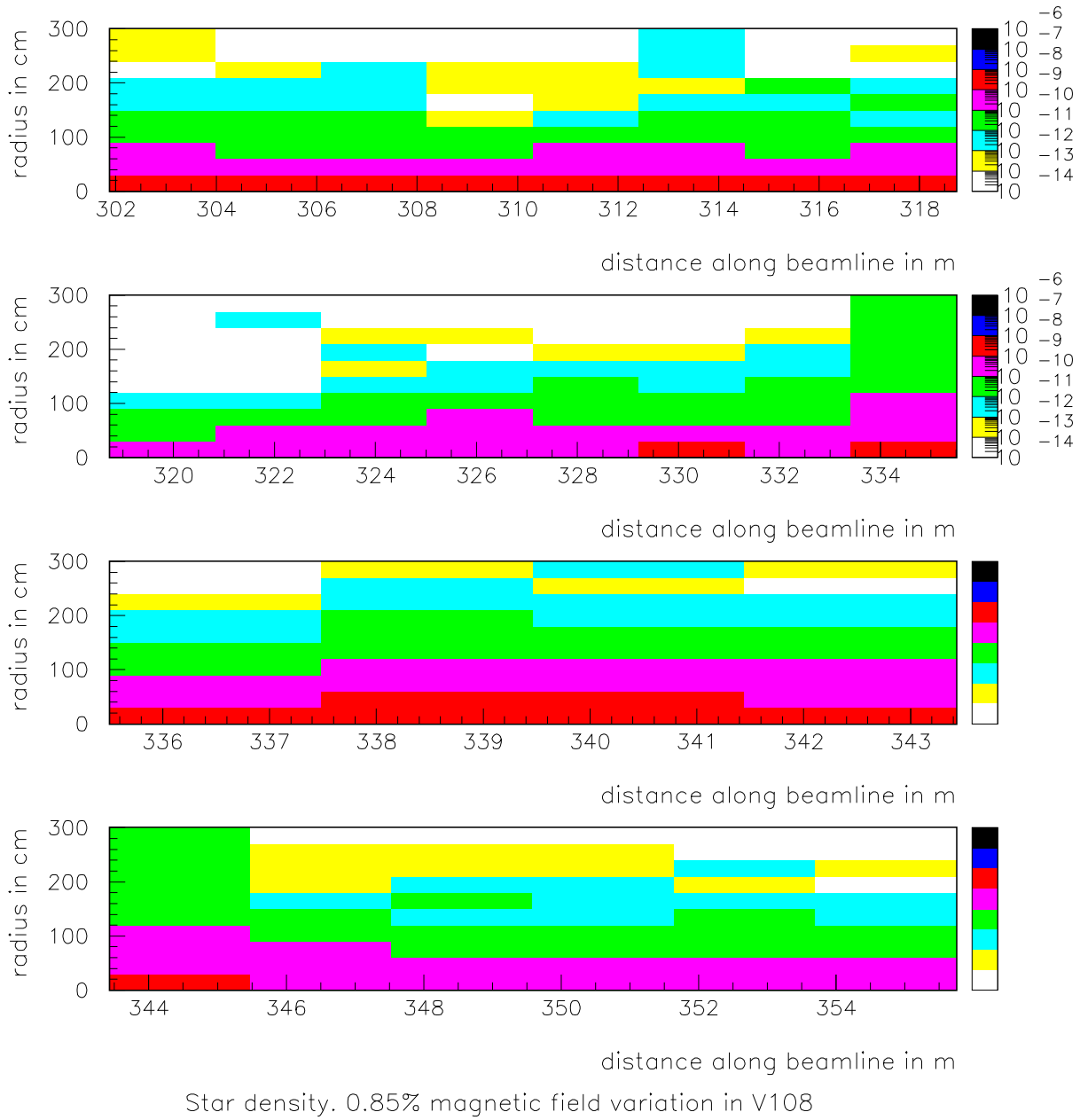

Figure B.24: Star density distribution for last four regions.

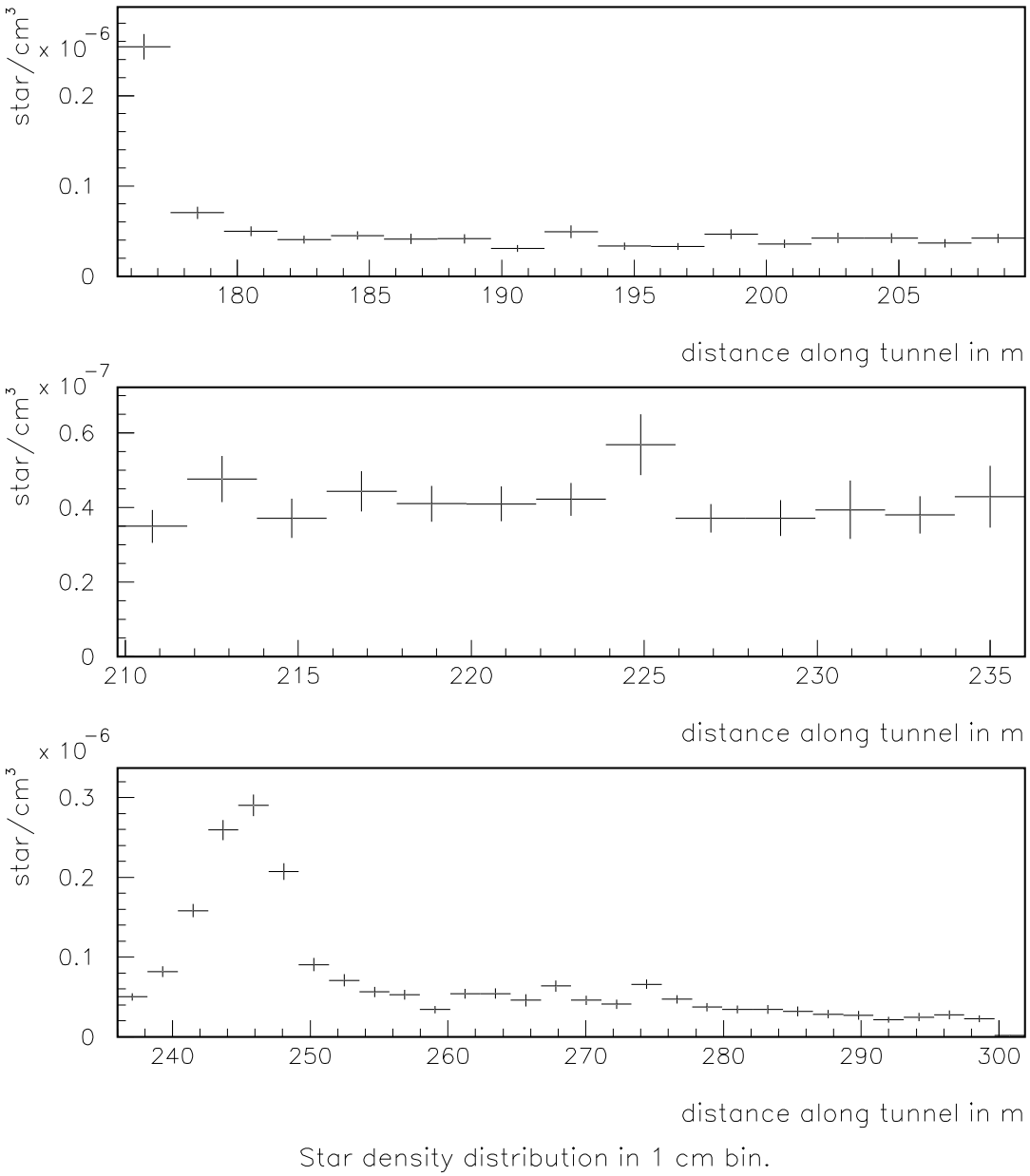

Figure B.25: Star density distribution for first three regions. Magnet current variation on 0.9% in V108.

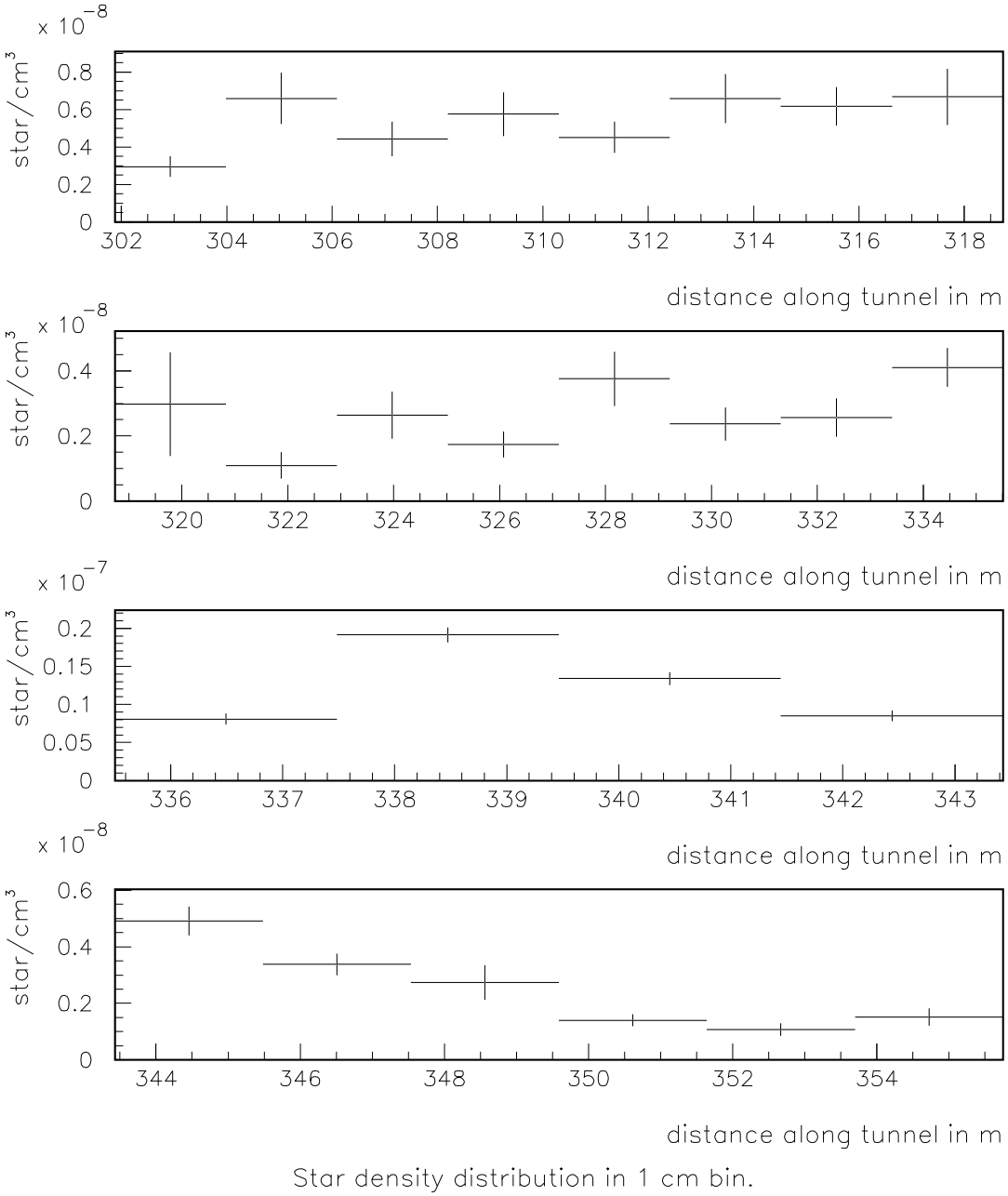

Figure B.26: Star density distribution for last four regions. Magnet current variation on 0.9% in V108.

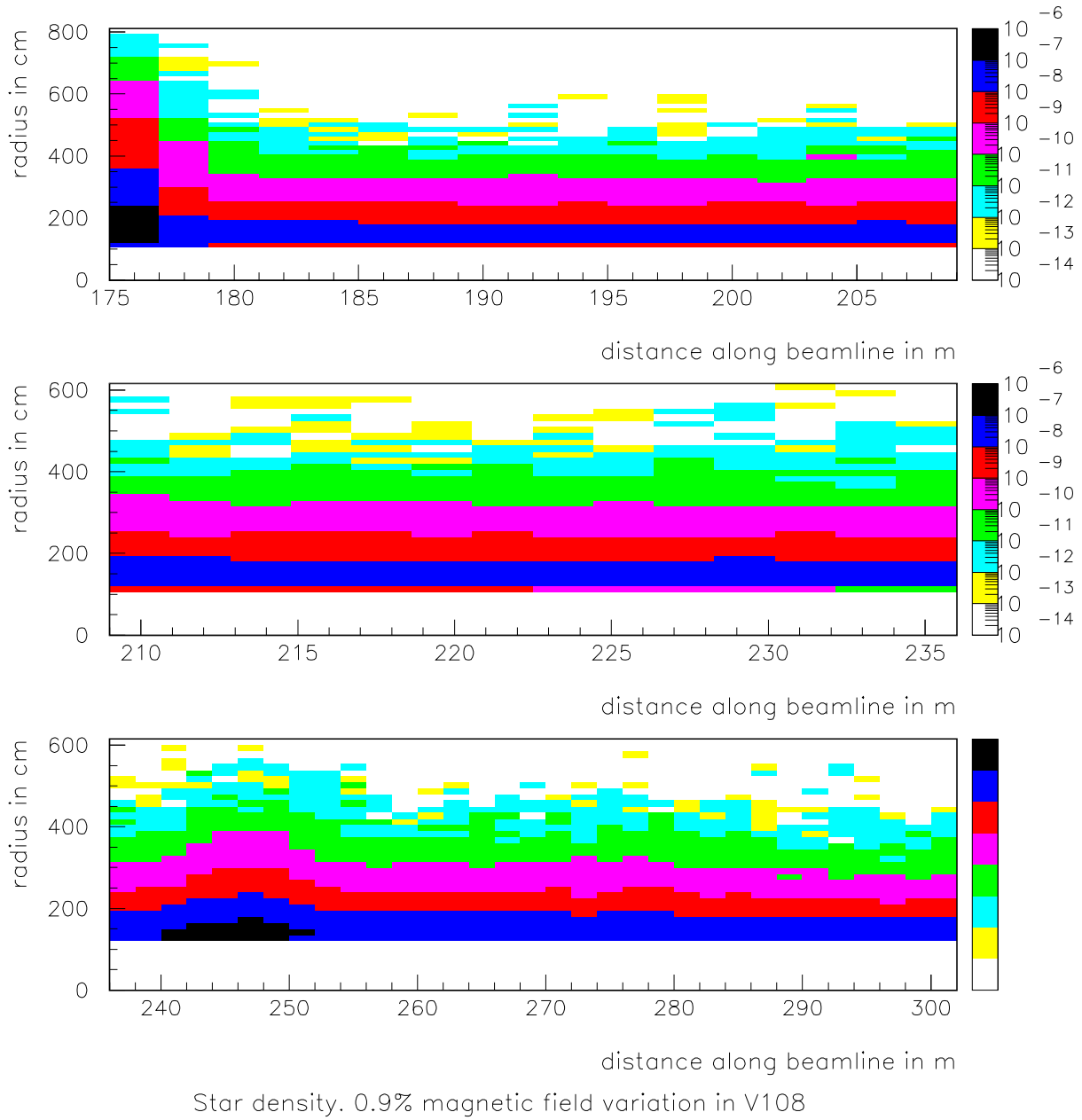

Figure B.27: Star density distribution for first three regions.

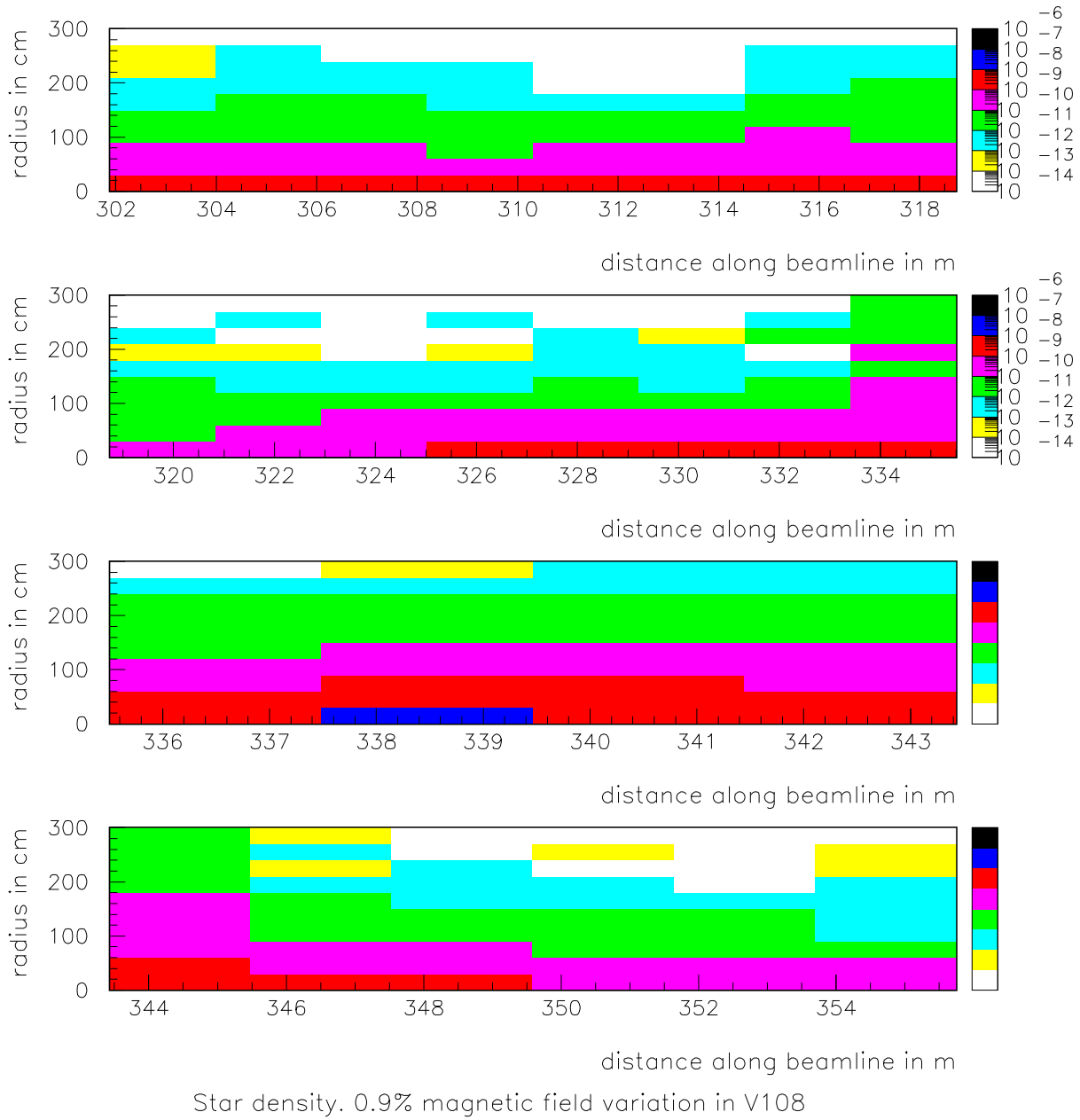

Figure B.28: Star density distribution for last four regions.

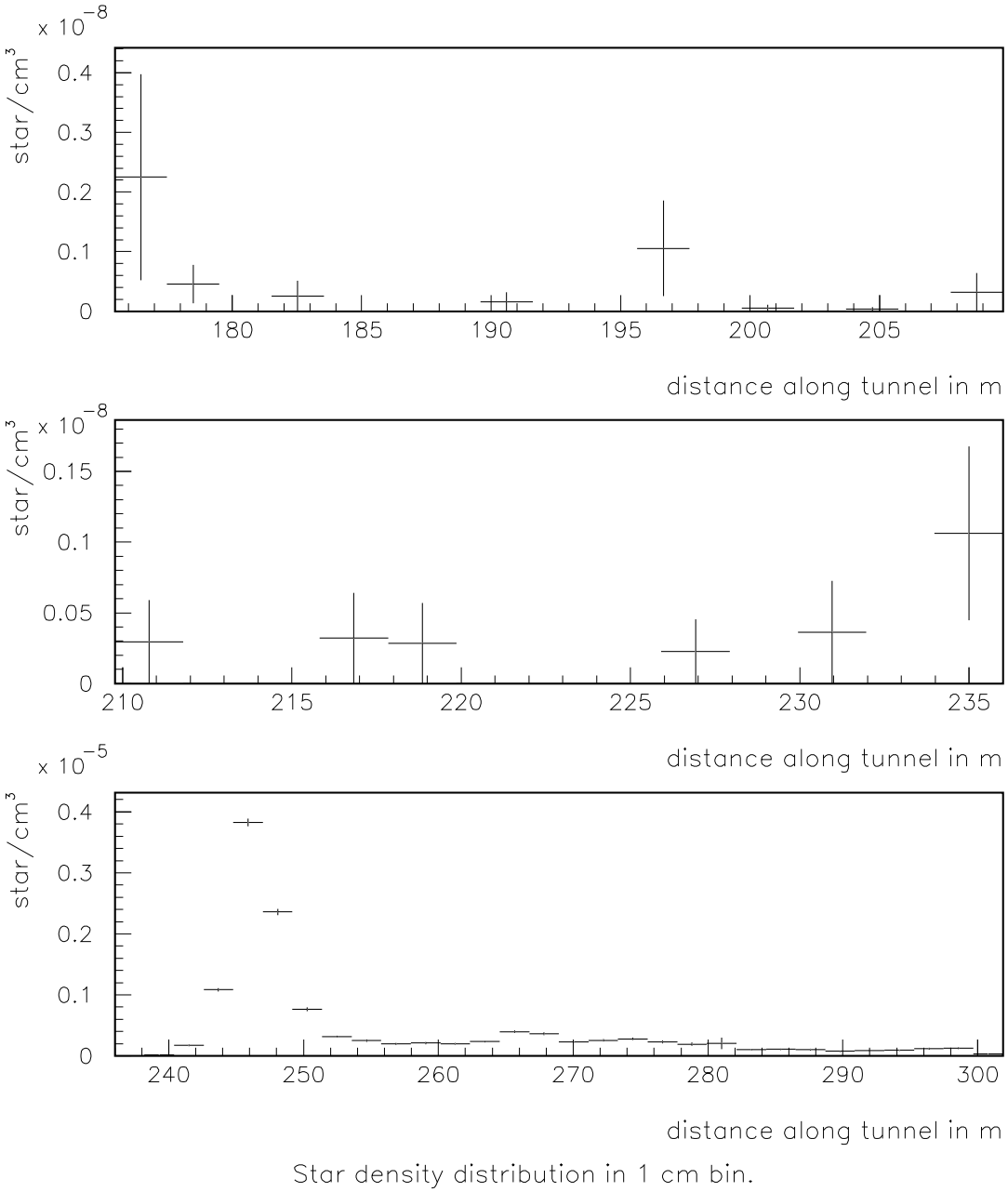

Figure B.29: Star density distribution for first three regions. Magnet current variation on 1.4% HV101 and 0.1% in V108.

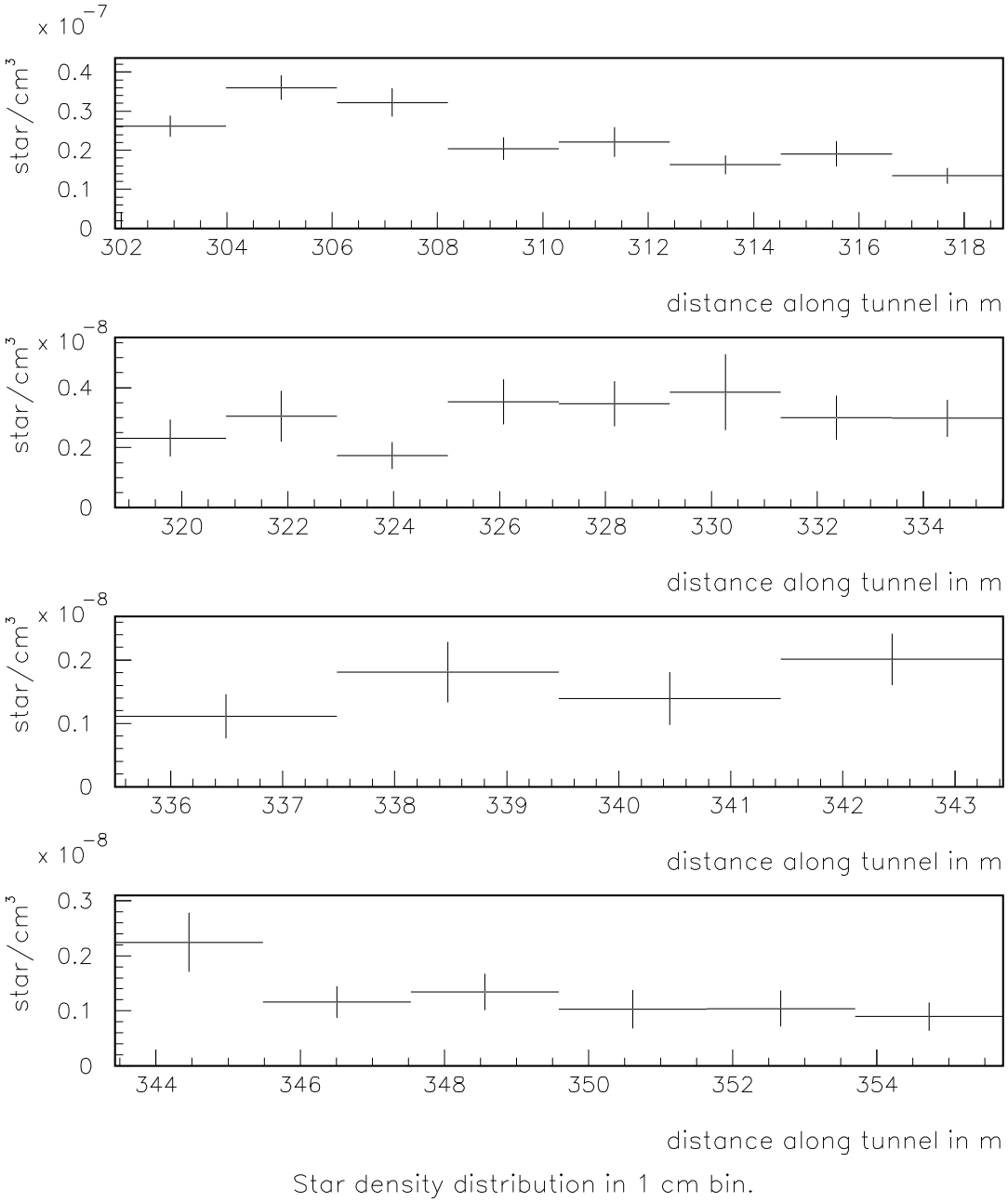

Figure B.30: Star density distribution for last four regions. Magnet current variation on 1.4% HV101 and 0.1% in V108.

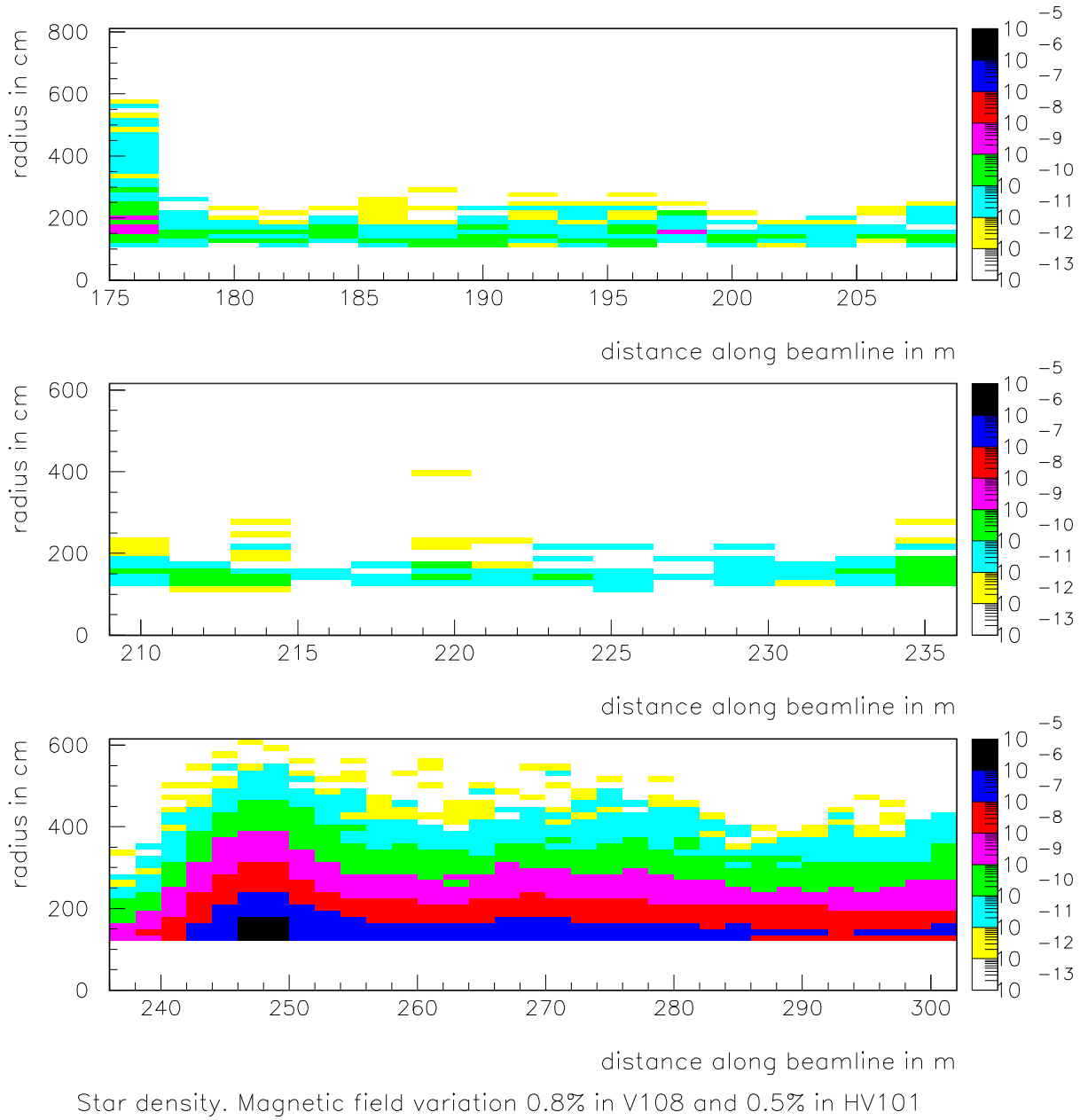

Figure B.31: Star density distribution for first three regions.

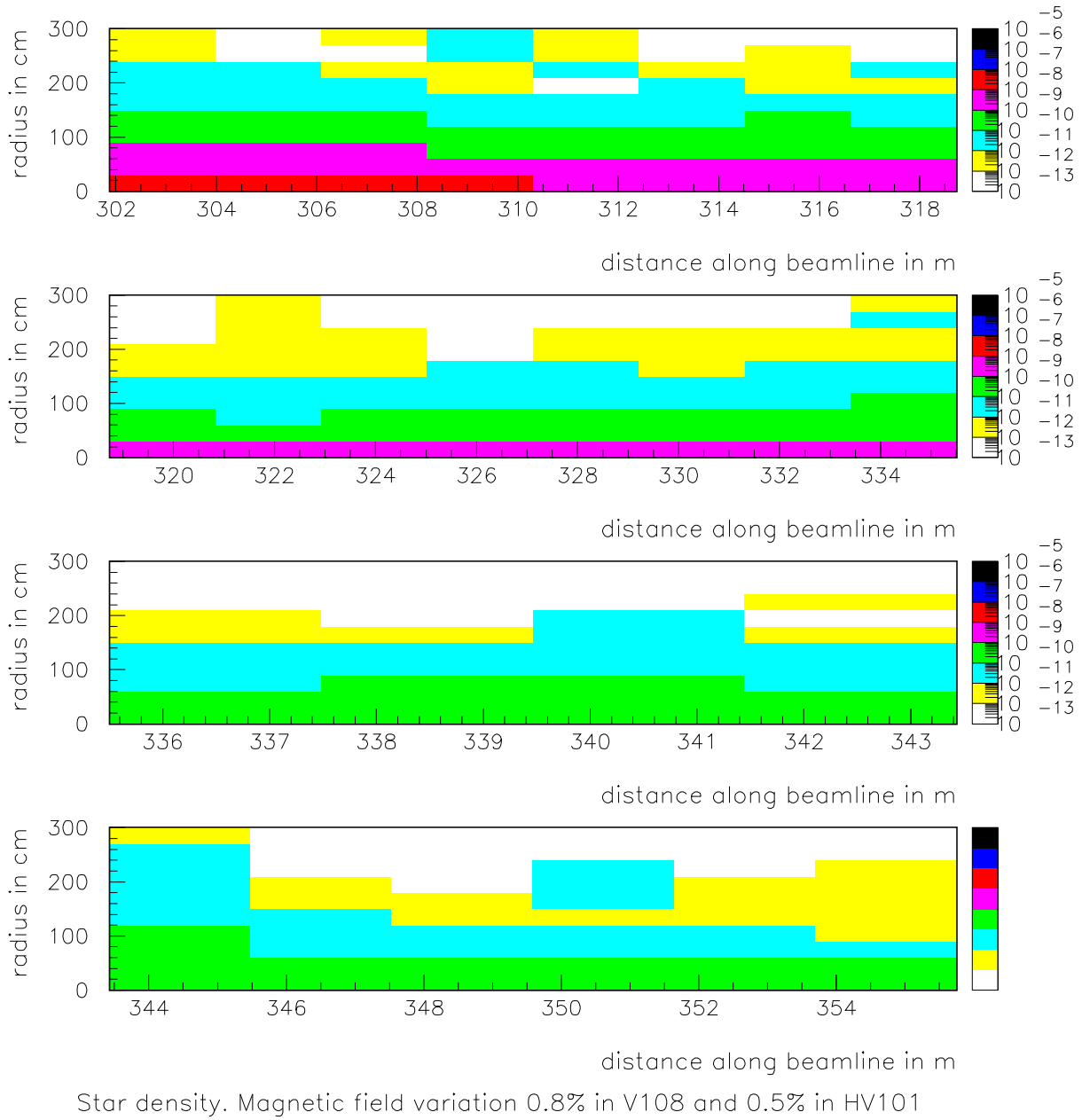

Figure B.32: Star density distribution for last four regions.

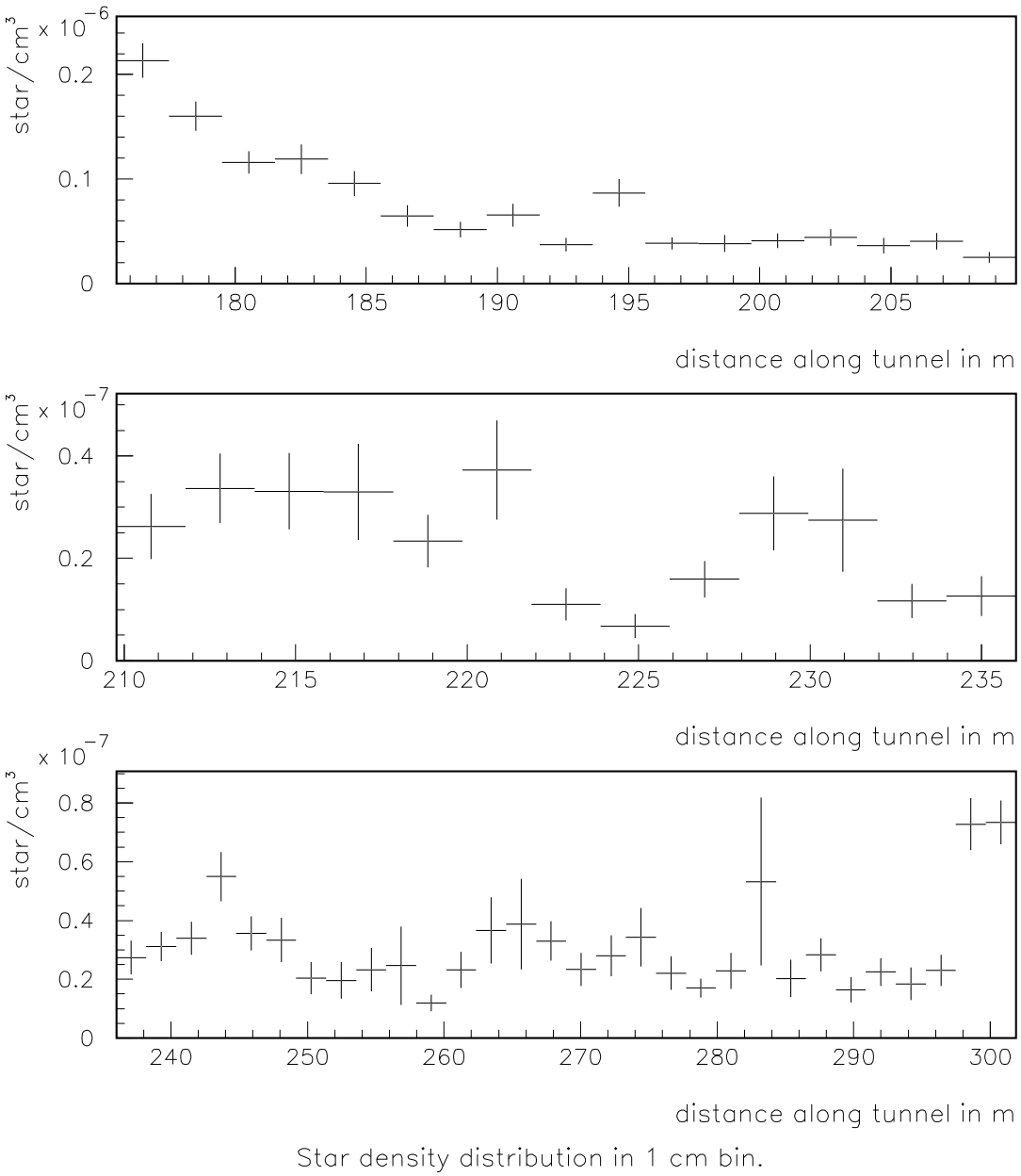

Figure B.33: Star density distribution for first three regions. Magnet current variation on 0.5% HV101 and 0.8% in V108.

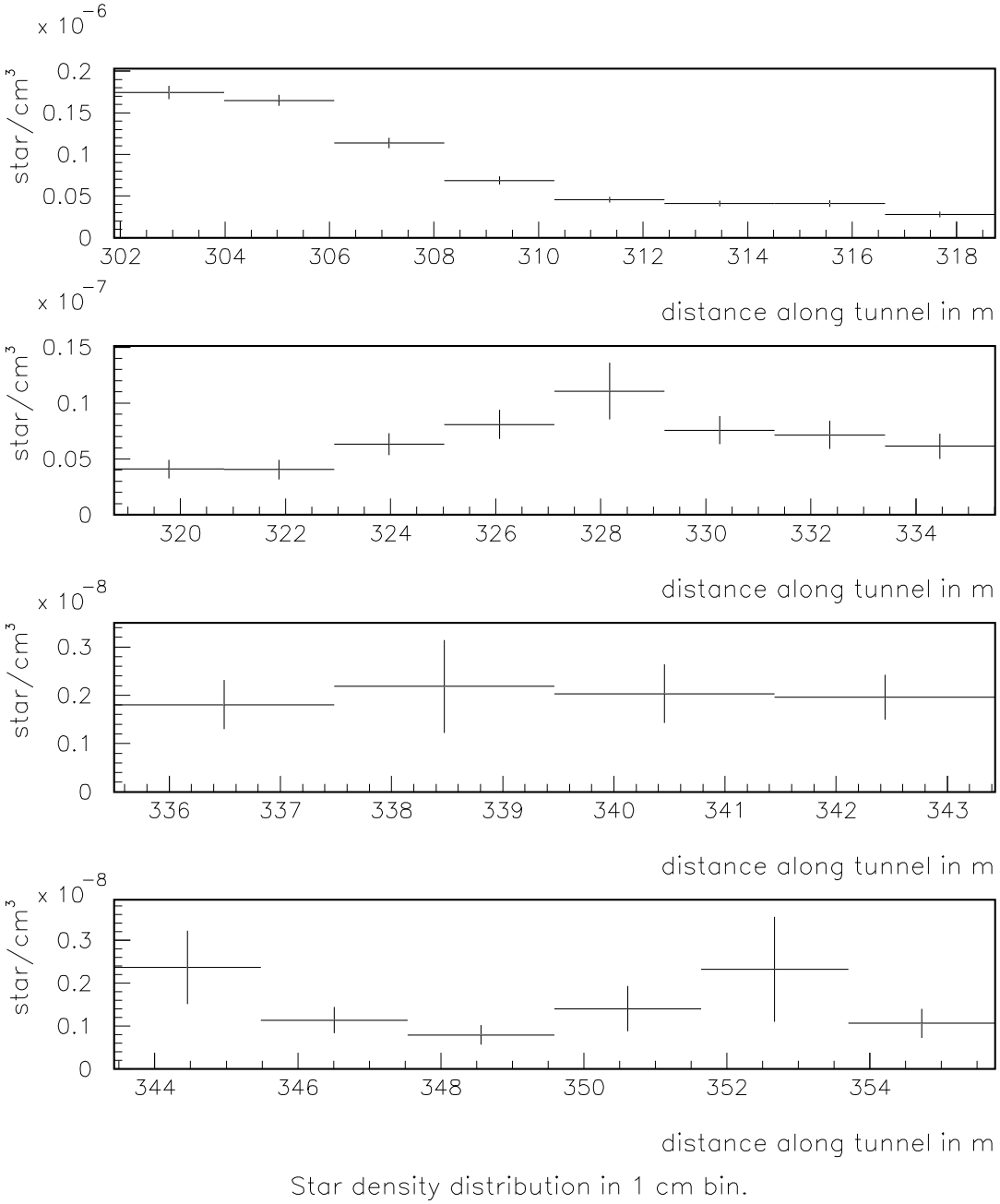

Figure B.34: Star density distribution for last four regions. Magnet current variation on 0.5% HV101 and 0.8% in V108.

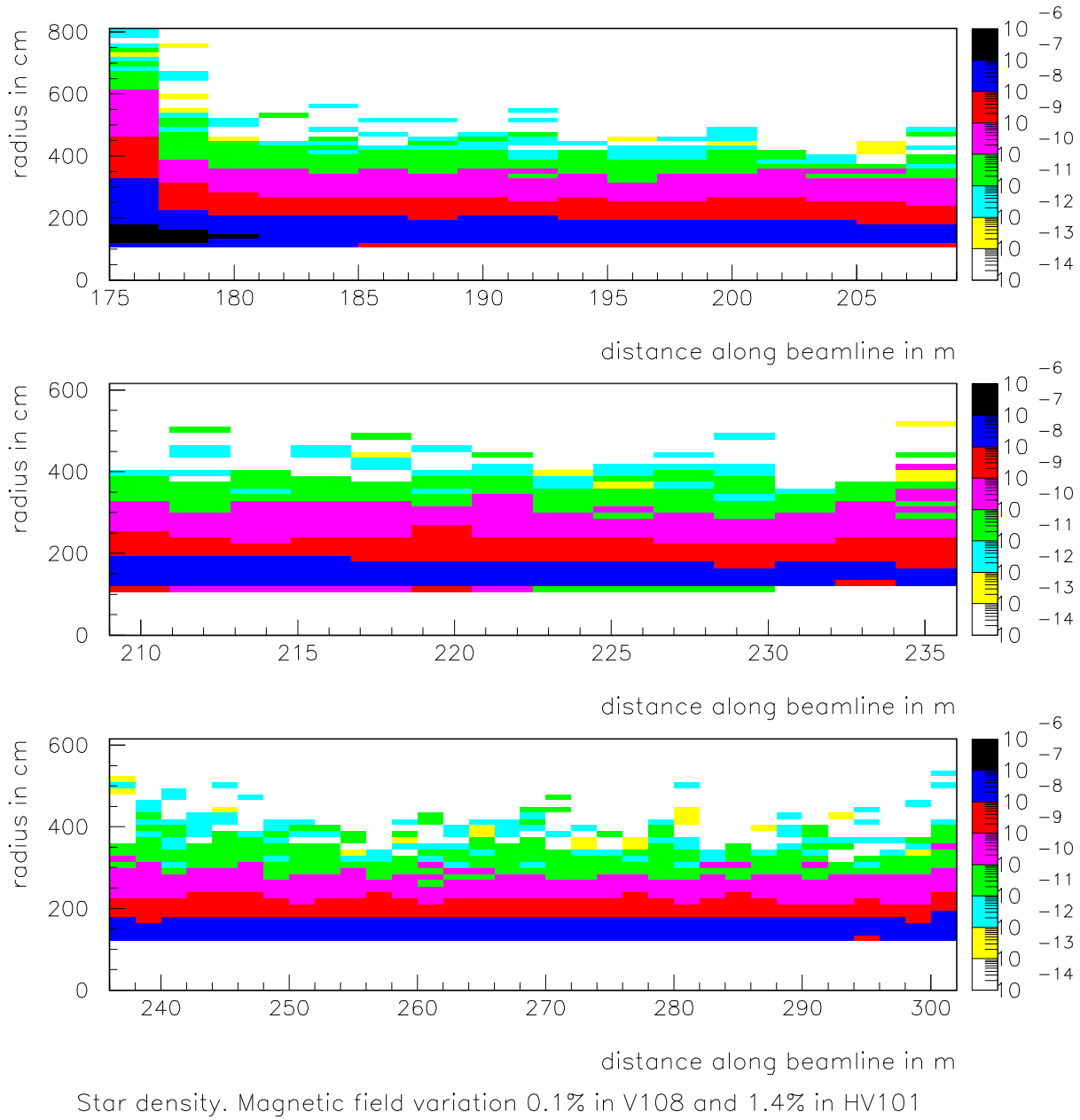

Figure B.35: Star density distribution for first three regions.

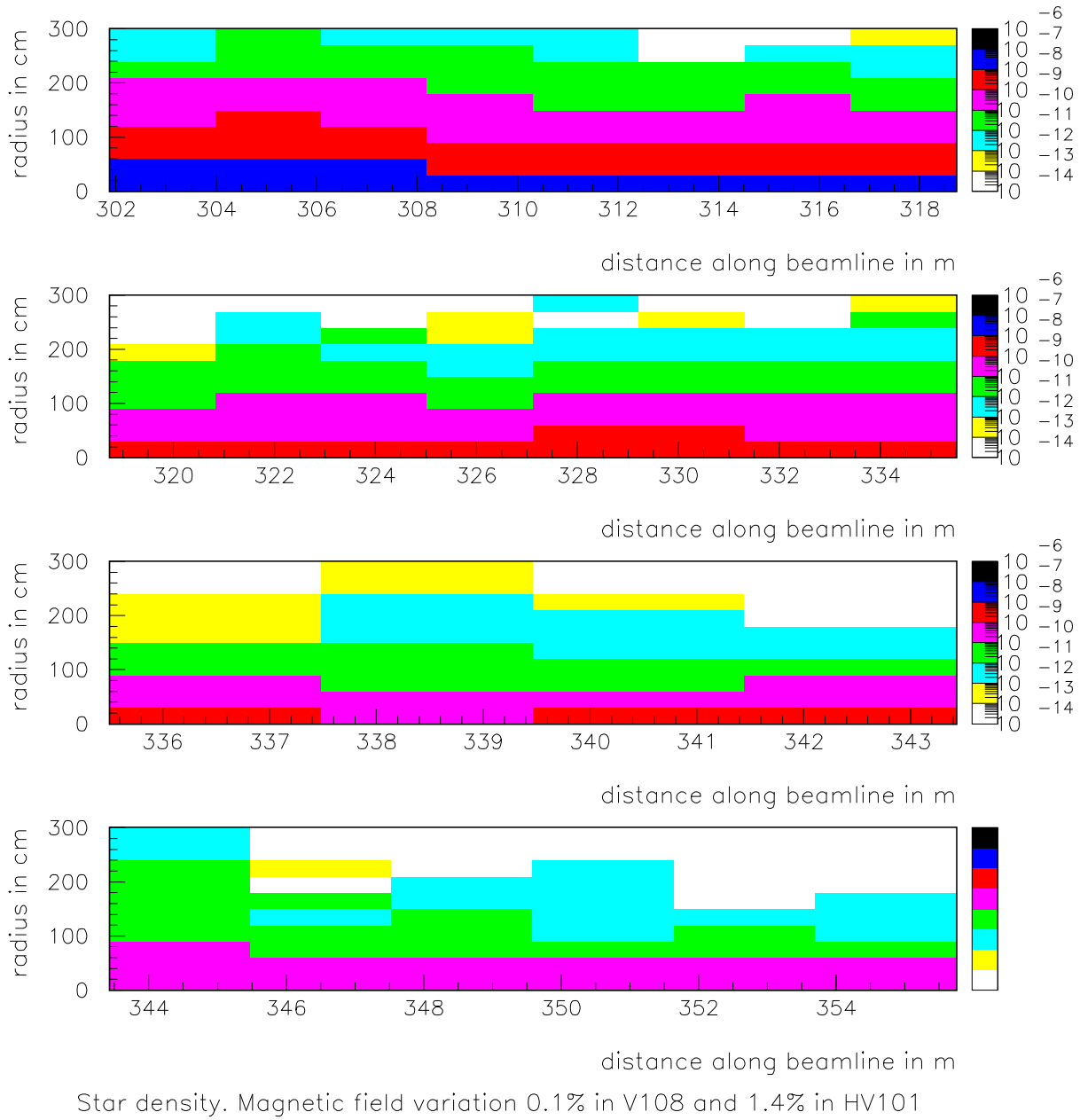

Figure B.36: Star density distribution for last four regions.

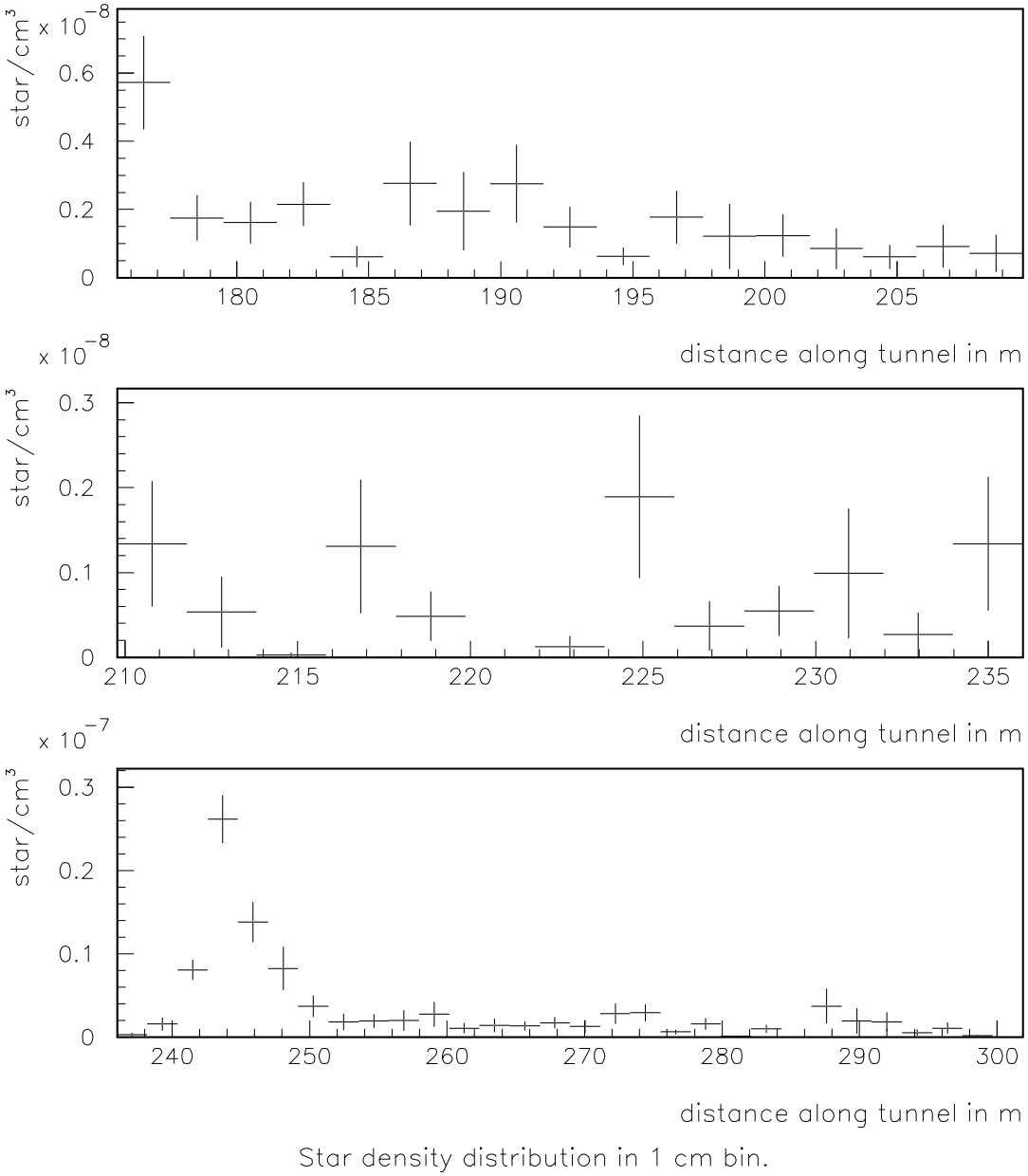

Figure B.37: Star density distribution for first three regions. Magnet current variation on 1% V118 and 0.7% in V108.

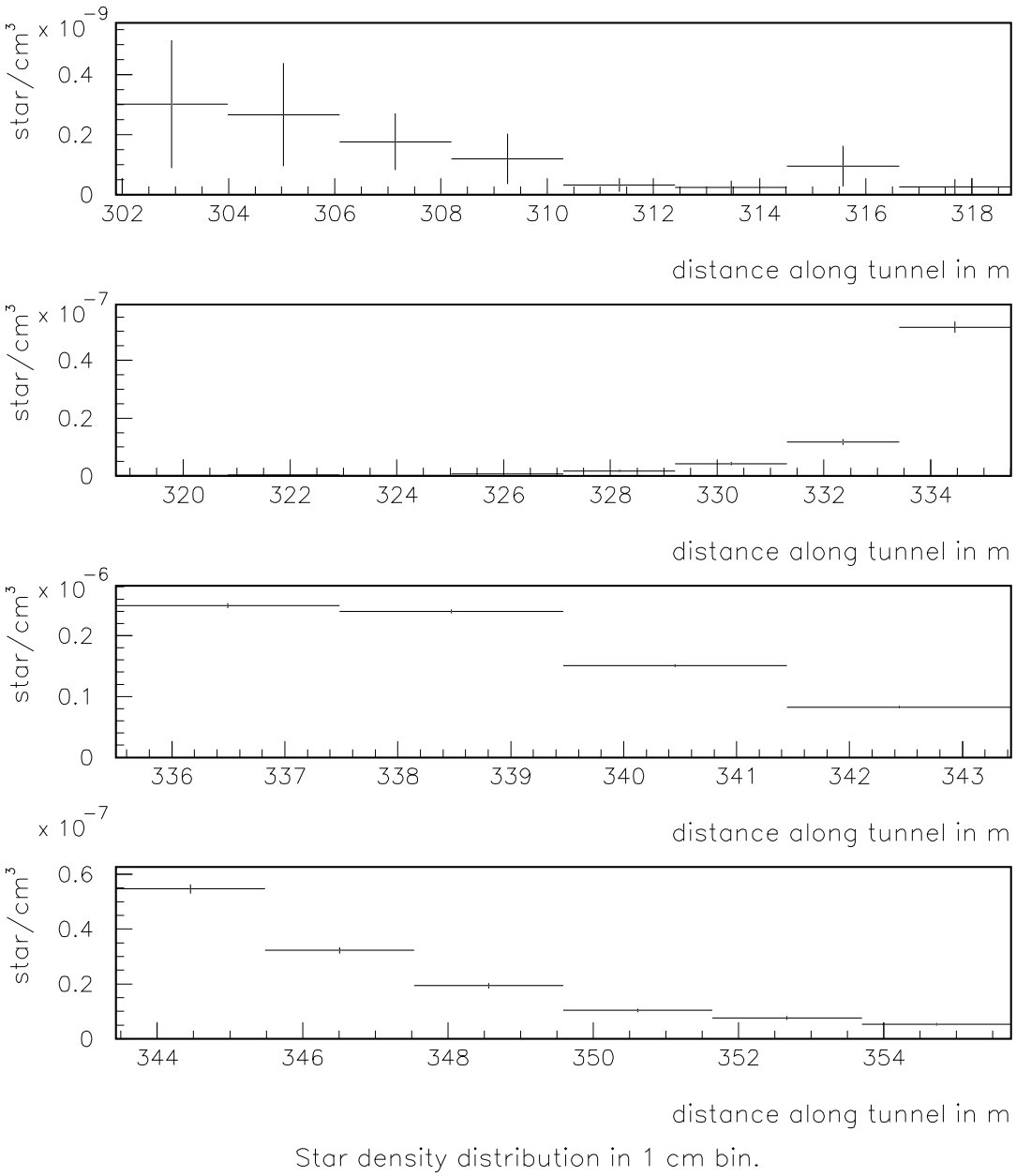

Figure B.38: Star density distribution for last four regions. Magnet current variation on 1% V118 and 0.7% in V108.

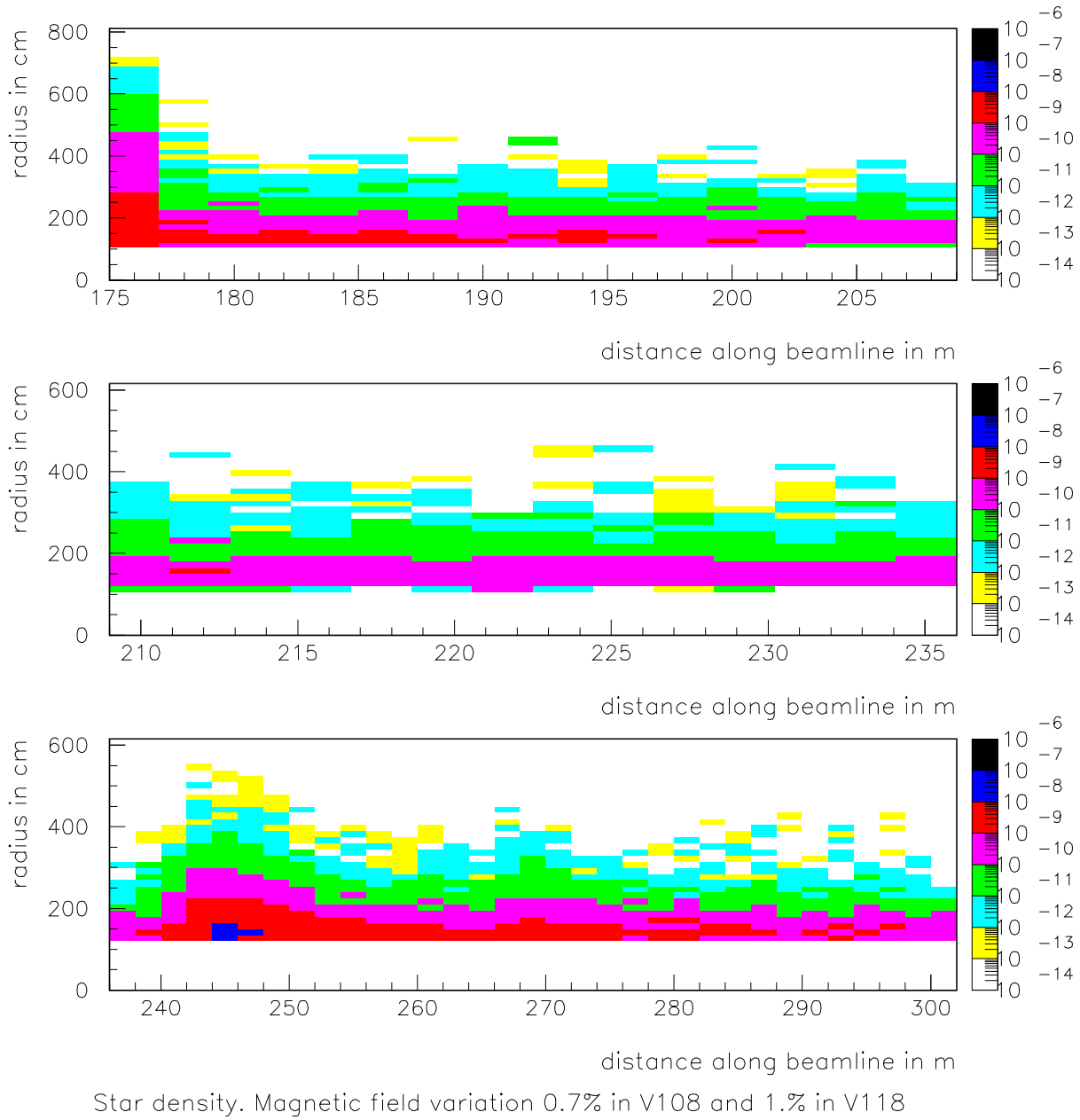

Figure B.39: Star density distribution for first three regions.

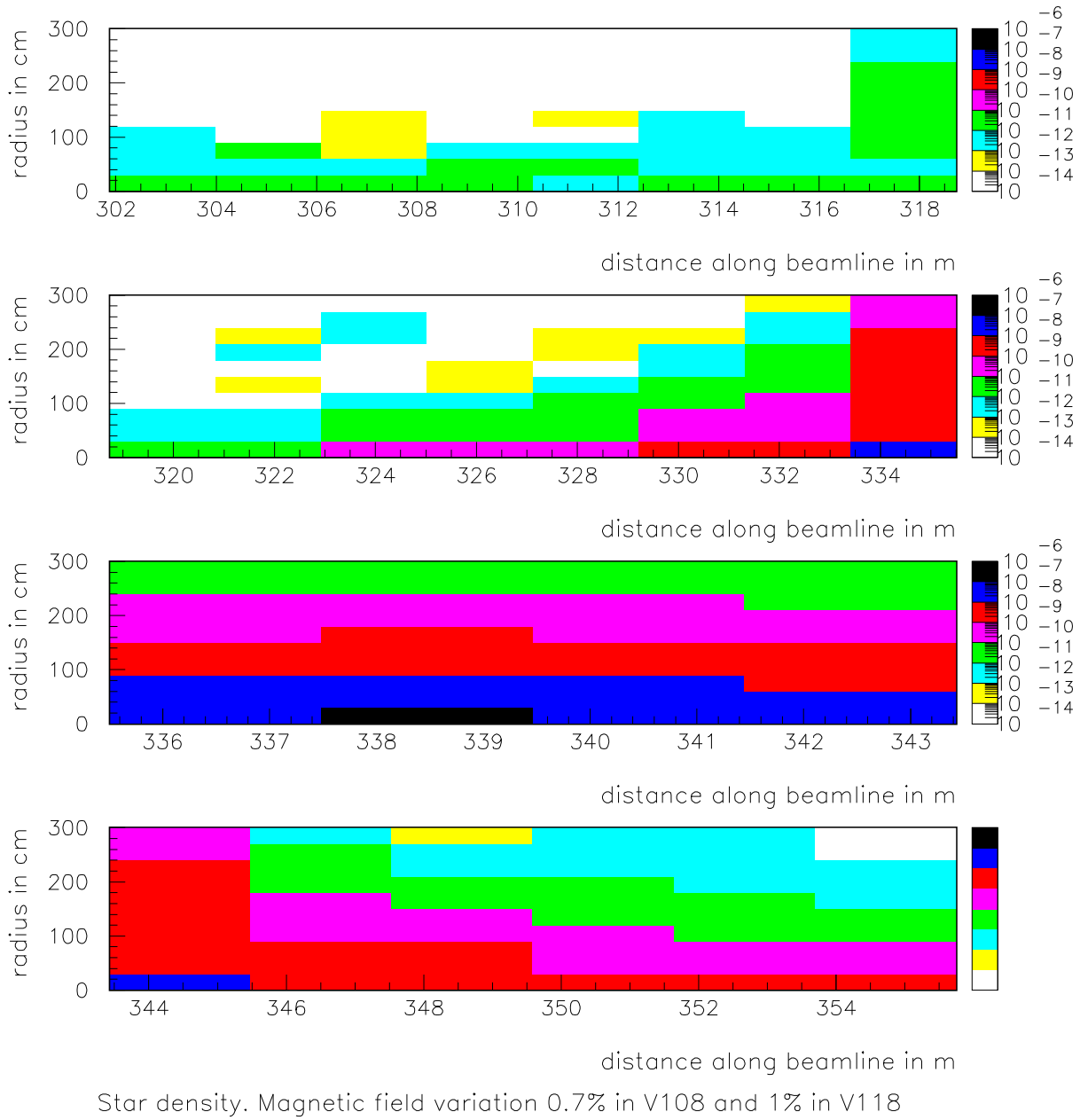

Figure B.40: Star density distribution for last four regions.

Appendix C

Star Density and Beam Loss Monitors

This appendix documents the studies of beam loss (studied in Chapter 4) to determine the simulated response in beam loss monitors at the position of each magnet. For most of the scenarios considered in Section 4.4, the energy deposition in beam loss monitors is calculated. Typical distributions of detector signals along the beam line are shown in Figure C.1. The energy deposition in the monitors and star density distribution are clearly correlated.

Monitor activation in first two regions is due to beam interactions with the HT107 corrector. In figure C.2 the dependence of average star density on the signal in beam loss monitor placed on HT107 is shown. The correlation can be described by a simple linear dependence.

In region 4 the most significant beam losses occur on the V110-1, Q108 and HT108 magnets. In figure C.3a the average star density vs. sum of signal from detectors placed on these magnets is shown. The V110-1 and Q108 magnets are much larger than the HT108 corrector (see Appendix A). Detectors set at different distances from beam pipe have different sensitivity. If the difference in sensitivity is taken into account, a linear correlation between star density and signal in detectors can be achieved (see figure C.3b)

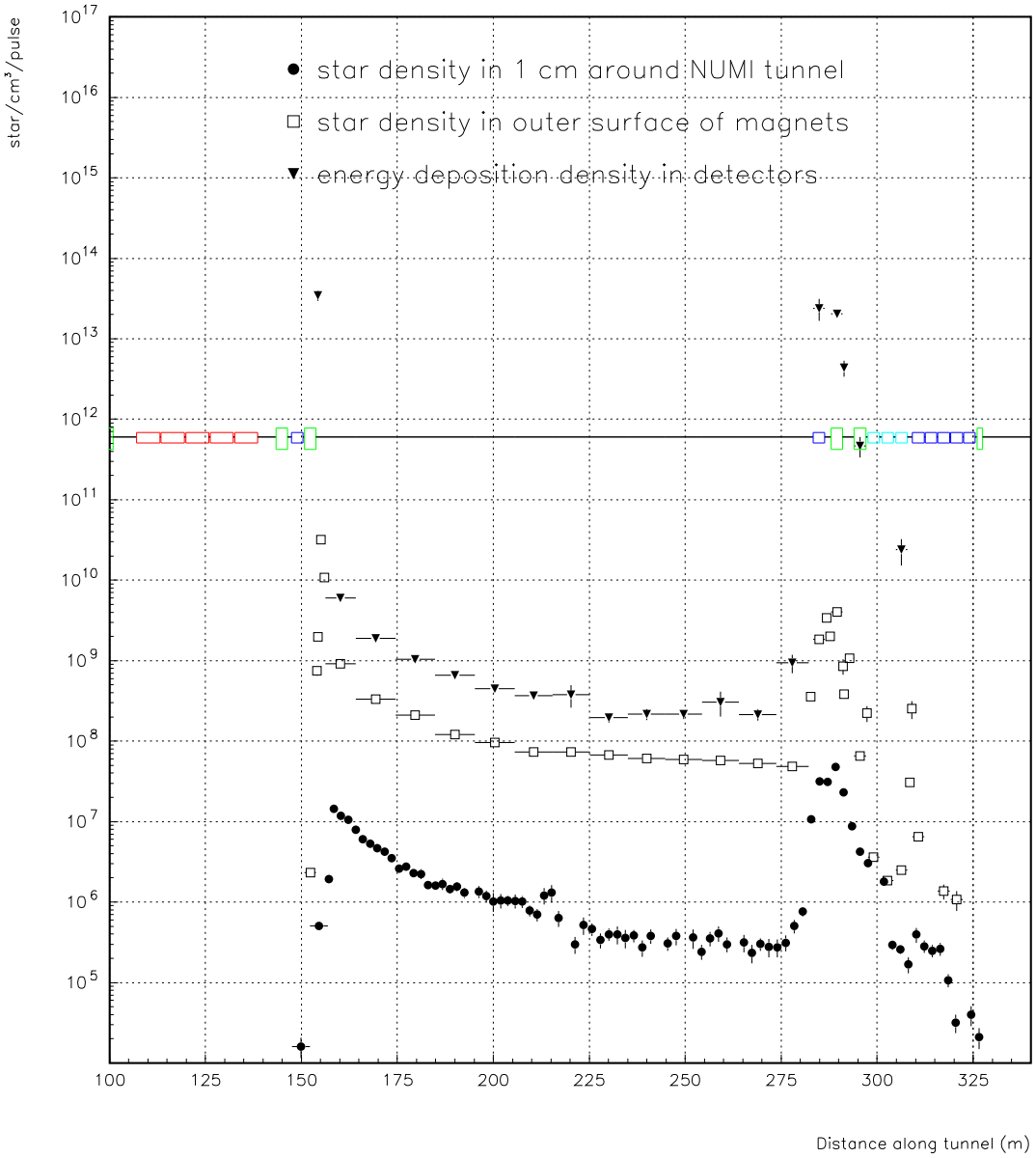

Figure C.1: Star density distribution and energy deposition in beam loss monitors. Magnet current variation set to 0.4% in V105.

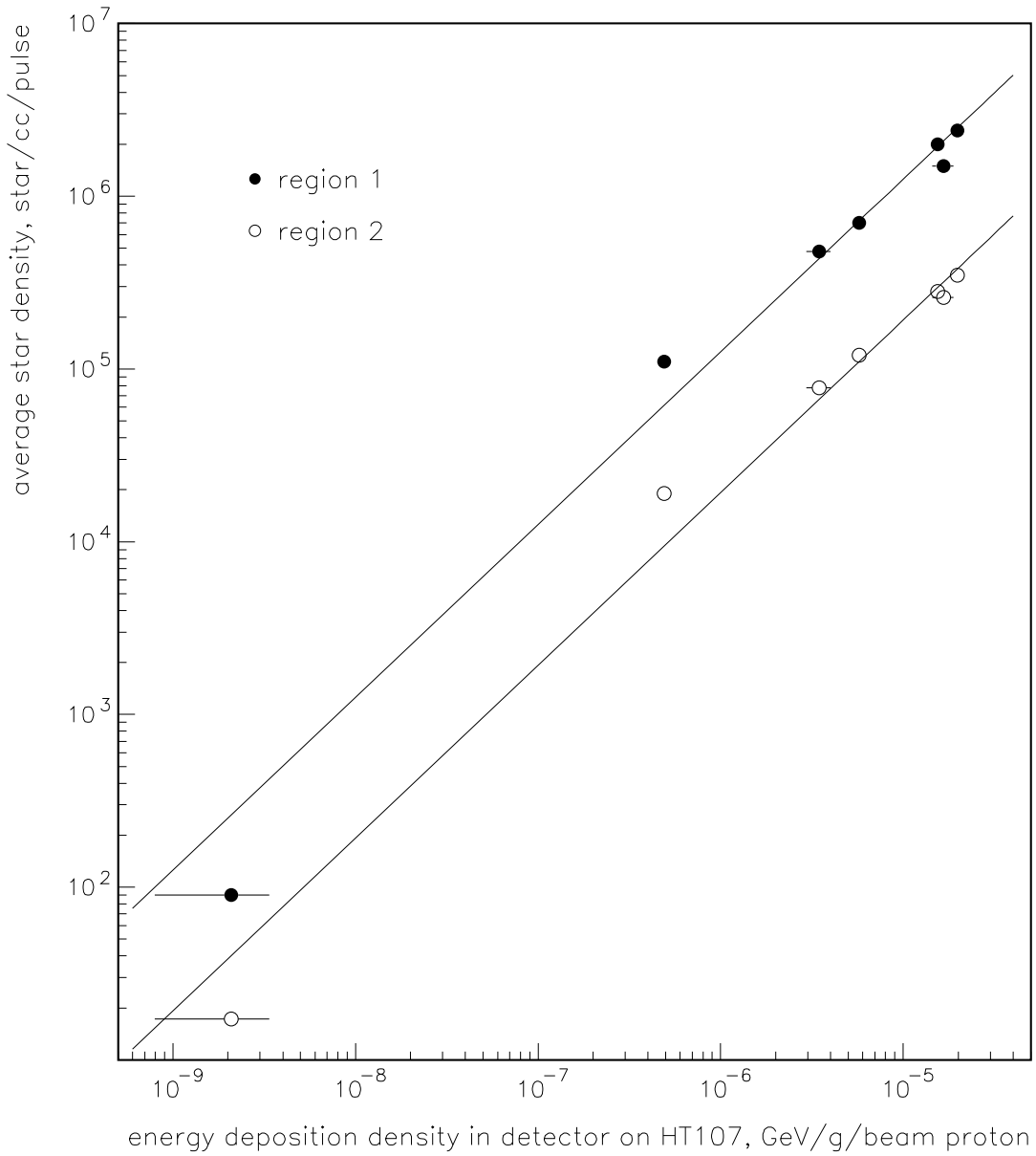

Figure C.2: Correlation between star density in regions 1,2 and energy deposition in beam loss monitor.

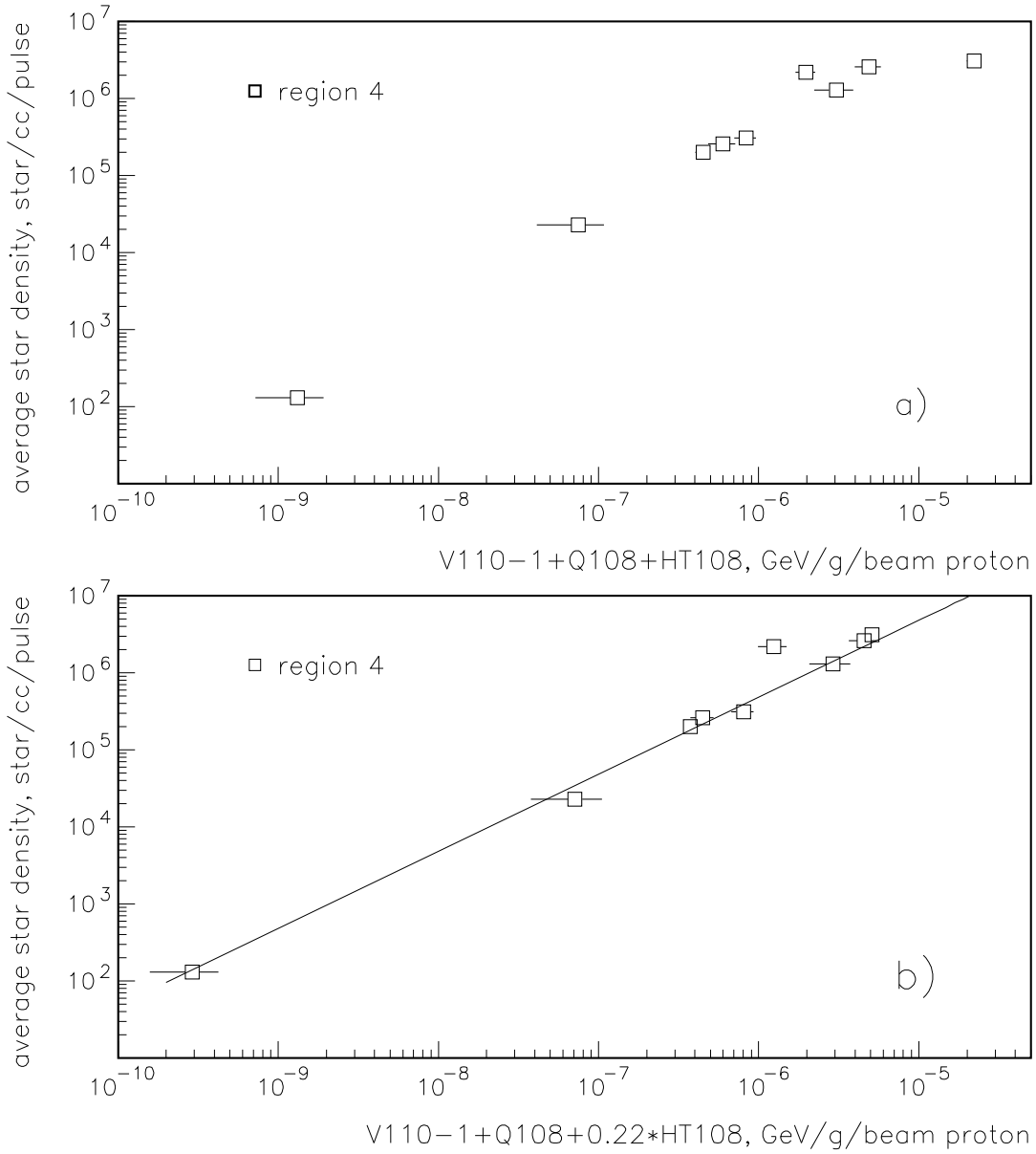

Figure C.3: Correlation between star density in region 4 and energy deposition in beam loss monitors.